UNIVERSITÀ DEGLI STUDI DI TRIESTE

UNIVERSITÀ DEGLI STUDI DI TRIESTE

XXXVI CICLO DEL DOTTORATO DI RICERCA IN

NANOTECNOLOGIE

Borsa MUR/Ateneo cofinanziata dal Dipartimento di Fisica su fondi CNR-IOM

MORPHOLOGICAL AND MECHANICAL PROPERTIES OF CELLS INVESTIGATED BY MULTIMODAL IMAGING AND LOCAL PROBING TECHNIQUES

Settore scientifico-disciplinare: **ING-IND/22**

DOTTORANDA
NICOLETTA BRAIDOTTI

COORDINATORE
PROF. ALBERTO MORGANTE

SUPERVISORE DI TESI
DOTT. DANUT ADRIAN COJOC

CO-SUPERVISORE DI TESI
PROF. ORFEO SBAIZERO

ANNO ACCADEMICO 2022/2023

ACKNOWLEDGEMENTS

I would like to thank for the financial support the *Doctoral School of Nanotechnology* of the *University of Trieste* and the *Istituto Officina dei Materiali - Consiglio Nazionale delle Ricerche (CNR-IOM)* of Trieste.

I thank *Dr. Silvia Gazzin*, *Dr. Sri Yayanti*, *Prof. Claudio Tiribelli*, and the Italian Liver Foundation for the generous animal tissue donation (protocol 1FF80.N.PZB). They allowed me to carry on experiments on primary cardiac fibroblasts conducting research in a very sustainable way and in the full respect of animals. I also thank *Paola Zarattini* and all the staff from the animal unit for their exceptional work.

I thank all the people form the PhD's administrative office of the *Department of Physics* of the *University of Trieste*, in particular *Rosita Glavina*, *Giulia Ghiretti* e *Ottavia Umani* for providing satisfactory feedbacks in very short time to every request, and for clear explanations and guidance throughout the complexity of bureaucracy.

I would like to thank *Prof. Pierangelo Gobbo* and his group, form the *Department of Chemical and Pharmaceutical Sciences* of the *University of Trieste*, for having hosted me in his lab during the development of protocols for substrates preparation.

The deepest gratitude is for my supervisor *Dr. Dan Cojoc* and my tutor *Prof. Orfeo Sbaizero* which supported my progresses step by step both professionally and emotionally, providing me with instruments and materials and making this wonderful experience possible.

I would also like to thank *Prof. Luisa Mestroni* from the *University of Colorado, Anschutz Medical Campus – Division of Cardiology* and *Prof. Carlin Long* from the *University of California, San Francisco* for the fruitful discussions about cardiac fibrosis.

Finally, I thank all my colleagues for the help, support and collaboration which have accompanied me along every step of this wonderful journey and from which I've learn that "team work is the key to success".

ABSTRACT

In the last decades lot of attention was conferred to mechanobiology, a multidisciplinary field bringing together concepts from biology, biochemistry, material science, engineering and biophysics. The main aim of this discipline is the understanding of the mechanisms of mechanotransduction in cells. This involves molecular events occurring at the nanoscale; therefore, nanoscience and nanotechnology are exploited for these types of studies. For these purposes, many tools and techniques have been developed for the visualization of cells and their structures enclosing: Optical Microscopy (Brightfield and Fluorescence), Digital Holographic Microscopy (DHM), and Atomic Force Microscopy (AFM). However, along with imaging setups, also mechanical stimulation instrumentations have been required and developed to perform mechanical probing. Among these there are: Quartz Crystal Microbalance (QCM), Micropipette Aspiration (MA), Atomic Force Microscopy (AFM) and Optical Tweezers (OT).

Since the investigation options are enhanced when more techniques are combined together, the application of multimodal imaging, as well as multimodal mechanical stimulation, and the combination of both, is deeply investigated within this Thesis.

The purposes of these techniques space from cell morphological, dynamical and viscoelastic characterization to force-induced calcium gating and mechanosensitive Piezo1 channel investigation.

First, a new combination of QCM and DHM techniques was adopted for the achievement of synergic results about morphological and viscoelastic properties of cardiac fibroblasts treated with cytoskeletal drugs. The sensitivity of QCM allowed the investigation of cell-surface interaction within a nanometric depth above the quartz sensor.

Subsequently, mechanical stimuli within a range of forces/pressures required for force-induced calcium gating through mechanosensitive ion channels were investigated in cardiac fibroblasts. Forces from piconewton up to nanonewton were employed by using OT and AFM respectively while cell response was followed by fluorescent calcium imaging. This multimodal investigation revealed important features about microenvironment-mediated mechanosensitive adaptation of fibroblasts which are of relevant importance for cardiac fibrotic mechanisms understanding.

A new multimodal methodology to investigate red blood cells (RBCs) mechanics was also proposed. In this work, MA was coupled to multimodal imaging enclosing both bright field and fluorescent calcium recording for accessing information on mechanical properties as well as Piezo1 channel functionality at the same time, for individual cells.

Finally, the application of DHM jointly with microfluidics in a novel measurement setup led to the validation of a new diagnostic method and instrument for fast bacteria analysis and urine label-free samples. The technique was compared to clinical gold standards (culture plate test and flow cytometry) showing faster analysis operation at lower cost for similar results. This fruitful project was developed in collaboration with Alifax srl.

In conclusion, the Thesis aims both to consolidate and expand already existing knowledge about cell mechanobiology proposing novel interesting results and suggestions about fibroblasts fibrotic mechanisms and stimulus-induced Piezo1 channel functionality both in fibroblasts and RBCs. The achieved results reported here, together with proposed innovative experimental approaches, may open new pursuable research ways in the mechanobiology field, and impact also the clinical landscape in terms of future diagnostic tools and targeted therapies.

PUBBLICATIONS

The results discussed within the Thesis are relative to three published, one accepted and one submitted articles, one conference abstract and poster presentations in one national and two international congresses. Importantly, one of the posters received the "Biophysical Society Poster Award" at the 14th EBSA congress in Stockholm, Sweden. Within the PhD program, I also contributed to other two works in progress which results are not enclosed in this Thesis. In conclusion, I annually presented the results at NanoCross congresses organized by the University of Trieste, PhD program in Nanotechnology and Jozef Stefan International Postgraduate School, Jozef Stefan Institute, University of Maribor, where I received the "Fernando Tommasini Award" for the most divulgative talk.

Articles in Peer Review Journals

Braidotti, N.; do R. B. F. Lima, M.A.; Zanetti, M.; Rubert, A.; Ciubotaru, C.; Lazzarino, M.; Sbaizero, O.; Cojoc, D. The Role of Cytoskeleton Revealed by Quartz Crystal Microbalance and Digital Holographic Microscopy. Int. J. Mol. Sci. 2022, 23, 4108.

Braidotti, N.; Chen, S.N.; Long, C.S.; Cojoc, D.; Sbaizero, O. Piezo1 Channel as a Potential Target for Hindering Cardiac Fibrotic Remodeling. Int. J. Mol. Sci. 2022, 23, 8065.

Gigli, L.; **Braidotti, N.**; Lima, M.A.d.R.B.F.; Ciubotaru, C.D.; Cojoc, D. Label-Free Analysis of Urine Samples with In-Flow Digital Holographic Microscopy. Biosensors 2023,13,789.

Braidotti, N.; Ciubotaru, C.D.; Rizzo, D.; Bergamo, L.; Bernareggi, A.; Cojoc D. Investigating mechanosensitive channels activation in concert with the mechanical properties of red blood cells. Discover Mechanical Engineering, accepted on 17/10/2023.

Braidotti, N.; Demontis, G.; Conti, M.; Andolfi, L.; Ciubotaru, C.; Sbaizero, O.; Cojoc, D. The local mechanosensitive response of primary cardiac fibroblasts is influenced by the microenvironment mechanics. (submitted)

Conference Abstract

Braidotti, N.; Demontis, G.; Andolfi, L.; Sbaizero, O.; Cojoc D. Piezo1 channel investigation in cardiac fibrosis precursor cells mechano-physiology, Eur. Biophys. J. 2023, 52 (Suppl 1):S1–S220.

Posters

Braidotti, N.; Cojoc, D.; Sbaizero, O. "Near-interface behavior of primary cardiac fibroblasts upon cytoskeletal actin alteration", XXV Congresso Nazionale SIBPA 2021, 28/06/2021 – 01/07/2021 (online), Società Italiana di Biofisica Pura ed Applicata (SIBPA).

Braidotti, N.; Cojoc, D.; Sbaizero, O. "Mechanical properties of cytoskeleton altered cardiac fibroblasts", 4th Annual Mechanobiology Symposium: Mechanobiology and Metabolism, 09-10/03/2022 (online), Center for Engineering MechanoBiology, University of Pennsylvania, Philadelphia.

Braidotti, N.; Demontis G.; Conti, M.; Andolfi, L.; Sbaizero, O.; Cojoc D. "Piezo1 channel investigation in cardiac fibrosis precursor cells mechano-physiology", 14th European Biophysical Societies' Association (EBSA) congress, 31/07/2023-04/08/2023, Stockholm, Sweden. (Award received)

Other works

Zanetti, M.; **Braidotti, N.**; Khumar, M.; Montelongo, E.; Sbaizero, O.; Mestroni, L.; Lazzarino, M.; Pena, B.; Andolfi, L. Investigation of heart's rheology by in vitro modeling of cardiac tissue using 3D cellular spheroids. (unsubmitted)

Farahzad, N.; Montelongo, E.; Kumar, M.; Travers, J.G.; Abdel-Hafiz, M.; Pascolo, G.; Lorelli, S.; Zanetti, M.; **Braidotti, N.**; Weir, R.; Mckinsey, T.; Taylor, M.R.G.; Park, D.; Magin, C.M.; Regensteiner, J.; Mestroni, L.; Sbaizero, O.; Peña, B. Assessment of tensile and compressive stress in sex-specific cardiac Fibroblast: in vitro Modeling of Cardiac Biomechanics. (unsubmitted)

Awards

Biophysical Society Poster Award

Braidotti, N.; Demontis G.; Conti, M.; Andolfi, L.; Sbaizero, O.; Cojoc D. "Piezo1 channel investigation in cardiac fibrosis precursor cells mechano-physiology", 14th European Biophysical Societies' Association (EBSA) congress, 31/07/2023-04/08/2023, Stockholm, Sweden.

"Fernando Tommasini Award" for the most divulgative talk

Braidotti, N.; Demontis G.; Andolfi, L.; Sbaizero, O.; Cojoc D. "Piezo1 channel investigation in cardiac fibrosis precursor cells mechano-physiology", NanoCross congress, 21-23/02/2023, University of Trieste, PhD program in Nanotechnology and Jozef Stefan International Postgraduate School, Jozef Stefan Institute, University of Maribor.

TABLE OF CONTENTS

Part I

INTRODUCTION

1 MORPHOLOGICAL AND MECHANICAL PROPERTIES OF LIVING CELLS

The investigation of morphological and mechanical properties of living cells represents one of the main topics covered by mechanobiology, which is an emerging and multidisciplinary field at the interface with biology, engineering, chemistry and physics. Therefore, before talking about cell properties, with a particular engineering approach, it is worth introducing the mechanobiology objectives and the technical language used with cells. Thereafter, cell mechanical properties, and related cellular elements involved in, are presented before moving the attention to mechanotransduction processes. The experimental section of the Thesis is focused on cellular mechanotransduction; therefore, providing a thorough explanation on its role and importance for both physiological and pathological states is needed.

1.1. MECHANOBIOLOGY

About 20 years ago the observations of a force-dependent maturation of focal adhesion in stiff environment or under mechanical forces signed the origins for the mechanobiology field. Since then, physics as well as mathematical models became integral part for supporting the progress in this field [1]. Since the main aim of the discipline resides in the investigation on the role of physical forces and related cell and tissue mechanical properties changes, knowledges from material science and engineering have also been involved [2]. It is known that cells and tissue are subjected to forces which allow both physiological and pathophysiological processes. Among the main elements involved in force perception there are mechanosensitive channels with focal adhesion and cytoskeleton also playing an essential role. Moreover, cells are also able to exert force on substrates by themselves and this expands once more the field to be investigated.

Despite the precise aim of biologists which is focused on the investigation of pathways involved in the regulation of signal transduction and gene expression, the measurement and manipulation of such forces remain challenging from a biological point of view.

This gap is filled by the competences from physicists, material scientists and engineers [2]. This is the reason why in most of the mechanobiology studies, terms such as “stiffness” or “rigidity” referred to cell, tissue or substrate properties are adopted [3]. However, the intrinsic origin and meaning of these concepts belongs mainly to the material engineering field rather than the biological or physics one.

1.2. MECHANICAL PROPERTIES OF MATERIALS

The term “stiffness” is intuitively addressed to the resistance of a material to deformation when it is subjected to mechanical forces [3]. Intrinsically, this material property is measured through the elasticity modulus or Young’s Modulus (E) which is defined by:

$$E = \frac{\sigma}{\varepsilon}, \tag{1.1}$$

where the σ and ε are respectively the tensile stress and the strain in the linear elastic region shown in the stress-strain curve in Figure 1.1. Such curve is obtained by testing samples with the Tensile Test [4].

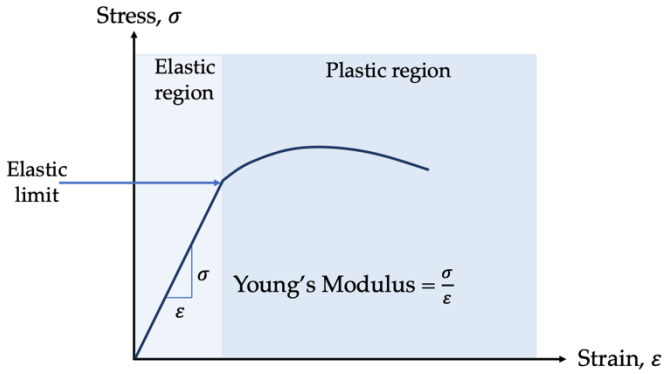

Figure 1.1. Stress-Strain curve for a typical material under tensile stress.

The elastic region corresponds to the region in which the deformation is reversible; thereafter, once overcame the elastic limit, the deformation is permanent.

The term "deformation" refers to the unitless value of strain while "stress" is given by the force normalized by the initial area [3]:

$$\sigma = \frac{F}{A_0}, \tag{1.2}$$

The curve reported in Figure 1.1 considers the nominal stress. However, after reaching the maximum value in the plastic region (tensile strength), the samples' section starts to reduce and therefore it elongates with lower required force. On the other hand, the real tension calculated considering the real instantaneous area continues to increase respect to the nominal one.

The stress-strain curve is a typical representation of a generic ductile material behavior (it can be metallic or polymeric) when it is tested by tensional forces application.

However, materials can be subjected also to shear forces, as shown in Figure 1.2. In this type of deformation, the shear stress is given by:

$$\tau = \frac{F}{A_0}, \tag{1.3}$$

where F is the force acting on the area A_0.

At the same time a definition for shear deformation also exists and is given by:

$$\gamma = \frac{a}{h} = tan\theta, \tag{1.4}$$

where the mining of *a* and *h* is shown in Figure 1.2.

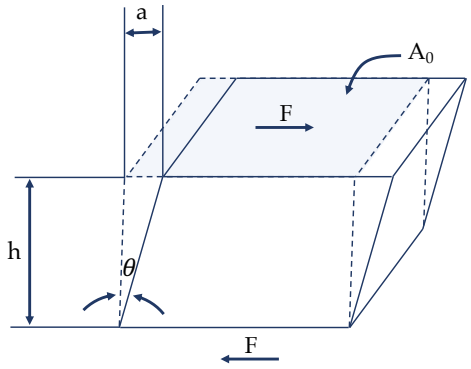

Figure 1.2. Shear stress representation

As for tensile deformation, also in the shear elastic region the Shear Modulus (G) can be introduced:

$$G = \frac{\tau}{\gamma}. \tag{1.5}$$

This modulus describes the material resistance to shear deformation and is related to the Young's Modulus following the formula [5]:

$$G = \frac{E}{2(1+\nu)}, \tag{1.6}$$

where ν is the Poisson's ratio, which for isotropic materials is commonly ≈ 0.3. Therefore, the approximation: $G \approx \frac{3}{8}E$ holds.

It is important to note that the properties described above belong only to those materials defined as "elastic solids" in material science, i.e. materials which can be just described by a spring like model [5, 6]. However, another set of materials exists which possesses only partially elastic properties. These are defined as "viscoelastic" materials, due to the fact that they exhibit both viscous (dashpot-like) and elastic (spring-like) characteristics when subjected to deformations, which place them to fill the gap between elastic solid and Newtonian liquid [7]. Among the materials displaying significant viscoelastic effects there are: food, synthetic polymers, wood, soil and biological soft tissue as well as metals at high temperature.

This class of materials owns complex behaviors. In fact, the relationship between stress and strain depends on time. The discipline which studies such materials is "rheology" and it makes use of several types of investigations for achieving the viscoelastic characterization of them.

A deep description of the rheological techniques, as well as the meaning of rheological parameters, is out of the scope of this Thesis. However, it is opportune to note that they are based on complex equations constituted by the two components (elastic-like and viscous-like). Moreover, depending on several factors (e.g. temperature, cross-linking, rate of deformation), viscoelastic materials are able to exhibits a prevalent elastic-like behavior or a viscous-like one, often showing also a transition from one state to the other [8]. A very versatile method for the characterization of such materials is the dynamic mechanical measurement [9]. It is used to study the tendency to flow (viscosity) and the stiffness (modulus), and consists in the application of a small-amplitude oscillatory motion to a material placed in contact with and between two disks, one oscillating and one fixed [8, 10]. The outcoming component in phase with the strain determines the elastic (or storage) modulus (G'), which corresponds to the elastically stored energy, whereas the out of phase component defines the viscous (or loss) modulus (G'') and corresponds to the viscous dissipated energy [8]. The ratio between the loss and the storage modulus is known as "damping" and is denoted by [10]:

$$\tan\delta = \frac{G''}{G'}. \tag{1.7}$$

It measures the dissipation, or loss of mechanical recoverable energy, or internal friction in a viscoelastic system. It is a dimensionless number determining the solid or liquid prevailing behavior. For an ideal elastic material, the viscous behavior portion is zero, and the loss factor (tanδ) is zero. On the other hand, samples with an exclusive viscous property have a loss factor that converges to infinity. Between these two border conditions, materials with viscoelastic properties find place for which high tanδ values correspond to a material that has a high, nonelastic strain component, while low ones are representative of a more elastic material [11, 12].

1.3. MECHANICAL PROPERTIES OF BIOLOGICAL MATERIALS

Material Science and Engineering had been focused for years on the classical material classes: metals, polymers, ceramics and composites.

However, along with an emerging interest in biological materials since 1990s, a new field of application was highlighted [13]. A major relevance was acquired by tissue and organ mechanical properties characterization as a consequence of lifestyle changes and aging world population [14]. Since our body is composed by several organs and tissues which are involved in different functions and exhibit different mechanical properties, a first classification can be made on the macroscopic ability to resist mechanical loading:

- soft tissues: neural tissues and most abdominal organs (e.g. kidney, heart, intestine);
- hard tissues: cartilage, ligament, tendon and bone.

Within the two subclasses the Young's Modulus ranges from few kPa to MPa. Indicative stiffness values for some biological living tissues are reported in Figure 1.3 [14].

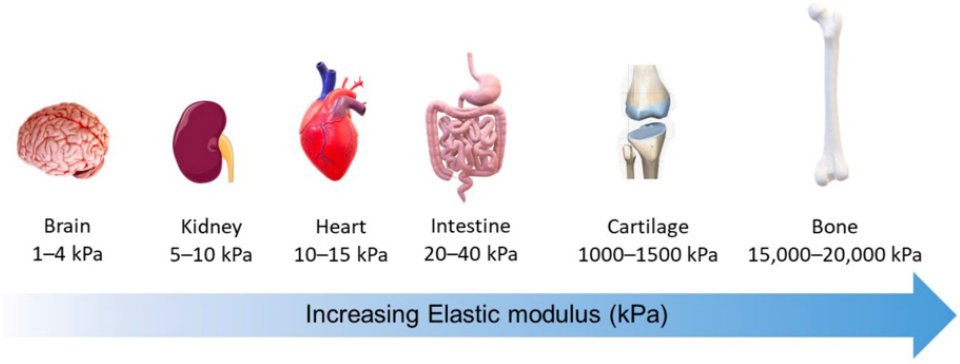

Figure 1.3. The stiffness of some living tissues [14].

However, as already mentioned, the Young's Moduli are only indicative. In fact, mechanical changes within individual tissues can occur as a consequence of chronological age (physiological condition) and the development of diseases (pathological condition) [15]. A typical and broadly investigated pathological example is the change in mechanical properties during the development of solid tumors which are known to be stiffer than the non-transformed tissue counterpart [16]. On the other hand, also nontumorigenic pathologies are characterized by similar changes. In this context, fibrosis had acquired a lot of attention as it involves several organs and implicates serious consequences. In particular, the increased stiffness in fibrotic tissue was studied in the lung [17, 18], kidney [19], liver [20] and in the heart [21]. The last one will be discussed in detail further in this Thesis.

Even if absolute stiffness values are organ-dependent, the fibrotic mechanisms characterizing such pathological condition are similar among the tissues. Basically, fibrosis is characterized by the formation and deposition of excess fibrous connective tissue, resulting in progressive architectural

remodeling in nearly all tissue and organs [22]. A schematic representation of the fibrotic remodeling in different organs is reported in Figure 1.4.

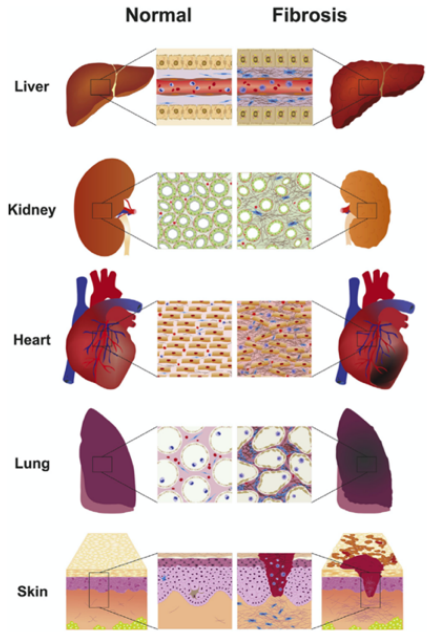

Figure 1.4. Representation of common characteristics of organ fibrosis for different tissue types [22].

As for engineering materials, whose mechanical properties are controlled by microstructure, the architectural remodeling of the tissue is the leading cause of the alteration of its mechanical properties [15].

However, to obtain deeper information about tissues mechanical properties and processes involved in properties alteration, it is necessary to move the attention down to building blocks composing the tissues of organs: the cells.

1.4. CELLS MECHANICAL PROPERTIES

Cells are complex systems exhibiting both elastic and viscous properties. Moreover, cells are highly dynamic; in fact, continuous remodeling of their internal structure occurs which is accompanied by changing in their mechanical properties [23]. Despite such complexity, they can be simplified by theoretical models and managed as classical materials for characterization purposes, allowing the measurement of their mechanical properties. For example, it is possible to quantify the cell deformation in response to the mechanical force over the time, and, as for classical materials, depending on different deformation modes (e.g. linear extension, shear deformation), different parameters can be achieved (e.g. Young's Modulus, Shear Modulus) [24]. There are many ways for mechanical properties assessment by which is possible to obtain information on whole cell Young's Modulus, deformability, viscoelastic properties, but also separate contributions coming from isolated cellular elements respect to the whole [24, 25]. Some of these methods will be discussed in more detail in this Thesis.

It had been demonstrated that cell cytoskeleton largely determines such mechanical properties [26] and this is the reason why a lot of efforts have been spent on its investigation among several cell types.

1.4.1. Cell Cytoskeleton

The cytoskeleton is a dynamic, heterogenous biopolymeric network consisting of three major filamentous components: microfilaments, microtubules and intermediate filaments. The basic structural elements of these are linear polymers of actin, tubulin and vimentin proteins respectively [23, 27].

By protein purification and rheological measurements, viscoelastic characterization of single biopolymer network had been achieved. In a very interesting work [27] such experiments had been carried out with the following conclusions:

- filamentous actin (F-actin) is much more resistant to deformation (has higher shear moduli) than either microtubules and vimentin filaments;
- microtubule network has the greatest deformability with loss of elasticity at 50 % of strain and an outcoming liquid-like behavior;
- vimentin network is easily deformable but does not lose elasticity;
- F-actin network showed the highest storage modulus (G');
- F-actin network showed a complete recovery after the application of a constant stress (creep);
- microtubule and vimentin filaments exhibited an unrecoverable strain typical of viscous flow.

Based on these experimental results it is clear that F-actin possesses the greatest resistance to stress and this is the reason why cells have a cortex made up by F-actin which resists against environmental stresses. Actin cortex is not the only one structure resulting from actin assembly; in fact, actin is involved also in filipodia, lamellipodia and stress fibers [28, 29].

An illustrative representation of primarily types of F-actin structures is reported in Figure 1.5.

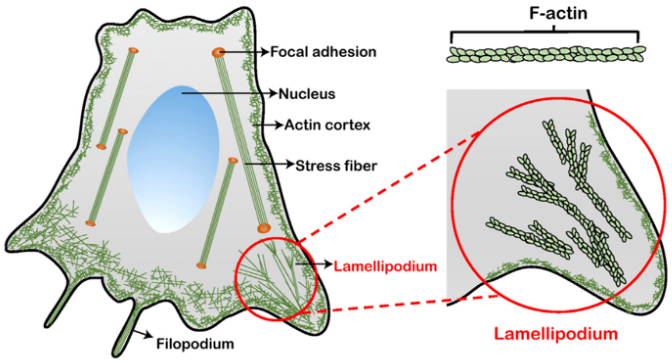

Figure 1.5. Primarily types of F-actin structures enclose actin cortex, stress fibers, lamellipodia and filopodia [29].

The cytoskeleton is a vital cellular component involved in several processes, and therefore, its dysfunctions can be translated into serious cellular functional impairments [30].

In fact, many works highlight a correlation between some pathologies and altered cell cytoskeleton [30-34] and this justifies the consistent interest in investigating cell behavior under controlled artificial cytoskeletal alterations. The understanding of consequences reflected on cell mechanical properties under impaired cytoskeleton is propaedeutic to focus the attention on pathological cells from patients, with the prospect of future possible clinical application as diagnostic tool and treatment protocols. An example of selective alteration of actin and microtubule in cardiac fibroblasts and implicated morphological, viscoelastic and adhesive property changes will be presented in the experimental section of the Thesis (Chapter 4).

The main role of cytoskeleton is to contribute to the cell rigidity [35]. However, it is implicated also in the adhesion process to the external environment through binding proteins, which mediate its connection with the extracellular matrix (ECM) [36]. Adhesion sites are of extremely importance for

sensing and signaling substrate properties changes, which collocate them among the elements required for mechanotransduction processes [37].

1.5. MECHANOTRANSDUCTION

Although it is accepted that cells are subject to mechanical cues the mechanisms of force perception are yet to be unravel. Cells can convert physical forces into biochemical signals which culminate into the cellular response by the activation of intracellular transduction pathways. This process is called "mechanotransduction" and it is one of the main aspects covered and investigated by mechanobiology [37, 38]. However, such process involves molecular events occurring at the nano level, therefore the deep investigation of these mechanical cues and implicated cellular responses remained elusive until nanotechnology has provided new set of suitable tools [39]. On the cellular level, the mechanotransduction process is able to modulate several functions such as protein synthesis, secretion, adhesion, migration, proliferation, viability and apoptosis. Therefore, it is logical to think that defects in mechano-elements can lead to adverse outcomes. At the same time, a proper mechanotransduction process in altered environmental conditions can induce dysfunctional consequences as well, as a result of its environment-mediated amplification or reduction [40].

There are several elements involved in the mechano-sensing and -transduction process. First, the cytoskeleton is one of the candidates. In particular, the cortical actin network underlying the plasma membrane is sensitive to mechanical stimulation at the cell surface [41]. Due to its dynamic behavior, quick remodeling occurs in response of plasma membrane changing in tension, shear or bending [41].

Secondly, the maturation of small focal adhesions (FAs) into large ones, anticipated before in the Section 1.1, as a consequence of mechanical loading (e.g. increased cell contractility or local mechanical stimuli) [42], had suggested their role as mechanosensitive elements. In addition, their position at the interface between cell intracellular and extracellular space likely plays a central role in sensing mechanical signals both from outside and inside [43].

Moreover, since within the intracellular space the cytoskeleton and the nucleus are engaged through the "linker of nucleoskeleton and cytoskeleton" (LINC), mechanical signal can be readily transmitted from FAs to the nucleus. In this way the so called nuclear mechanotransduction can occur leading to a very efficient way for translating mechanical signals into changes in gene expression [41].

However, even if there are several evidences about the role of these mentioned mechanosensitive elements in sensing and transducing mechanical cues; among the investigated mechano-sensors an essential work is done by the mechanosensitive ion channels (MSCs).

1.5.1. Mechanosensitive ion channels

Mechanosensitive ion channels are mechanosensitive elements directly activated by stress applied to the lipid bilayer or its associated nonmembrane components and able to convert physical stimuli into electrical signals [44]. They allow selective or non-selective ions transport which occurs because of channel activation. This involves a transition from a resting-closed state to an activated-open state that conducts an ionic current [45]. The current knowledge highlights two possible mechanisms, and related models, for channel gating: the bilayer (or force-from-lipid) model and tether (or force-from-filaments) model [45-47].

The first one is based on channel activation because of force applied to the lipid bilayer generating membrane tension variations. On the other hand, as the name suggests, the tether model implies that the channel is physically tethered to extracellular matrix or intracellular accessory structures (e.g. cytoskeleton) for mechanogating [46].

It is important to note that the previously discussed cytoskeletal dynamicity can induce variations in the bilayer tension, even in the absence of external mechanical stimuli [48]. Moreover, cells are able to actively generate forces [49] which are used for probing the stiffness of the ECM and serving as key regulator of cell signaling, function and fate [50, 51]. Therefore, it is likely that the source of

forces for channel activation can also come from the inside, and once generated, it is subsequently propagated out of the cell. Thus, even in the absence of external mechanical stimuli the inside-out mechanotransduction can take place representing an active mode for channel activation rather than a passive one [45].

Several channels' families have been investigated so far, however in the last decade a lot of attention was gained by the recent discovered mechanosensitive ion channel Piezo1.

1.5.2. Piezo1 channel

The following paragraph is taken and adapted form a review published as first author: *Braidotti, N.; Chen, S.N.; Long, C.S.; Cojoc, D.; Sbaizero, O. Piezo1 Channel as a Potential Target for Hindering Cardiac Fibrotic Remodeling. Int. J. Mol. Sci. 2022, 23, 8065.*

Piezo1 is a recently discovered mechanosensitive or stretch-activated ion channel. Coste et al. in 2010 discovered the potential of this channel, expressed by several mammalian cells, and used to translate mechanical force into biological signals [52]. Piezo1 is a non-selective channel activated by pressure, hence the Greek word "Piezo". It was observed to be permeable to Na^+, K^+, Ca^{2+}, and Mg^{2+} with a slight preference for Ca^{2+} [52]. Despite the *in vitro* chemical activation of Piezo1 by Yoda1 or Jedi1/2 [53, 54], among the other mechanosensitive channels, Piezo channels are the only ones to be gated primarily by mechanical stimuli instead of chemical or physical ones [55]. In 2015, Yoda1 was first identified as a synthetic Piezo1-agonist compound that elicits Ca^{2+} flux selectively in Piezo1 in the absence of externally applied pressure [53]. Even if this agonist is the most used for channel studies purposes, in 2018, a novel set of Piezo1 chemical activators, termed Jedi (Jedi1 and Jedi2), was discovered [54]. While these offer the possibility to study the channel activation, there are currently very limited inhibitors that are specific for Piezo1 available. Non-specific antagonists of other mechanosensitive ion channels, such as streptomycin and spider peptide toxin (GsMTx4), do work for Piezo1 but not in isolation [56].

The Piezo family is composed of Piezo1 and Piezo2. They are both mechanically activated cation channels mainly located at the plasma membrane. However, Piezo1 was also detected in the endoplasmic reticulum, nucleus, and mitochondria [52, 57]. They were found to be involved in many mechanotransduction pathways such as touch sensation, proprioception, nociception, vascular development, and breathing [58]. Up to now, Piezo2 has been considered to belong mainly to sensory neuron biology [59, 60], while Piezo1 was shown to be expressed by many different cell types [61].

The Piezo1 structure is characterized by a three-blade propeller architecture [62] with an extracellular domain. The so-described structure consists of an in-plane dimension of about 200 Å and 140 Å in section [58]. The transmembrane helices have a pronounced bend culminating in a spherical dome, with an estimated dimension of 390 nm^2 [63], projected into the cell, which is supposed to be responsible for the local membrane distortion even outside the channel perimeter [58, 62, 63]. A simplified representation is shown in Figure 1.6, which was adapted based on Haselwandter and co-workers' illustrations [63]. Based on energy calculation, it is believed that the membrane deformation caused by this large protein leads to prefer a shape associated with the lowest energy. The work required to deform the membrane can be calculated from:

$$G_M = \frac{1}{2} K_b \int (c_1 + c_2)^2 dA + \gamma \Delta A \,, \tag{1.6}$$

where K_b is the membrane bending modulus, γ is the membrane tension, c_1 and c_2 are the principal curvatures of the surface, and ΔA is the decrease in in-plane area when the membrane is deformed from its planar configuration [63]. As the equation suggests, it is possible to correlate the membrane deformation imposed by Piezo to only three physical properties (Figure 1.6). These parameters are the Piezo shape (basically its radius of curvature), the membrane bending modulus, and the membrane tension.

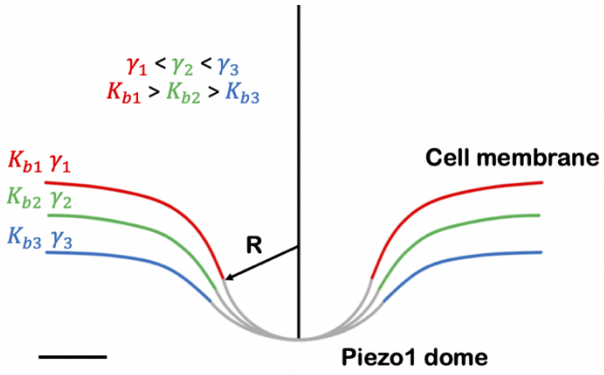

Figure 1.6. Section view of Piezo dome (gray) and deformation imposed on the cell membrane (red, green, blue). The three physical parameters and their relative relationships involved in the regulation of membrane shape are reported: R (radius of curvature of the dome), K_b (membrane bending modulus), and γ (membrane tension). Scale bar: 10 nm.

When tension is applied to the membrane, the energy is, in turn, minimized if Piezo flattens (rise in dome radius of curvature), favoring its opening state. Therefore, in relation to Figure 1.6, if the red curve is considered representative of the resting condition (closed state), the gradual tension application is described by the green followed by the blue curve, where the cell membrane appears almost completely flattened. For a detailed description of the energies involved, please refer to the recently published work by Haselwandter and co-workers [63].

Based on the aforementioned energetic discussion, force-induced membrane tension opens the channel allowing the permeation of cations [48]. However, since Piezo1 was discovered, force-from-lipid and force-from-filament models have been debated in its regard. However, the second one is nowadays getting even more attention, and recently, the tethered connection which links Piezo1 to the cytoskeleton was discovered. This one was found to reside within the E-cadherin/β-catenin/F-actin mechanotransduction complex [64] and provides current for the long-range propagation of membrane tension perturbation. Therefore, as previously mentioned, due to the well-known ability of cells to exert endogenous traction forces, increases in local membrane tension can be generated from the inside causing channel opening [51, 64]. At the same time, a local membrane stimulus can be transmitted across the cell through cytoskeletal actin for the activation of far-placed Piezo1 channels. The upstream signaling responsible for the generation of traction forces that activate Piezo1 involves the phosphorylation of Myosin II by Myosin light chain kinase (MLCK). Moreover, since Ca^{2+} regulates MLCK itself, it likely represents the driving force for the feedback loop for which traction forces-induced Piezo1 activation is enhanced as a consequence of Piezo1-dependent calcium signaling [51]. As anticipated, cell-generated traction forces are an absolute prerequisite for probing the stiffness of the ECM and regulating, in turn, cell signaling and function [45, 51]. Therefore, these findings likely highlight the Piezo1 role for the downstream as well as the upstream signaling in sensing the external mechanical environment.

1.6. FIBROTIC MECHANICAL ENVIROMENT

Based on the previously discussed matter, it becomes clear that substrates mechanical properties on which cells adhere are determinant for cellular function. In fact, the signaling of mechanical cues by the mechano-elements above described proceeds a cellular response which regulates in turn several factors (e.g. protein synthesis, secretion, adhesion, migration, proliferation, viability and apoptosis) [40].

In particular, the already mentioned tissue stiffness changes during both physiological or pathophysiological conditions are sensed by cells and transduced into biological responses including cytoskeletal reorganization, traction forces establishment, FAs maturation and channels activation.

Moreover, cells can contribute themselves to microenvironment mechanical property variations leading to a feedback loop culminating in an amplificated mechanotransduction. Therefore, to obtain better knowledge about the leading cellular mechanisms and implicated drawbacks, several *in vitro* experiments have been carried out. In this regard, fibroblasts have been widely investigated [65-67]. In fact, they play a key role in fibrosis which, as discussed before, is a pathological tissue condition associated to substantial mechanical changes.

Fibroblasts are highly dynamic cells able to undergo a phenotypic transition into an activated form called "myofibroblasts" because of proinflammatory or mechanical stimuli. This is accompanied by an increased cell contractility due to cytoskeletal reorganization and α-smooth muscle actin (α-SMA) incorporation into actin stress fibers [68, 69]. Moreover, between the main myofibroblasts characteristics there is also an increased production of ECM proteins which makes them essential players during wound healing process. Quiescent fibroblasts are responsible for the maintenance of a balance between degradation and production of ECM in normal physiological conditions [68-70]. However, the enhanced ECM accumulation had been demonstrated as an essential feature for injury replacement and tissue regeneration in several tissues such as skin [71], lung [72] and heart [73]. Despite the absolute necessity of fibroblasts on injured areas, their persistence beyond the physiological repair timepoint become pathologic and leads to fibrosis with subsequent adverse outcomes [74]. On the top of implicated drawbacks, there is a feedback loop which is established because of stiffening-induced ECM excessive production. In fact, the stiff mechanical environment becomes suitable for additional fibroblasts activation, enhancing once more the stiffness by further ECM generation, and promoting fibrosis [75]. The impairment of organ functions as a consequence of fibrosis is associated with high morbidity and mortality [76]. This is the reason why many efforts have been spent on this topic by researchers and clinicians all over the world. Unfortunately, despite the work done for developing new efficient therapeutic strategies, up-to-date there are no specific antifibrotic therapies available in any organ [76]. Even if studies based on animal models raveled some possibilities in reversing fibrosis, these cannot be directly translated into human therapies due to the physiologic and genetic differences [77, 78]. Moreover, the poorly understanding of pathophysiological mechanisms established in the fibrotic process limit, to date, its successful treatment [21]. For this reason, many researchers are pushed on a deep investigation into these mechanisms, starting from *in vitro* cell cultures for understanding cellular implicated processes first and highlighting suitable target for the successful development of precision therapies.

An extensive study has been carried out in this regard by collecting evidences form literature and, finally, suggesting a novel antifibrotic approach in the specific context of cardiac fibrosis. The preclinical work, hypothesis and discussions are reported in [68]. The main conclusion obtained can be summarized in the following statement: Piezo1 could play an important role in cardiac fibroblasts biology and offer a unique opportunity to modify the maladaptive cardiac remodeling in response to injury, ultimately leading to heart failure.

In fact, in the course of the review [68], Piezo1 is highlighted as a possible driving force for fibrotic remodeling progression. It increased expression and activity because of fibroblasts activation had been suggested as the leading cause of subsequent cascades able to favors the chronicity of the pathology. Therefore, the possibility of restoring its physiological activity was suggested as a new way for interrupting the positive feedback in which its increased activity may promote ECM remodeling in a way in which its stiffness-induced stimulated activity is again enhanced. In addition, its involvement in cytokines regulation, the mechanism by which it affects healthy fibroblasts even distant from the injured zone, may open the possibility of slowing down the organ-wide reactive fibrosis. Finally, we proposed that Piezo1 could be used as a biomarker, for discriminating the aggressiveness of cardiac fibrosis, as well as a beneficial therapeutic target. However, even with the promise of the reported observations on the benefit of inhibiting Piezo1 activity, more studies need to be carried out starting from *in vitro* experiments. Studying cells from fibrotic human organs is just one possible way. However, mimicking physiological and pathophysiological stiffness conditions for

manipulating cellular states is nowadays possible thanks to biomimetic materials. These offer a valid comparative tool to monitor cellular behavior by reproducing health and pathological mechanical environments.

1.7. BIOMIMETIC MATERIALS

"The study of the formation, structure, or function of biologically produced substances and materials (as enzymes or silk) and biological mechanisms and processes (as protein synthesis or photosynthesis) especially for the purpose of synthesizing similar products by artificial mechanisms which mimic natural ones." This was the definition which accompanied the first public appearance of the word "biomimetic" in Webster's dictionary in 1974 [79]. The term "biomimetic" has a Greek origin: 'bios' meaning life and 'mimetikos' meaning imitative [80].

It is well known that the nature inspired the human being making the technological development possible [80]. In fact, a proof of that is the discovery of biomimetic materials which offered the opportunity to mimic salient features of ECM with promising achievements. From a biological point of view, ECM is the non-cellular component of tissues composed by proteins, polysaccharides, growth factors, signaling molecules, proteases, and water [81].

However, from an engineering perspective, ECM is defined as the main structural component of soft tissues. It is basically a hydrogel; thus, a biphasic viscoelastic material composed of a solid polymeric network interpenetrating an aqueous solution [82].

Overall ECM mechanical properties depend on the mechanical contribute of specific network components. For example, collagen is responsible for tissue stiffness and strength, while elastin endows extensibility and resilience. However, the characteristics of ECM composition and self-assembled hierarchical architecture, and subsequent mechanical properties, are tissue specific [82, 83].

The behavior of the solid phase can be related to the tissue's elastic properties, usually described by Young's Modulus. On the other hand, the interfibrillar liquid, mainly composed by water and solutes such as glycosaminoglycans, proteoglycans, and glycoproteins, is characterized by its resistance to flow, which is quantified through viscosity [82].

Engineers have taken inspiration from such properties for developing bioinspired materials matching the features of native ECM. Therefore, numerous engineering substrates with controllable parameters have been proposed for responding to current challenges. One of the problems which are still open regards the tissue repair. Tissue engineering, an emerging inter-discipline which integrates material science and engineering, is focused on this and recognized hydrogels as possible key players in the field. Their high-water content, hydrophilicity, good biocompatibility, ability to simulate ECM environment and to control drug release make them excellent scaffold materials [84].

Hydrogels can be prepared starting from natural polymers (e.g. gelatin, collagen, fibrin, silk fibroin, hyaluronic acid (HA), chondroitin sulfate (CS), alginate, chitosan) or synthetic polymers (e.g. poly(ethylene glycol) (PEG), poly(vinyl alcohol) (PVA),poly (N-isopropylacrylamide) (PNIPAM), polyacrylamide (PA)). Natural polymers possess high biocompatibility, biodegradability, and similar microenvironment to that of native tissues. On the other hand, synthetic polymers exhibit high controllability, reproducibility, and good mechanical properties. However, hybridization of synthetic polymers with natural materials have emerged as an easy-going approach to integrate the advantages of natural and synthetic component [85].

From a structural point of view, a hydrogel consists of a three-dimensional (3D) polymeric network formed by physical or chemical crosslinking. In the case of physical gels, also called "reversible", networks are held together by molecular entanglements and/or secondary forces. In contrast, chemical gels, also called "permanent", consist of covalently cross-linked networks [86].

However, chemical crosslinked hydrogels have gained more attention from researchers than physical crosslinked ones due to the variety available and easy control of the substrate stiffness with superior physiological stability [83]. In fact, chemical hydrogels with tuned elastic properties can be easily obtained by changing gel composition and one widely used example is polyacrylamide hydrogel [83, 84].

1.7.1. Polyacrylamide hydrogel

Polyacrylamide (PA) is one of the most used substrates for exploring cellular response to substrates stiffness [87-89]. It is obtained from the crosslink of acrylamide monomer with a suitable bifunctional crosslinking agent, most commonly, N,N'-methylenebisacryl-amide (bisacrylamide) [83, 90]. Gel polymerization is usually initiated with ammonium persulfate which acts as a source of free radicals. Then, the reaction rate is accelerated by the addition of a catalyst such as N,N,N′,N′-tetramethylethylenediamine (TEMED) which initiates the redox radical polymerization of PA [90, 91].

A schematic representation of PA polymerization is reported in Figure 1.7.

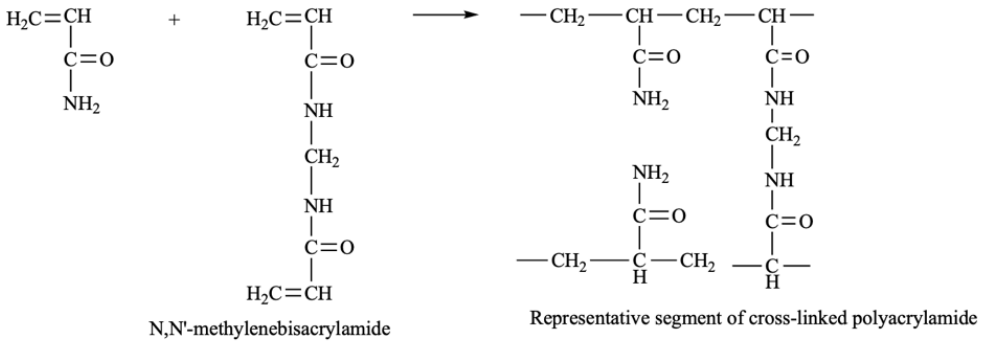

Figure 1.7. Acrylamide polymerization layout [90].

PA hydrogels stiffness ranges from 2 kPa up to 665 kPa, and it can be regulated by changing the constituent concentration and the proportion of acrylamide in the final specimen [83].

R. Subramani and colleagues performed a rheological investigation into PA hydrogels prepared by mixing acrylamide and bisacrylamide in different concentrations. They observed a reduction in G' as a consequence of decreasing concentrations of crossinker (bisacrylamide), acrylamide or both [92]. In addition, tanδ was always highly below 1 confirming that PA stresses are governed by elastic instead of viscous effects for the tested frequency range [92, 93]. Finally, through AFM the local Young's Modulus was evaluated showing the highest stiffness by using the highest acrylamide and crosslinker concentrations [92].

Due to PA controlled mechanical properties, this hydrogel has been widely used for studying mechanotransduction processes in several cell types. Brest cancer cells (MDA-MB-231) [94], tumorigenic (MCF7) and non-tumorigenic (MCF10A) epithelial cells [95, 96], epidermoid carcinoma cells (A431) [95], myoblast cells [97], human umbilical cord mesenchymal stem cells [98], human mesenchymal stem cells [99], glioblastoma stem cells [16] are just some examples of cell types investigated by using PA hydrogels. However, a lot of work was done by using fibroblasts form different origin: rat lung and subcutaneous fibroblasts [100], human lung fibroblasts (CCL-151) [101], mouse embryonic fibroblasts [102-105], dermal fibroblasts [106], and cardiac fibroblasts [107-109].

Despite PA usefulness in mechanotransduction studies, the main problem in working with is related to its bio-inert behavior. PA lacks surface receptors or cell interaction sites; therefore, conjugating adhesive proteins to its surface is mandatory for cell attachment [110].

In addition, PA is hydrophilic and repels protein adsorption by steric hindrance effects. Thus, in order to bind proteins and promote cell adhesion, the surface of polyacrylamide must be functionalized with coupling chemical species [111].

There are basically two main methods for patterning ECM on PA hydrogel [110, 111]:

1. Activation of the gel for covalent attachment of proteins to activated regions.
2. Copolymerization of ECM proteins in the gel.

Even if the first alternative results the most expensive one due to the involvement of costly chemical compounds, which are unstable in aqueous media and in the presence of oxygen, the final hydrogel stability makes it suitable for long-term culture experiments respect to the second approach [110].

The most successfully used chemical crosslinker is sulfosuccinimidyl-6-(4'-azido-2'-nitrophenylamino) hexanoate (sulfo-SANPAH). It is photoactivable heterobifunctional reagent activated by ultra-violet (UV) light containing an amine-reactive N- hydroxysuccinimide (NHS) ester and a photoactivatable nitrophenyl azid [111]. The photoactivatable region of sulfo-SANPAH binds polyacrylamide and the sulfosuccinimidyl group at the other end reacts with protein primary amine groups (Figure 1.8). In such way, PA activation and ECM proteins binding can be achieved for successive successful cell culture.

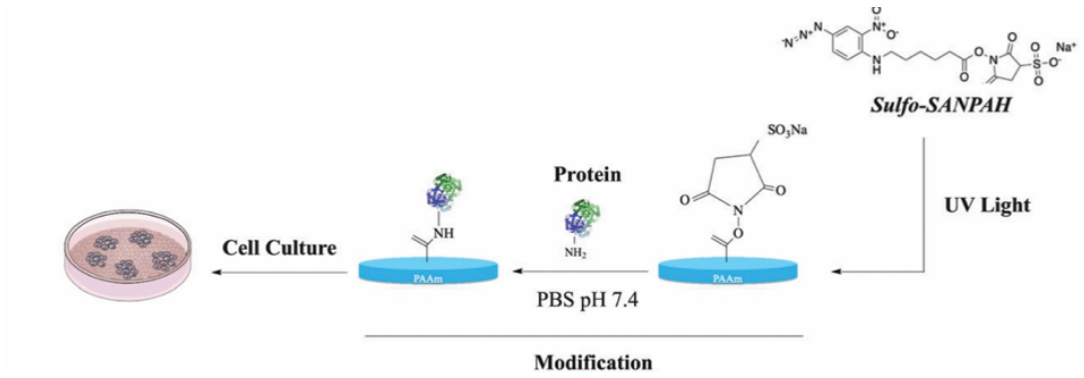

Figure 1.8. Schematic representation of PA functionalization with proteins through sulfo-SANPAH substrates activation [110].

1.7.2. Polydimethylsiloxane substrates

Despite the advantages cited above for hydrogels, PA substrates fabrication results often costly, time consuming as well as pretty toxic for users. Moreover, the stability in culture and in storage condition is limited, forcing user to avoid substrates preparation in advance for future use and limit the experiments to short culture periods. However, there are other materials available allowing users to mimic the elastic character of cell microenvironment in a more user-friendly, biocompatible, long stability, timesaving, and cheap way.

Polydimethylsiloxane (PDMS) is an example of a widely used material for developing substrate platform in mechanobiological and microfluidic applications [112-114].

PDMS substrates are generally produced by mixing silicone elastomer base with curing agent. The mixture is then degassed and poured into the desired vessel (e.g. Petri dishes) and heat-cured.

However, the obtained substrates are high hydrophobic and prevent cell adhesion; therefore, substrates can be easily activated with plasma oxygen and then functionalized with ECM proteins, without the requirement of specific treatment with any chemical and toxic compound. Thanks to the transparency of PDMS, microscope observation both in brightfield and fluorescence are permitted, making these substrates compatible with most of the biological experiments [115, 116].

Moreover, in order to tune the elastic properties, the base to curing ratio content can be adjust, similarly to PA hydrogels [117], thus allowing to obtain a broad range of Young's Moduli from few kPa to MPa, as reported in literature [117-120].

In this Thesis, both PA and PDMS applications will be discussed.

2 MULTIMODAL IMAGING

Mechanical properties of cells and tissues, and strategies for mimicking mechanical environment cues linked to healthy and pathological conditions have been discussed in the first Chapter. However, adequate imaging tools and mechanical probing devices to observe cell responses and adaptations to mimicked mechanical features, such as changes in cell morphology and cytoskeletal rearrangement, as well as to measure cell mechanical properties, are needed. Therefore, Chapter 2 is dedicated to imaging techniques used. Some of the imaging modalities available for these kinds of studies are below described. Moreover, experimental application of these will be further proposed in the second part of the Thesis.

2.1. PHASE CONTRAST MICROSCOPY

Most biological cells are usually transparent; therefore, they optically differ only slightly from their surroundings. Human eye perceives changes in amplitude of a light wave, however cells adsorb little light, resulting in only minor changes in the amplitude of transmitted light. This is the reason why imaging living cells in noninvasive, label-free, real time and high-resolution way remained a technical challenge until contrast-enhancing techniques have been developed [121, 122].

Enhancing cell contrast was possible thanks to optical components and techniques which exploit cell's properties, such as thickness and refractive index, to create image contrast [122].

Phase contrast (PhC) firstly proposed by Zernike in 1930s followed by Nomarski's differential interference contrast (DIC) in 1952 allowed to transform the phase shifts induced by objects in detectable intensity modulation [123]. Nowadays these label-free and non-invasive contrast-generating techniques are widely used in cell science.

However, despite the advantages introduced, they only allow an increase of contrast without the possibility to quantitatively measure the phase shift. Therefore, quantitative variation of biophysical cell parameters including cell volume remains pretty challenging by solely PhC and DIC signal variations visualization [123].

To overcome this limitation Quantitative Phase Imaging (QPI) techniques have been developed enclosing Digital Holographic Microscopy (DHM) [124].

2.2. DIGITAL HOLOGRAPHIC MICROSCOPY

Holography is a particularly attractive interferometric imaging technique with QPI capability. Discovered by Denis Gabor in 1948 holographic techniques have been considerably developed since then [121, 123].

The first proposed version, known as "classical holography", was centered on its lens-less imaging capabilities. It consists of a two-step interferometric imaging enclosing a first recording followed by the reconstruction process. This allows to capture both the amplitude and phase information of an observed specimen (object wave) (Figure 2.1). In the first step, the interference pattern resulting from the interference of the object wave with the reference wave is analogically recorded on a photographic plate. Gabor called "hologram" this pattern referring to the Greak meaning of "holos" = "whole". Subsequently, the reconstruction is achieved by re-illuminating the hologram with the reference wave. The outcoming diffraction processes produces an exact replica of the original wave diffracted by the sample.

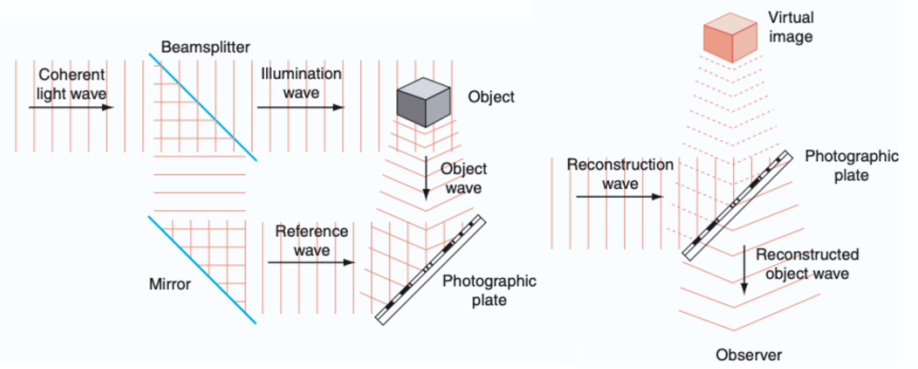

Figure 2.1. Layout of the two-step interferometric imaging consisting in a first hologram recording followed by the object wave reconstruction [121].

After ’90s the availability of cheaper digital detectors and charge-coupled device (CCD) camera lead to “digital holography” [123].

If the angle of incidence of the two waves (object and reference) is different, the real and the virtual images obtained by reconstruction can be separated spatially. This is called “off-axis” holography [125].

The use of an electronic camera allows to record digital holograms and fast achieve their numerical reconstruction. In fact, the reconstruction process obtained by re-illuminating the hologram in the classical approach is substituted by computer numerical reconstruction [121]. The application of digital holography (DH) to microscopy gave rise to the development of the digital holographic microscopy (DHM). Due to its interferometric and previously mentioned principle, DHM has been implemented using different classical interferometric configurations. However, the most used is based on a Mach-Zehnder interferometer; an exemplary layout is shown in Figure 2.2 [126].

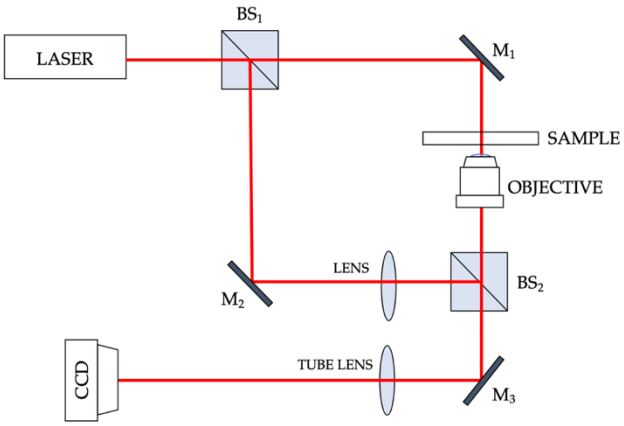

Figure 2.2. DHM typical layout showing main optical elements used for achieving the holograms recording on CCD camera. The laser beam is split by the first beam splitter (BS_1) in two beams which are reflected by mirrors M_1 and M_2. One beam crosses the sample passing through an objective and is then recombined with the reference beam. Thanks to the second beam splitter (BS_2) and the third mirror M_3, the beam is directed to the CCD camera where holograms are recorded.

DHM is nowadays successfully used in many fields, especially in the investigation of living cells [127-130].

This is due to its quantitative nature which allows some interesting morphological parameters measurement, such as cell thickness, volume, area, but also dynamical ones, for example cell membrane fluctuations. These are retrieved from the optical phase (OP) shift between the reference and object beam encoded in the acquired hologram and correlated to the optical path differences (OPD) following the relations:

$$OP = \frac{2\pi}{\lambda} OPD, OPD = h * (n_c - n_m), \quad (2.1)$$

where λ is the wavelength of the laser beam, h is the cell thickness, n_c is the refractive index of the cell, and n_m is that of the medium [123, 128, 130]. If the refractive indexes are known, the cell thickness can be easily obtained allowing subsequent calculation of other parameters such as cell volume. An example of acquired hologram and relative image reconstruction showing the cell thickness profile is provided within the Figure 2.3.

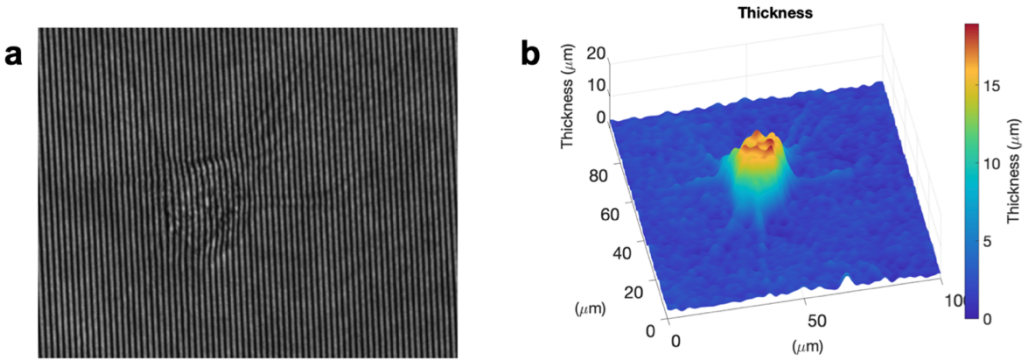

Figure 2.3. Hologram (a) and reconstructed image (b) of a cell.

In conclusion, the main advantage of DHM consists in providing quantitative information while remaining a label-free method.

2.3. FLUORESCENCE MICROSCOPY

Despite label-free methods, the introduction of labels such as fluorescent indicators had allowed a better cell physiology understanding due to the possibility to achieve full information on cellular internal structure and dynamicity.

The first fluorescence observation date back to 1845, however its explanation occurred only later, in 1852 by George Stokes. Therefore, at the beginning of 20th the first fluorescence microscopes were developed based on the expectation that an image can be better differentiated, and fine structure more easily detected, if the object itself emits light. Soon after, fluorescently-labeled antibodies were developed followed by genetic encoding of labeled proteins, which opened a new era on cells, organelles and proteins imaging [131].

The basic principle of fluorescence consists in the absorption of light energy by an indicator followed by the emission of some of this light energy a few nanoseconds later. During this process some of the energy is lost, therefore the emission occurs at a lower energy, thus at a higher wavelength [132].

Despite its usefulness in the biological field, the widefield (epifluorescence) microscopy remains a technique with diffracted-limited resolution to about 200 nm. However, novel developed fluorescence microscopy approaches have been introduced showing the ability to overcome some limitations. [133]. Among these there is confocal microscopy [134, 135]. It consists in the rejection of the out-of-

focus light from the image using two confocal pinholes. A pinhole aperture ensures that the light reaching the detector comes only from the equivalent (confocal) point in the specimen where the excitation light is focused [132, 136]. Confocal introduced just modest advantages in resolution but allowed the generation of high-contrast images through optical sectioning [134].

However, further advances had been performed thanks to the development of super-resolution methods in order to definitely overcome resolutions limitation.

The diffraction barrier of light microscopy had been broken for the first time with the invention of Stimulated Emission Depletion (STED) microscopy [137-140]. The originality of the invention resides in the ability to restrict the useful fluorescence emission to subdiffraction region at a given point of the sample by using stimulated emission depletion of the fluorophores surrounding it.

Beside STED, other super resolution techniques have been developed for the investigation of fluorescent samples with nanometric resolution enclosing Photo-Activated Localization Microscopy (PALM) [141], Stochastic Optical Reconstruction Microscopy (STORM) [142] and Structured Illumination Microscopy (SIM) [143].

Fluorescence microscopy is widely used to assess cellular features. It allows membrane, transmembrane and intracellular visualization of lipids, proteins or ions [132]. In the context of mechanobiology, in which cytoskeleton has a pivotal role, a lot of interest was gained by the possibility to observe cytoskeletal proteins organization, polymerization and dynamicity. This is achievable both on fixed samples and on living cells.

Fixed samples are generally selectively labeled through immunofluorescence technique [144]. On the other hand, the live cell labeling is generally possible by employing the available cell permeable fluorescent dyes, fluorescent proteins, and live-cell organic fluorescent probes [145].

In such ways, several targets of interest can be nowadays visualized thanks to the wide commercial distribution of antibodies, dyes and more generic fluorescent probes. In particular, in the second part of the Thesis the employment of a calcium binding dye will be shown for accessing calcium mobilization as a consequence of cell mechanical stimulation.

3 LOCAL PROBING TECHNIQUES

Despite imaging techniques which are used for assessing cell morphology and structures, the investigation of cellular mechanical properties requires the use of dedicated tools. As anticipated above, cellular events involved in mechanotransduction process occur at the nanoscale. In fact, as described in the previous Chapter, the efforts for reaching the nanometric resolution characterized the progress and the development of imaging techniques in the cell science field. In this context, nanotechnologies have not been limited to imaging tools, but also have supported the development of techniques for locally probing cellular mechanical features. This Chapter is dedicated to the description of some of these available methods which will be further proposed in the second part of the Thesis along with their experimental applications.

3.1. QUARTZ CRYSTAL MICROBALANCE

The following paragraph is taken and adapted from a research article published as first author: *Braidotti, N.; do R. B. F. Lima, M.A.; Zanetti, M.; Rubert, A.; Ciubotaru, C.; Lazzarino, M.; Sbaizero, O.; Cojoc, D. The Role of Cytoskeleton Revealed by Quartz Crystal Microbalance and Digital Holographic Microscopy. Int. J. Mol. Sci. 2022, 23, 4108.*

Among the available tools for mechanical cells probing and investigation, Quartz Crystal Microbalance (QCM) had gained a lot of interest.

QCM is basically a biosensor in which the sensor consists of a thin AT-cut quartz disc on which two gold electrodes are evaporated. An alternating current is applied to the quartz and, due to piezoelectric properties, causes its oscillation, whose frequency is sensible to the amount of the adsorbed mass.

In the case of very thin and completely elastic films, the frequency shift is proportional to the mass in contact with the quartz per unit of electrode's area. The equation that rules this relationship is known as Sauerbray's equation [146], which is

$$\Delta f_1 = -\frac{1}{C}\Delta m, \tag{3.1}$$

where C is the quartz sensitivity, f is the frequency, and m is the mass per unit of electrode surface area.

However, for such films immersed in liquid, an additional frequency shift is recorded due to liquid properties (density and viscosity). This term is called Kanazawa's contribute [147], and it correlates viscous properties with frequency shifts as follows:

$$\Delta f_2 = -f_0^{\frac{3}{2}}\sqrt{\frac{\rho_l \eta_l}{\pi \mu_q \rho_q}}, \tag{3.2}$$

where f_0 is the unloaded resonance frequency; μ_q and ρ_q are, respectively, the shear modulus and density of the quartz crystal; ρ_l and η_l are the density and viscosity of the liquid. In this way, the recorded total frequency shift consists of the sum of the contributions due to the mass and those due to liquid properties [148].

$$\Delta f = \Delta f_1 + \Delta f_2 = -\frac{1}{C}\Delta m - f_0^{\frac{3}{2}}\sqrt{\frac{\rho_l \eta_l}{\pi \mu_q \rho_q}}. \tag{3.3}$$

Unfortunately, this equation does not well predict the case of soft films immersed in liquid [148, 149]. Moreover, additional complications emerge when the film is not continuous, homogeneous, or even morphologically stable over time, making this technique unable to provide quantitative measurements when working with cells [150-153]. Thus, we used Equation (3.3) to achieve qualitative interpretations of our cell layer behavior. Additionally, in the case of liquid loading or viscoelastic films, a reasonable amount of dissipation of the quartz vibrational energy is observed [154, 155]. This dissipation (D) is proportional to the energy lost (G″) and stored (G′) during one cycle of oscillation, and it follows the equation:

$$\Delta D = \frac{G''}{G' 2\pi}. \tag{3.4}$$

Finally, with these two parameters (Δf and ΔD), provided by QCM, it is possible to investigate what occurs close to the surface of the quartz at the cell–substrate interface, considering that the penetration depth of the acoustic wave is given by:

$$\delta = \sqrt{\frac{\eta}{\pi f \rho}}, \tag{3.5}$$

where η and ρ are, respectively, the viscosity and density of the liquid, and f is the frequency [147, 154].

Therefore, by monitoring the above described outcoming parameters, QCM allows the detection of minute changes at the near-interface layer with its quartz sensor surface. For this reason, it has been employed to study cell–substrate adhesion [156-158], viscoelastic properties of the extracellular matrix [151], cytoskeletal rearrangements, and cell viscoelastic and morphological changes [152, 153, 159]. However, the absence of suitable models to predict the behavior of film layers made by cells limits the achievement of quantitative values, allowing only qualitative interpretations of the results. Therefore, the tentative of gaining quantitative mass or viscous information by using QCM is still challenging when working with cells [150-153]; however, if a complementary quantitative technique is used, the synergic outcomes could be very significant.

An example of successful combination of QCM with a quantitative method is presented in the second part of the Thesis in Chapter 4 with a case study concerning cytoskeletal rearrangement and adhesive properties of primary cardiac fibroblasts. As it will be shown, DHM was used as a quantitative tool for confirming the qualitative QCM interpretations with quantitative analysis.

3.2. MICROPIPETTE ASPIRATION

Micropipette-based technique has been widely used for assessing several cell mechanical and viscoelastic properties such as elastic modulus, membrane tension and viscosity [160-162].

A general aspiration setup consists of a micromanipulator which controls the positioning of the glass micropipette and a pressure generator [163].

The aspiration pressure (Δp) can be generated solely by connecting the micropipette to a liquid reservoir and can be regulated by adjusting the height of it following the relation:

$$\Delta p = \rho g \Delta h, \tag{3.6}$$

where ρ is the liquid density, g is gravitational acceleration and Δh is the height difference between the tip of the micropipette and the top of the reservoir [160, 161]. When the top of reservoir is higher respect to the tip a positive pressure following 3.6 rather than a negative one is generated [164].

The experimental setup described above works thank to solely hydrostatic pressure; however, it can join the addition of a pump for a better pressure control which provides an additional negative

pressure P_i. Therefore, the resulting aspiration pressure (ΔP) at the tip of pipette, considering the top of reservoir placed above the sample (thus generating a positive pressure), is [164]:

$$\Delta P = P_i - \rho g \Delta h, \tag{3.7}$$

The device described above has been successfully employed as a label free tool for the mechanical characterization of suspended cell by coupling the aspiration setup to the microscope [162, 165-168], as illustrated in Figure 3.1.

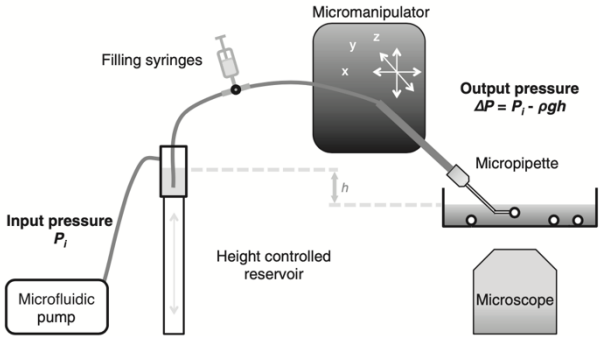

Figure 3.1. Layout of a typical micropipette aspiration setup coupled to optical microscope [164].

Moreover, in agreement with experimental purposes, several micropipette-based nanotools have been developed. An extensive review work was done by Haoqing Wang and collaborators [161] listing all the possible assays performed in single micropipette and dual micropipette mode.

However, the increased interest into mechanotransduction processes opened to the micropipette a new investigative field of application leading to multimodal micropipette assays [161].

In fact, micropipette with concurrent fluorescent imaging allows the investigation of mechanosensitive signaling [169]. Based on pressure force applied to deformable suspended cells (e.g. red blood cells), it is possible to achieve information of ion channel activity. A case study relative to this application is reported in the second part of the Thesis in Chapter 6.

On the same time, also adherent cells can be probe in this way for example by directly membrane aspiration or by pulling tether from the surface. This latter can be achieved thanks to silica beads attached on the membrane which are aspirated trough the micropipette system.

Instead of pulling the membrane, which is the core of the aspiration, the channel activation can also be studied by pushing the micropipette on the cells. In this case, the aspiration setup is not used except from the micropipette and the micromanipulator for pipette holding and positioning. If the micromanipulator is well equipped with a fine piezo controller, forces in the range of hundreds of nanonewton can be achieved, otherwise the range reached is no lower than tens of micronewton.

For lower pushing or pulling forces, Atomic Force Microscopy and Optical Tweezers can be used.

3.3. ATOMIC FORCE MICROSCOPY

Atomic Force Microscopy (AFM) was first proposed by G. Binning and C. F. Quate in [170] as a new system in which the motion of a cantilever beam with an ultrasmall mass is measured. This tool had been designed for the investigation of interatomic forces between single atoms.

The tool described above falls into the scanning probe techniques [171] and exploit the deflection of a cantilevered spring to image and probe different kind of samples [172].

A schematic representation of the device showing the main elements is reported below in Figure 3.2.

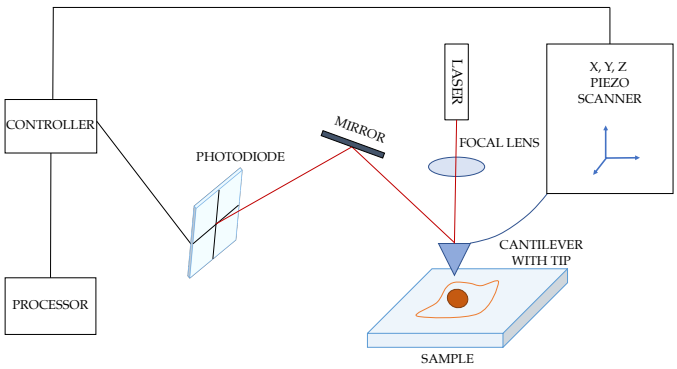

Figure 3.2. AFM components' schematic view

The tool sensing element is the flexible cantilever which is represented in Figure 3.2 equipped with a sharp tip, even if spherical probes are nowadays available and used. This is moved through a piezo scanner along the three dimensions. The deflection of the cantilever, as a consequence of interaction forces between the tip and the sample, is measured after the detection of the reflected laser beam with a photodiode [173].

This configuration confers to the AFM a versatile character. In fact, it can be used both as an imaging machine, allowing the acquisition of sample topography, and as a mechanical machine, by measuring various mechanical properties such as elasticity, adhesive and viscoelastic properties [172, 173].

The application of AFM as a mechanical machine, for the measurement of Young's Modulus of extracellular biocompatible substrates and cells, will be introduced further in this Thesis, along with its employment as local stimulation tool.

For this reason, technical information related to only this investigative modality are following reported.

When the cantilever is extended toward and retracted from the sample its deflection is determined as a function of the piezo-scanner deflection while the force sensed by the cantilever is calculated using the Hooke's law:

$$F = k \cdot d, \tag{3.8}$$

where k is the cantilever spring constant and d is the deflection. For cell studies cantilever stiffness used ranges between 0.01 and 0.6 N/m [174].

Since the vertical cantilever displacement and deflection are simultaneously recorded, a force-displacement curve is then obtained [173]. Subsequently, the contact point, which corresponds to the cantilever vertical position at which the contact with the sample occurs, needs to be established. Thereafter, the force-displacement curve can be converted into force-indentation one from which sample mechanical characterization can be achieved [174].

In fact, from such force curves samples' Young's Modulus is extracted by opportunely fitting the AFM experimental data. The widely used model is the Hertz one. This describes the simple case of elastic deformation of two perfectly homogeneous smooth bodies touching under load. However, it carries some assumption [175]:

1. The indenter must have a parabolic shape;
2. The indented sample is assumed to be thicker than the indentation depth (δ).

When the tip is approximated by a sphere of radius R, the force on cantilever $F(\delta)$ follows the equation:

$$F(\delta) = \frac{4}{3}\sqrt{R}\delta^{\frac{3}{2}}\frac{E}{1-\upsilon^2}, \tag{3.9}$$

where E and υ are the sample Young's Modulus and Poisson ratio respectively [175].

However, some Hertz model extensions, such as the Sneddon one, have been proposed for the consideration of other probe geometries respect to the sphere.

These models are based on the assumption of linear elastic behavior of the sample [174]. However, is well known that cells exhibit complex behaviors which place them pretty far from linear elastic materials [176]. Despite the discussion about the suitability of these models for biological specimens, the use of Hertz model is commonly accepted for comparative investigations [172], as will be presented further within this Thesis.

3.4. OPTICAL TWEEZERS

Optical Tweezers (OT) were introduce in the '70s by Arthur Ashkin who demonstrated the possibility to optically trap dielectric spheres by using lasers and exploiting the radiation pressure of light.

The unique characteristic of the technique is the possibility to hold a single particle in space, without mechanical contact, by using just a single beam of light, tightly focused [177]. For macroscopic objects the radiation pressure is too small and fail in achieve optical trapping and manipulation which is verified, instead, for microscopic objects (<100 μm). This happens thanks to the transfer of photons momentum to the object owning a refractive index different from the surrounding medium.

The forces governing such phenomenon can be divided in two components:

1) the scattering force that pushes the object away from the light source;

2) the gradient force that pulls the object towards the region of highest light intensity.

Depending on the size (d) of objects respect to the light wavelength (λ), the optical trapping is classified in:

1) "Rayleigh" regime for $d<<\lambda$;

2) "Ray-optics" or "Mie" regime for $d>>\lambda$.

However most biological applications find place in the middle of the two regimes, therefore both descriptions fail in quantitative accuracy [178-180].

In the first regime ($d<<\lambda$) the particle can be modeled as an induced dipole by the electric field of light. When the field is not homogeneous (as the Gaussian laser beam) the particle experiences an attractive force, which pushes it towards the higher intensities of the beam. However, particles are also subjected to scattering forces which arise from the absorption and reflection/refraction of the light and push them in the direction of the incident light. Representation of these forces is shown in the Figure 3.3.

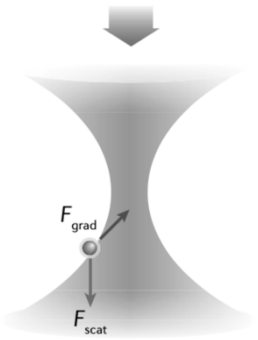

Figure 3.3. Representation of forces experienced by a Rayleigh particle. The particle, acting as an induced dipole, experiences gradient force which attracts the bead toward the higher intensity of the beam and scattering force which pushes it in the direction of the incident light (indicated by the big arrow on the top) [181].

In order to achieve successful trapping, the scattering force needs to be balanced by the gradient one. This is achieved through tight focusing obtained by large numerical aperture objectives [179, 181, 182].

On the contrary, in the Mie regime ($d>>\lambda$), the particle acts as a refractive object. Therefore, the momentum of the light changes, but as a consequence of the conservation of linear momentum, this is accompanied by a net force of opposite sign acting on the object [181]. A schematic representation of forces acting on Mie particles is shown in Figure 3.4.

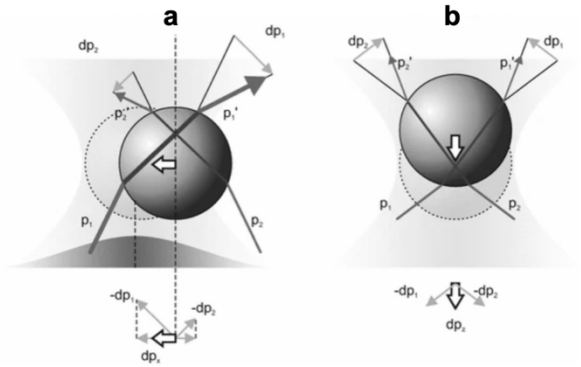

Figure 3.4. Representation of forces experienced by a Mie particle consist in lateral (a) and axial (b) gradient forces [179].

By considering the Figure 3.4a, p_1 and p_2 are rays of different intensity and are subjected to a momentum change which differs in magnitude (Δp_1 and Δp_2). This causes a net reaction force on the refracting medium in the direction of the highest intensity. Therefore, the x-projection of this force pulls the particle toward the center of the beam. Similarly, also the axial gradient force (Figure 3.4b) is caused by the momentum transfer upon refraction which results in a restoring force towards the focus.

A basic OT setup (Figure 3.5) consists of a laser beam which is expanded by a telescope and passed into a high numerical aperture objective lens that focuses it into a diffraction-limited spot, namely optical trap, inside the sample chamber. Therefore, a condenser lens collects the transmitted light which is imaged into a Quadrant Photodetecor (QPD) to measure the displacement of the trapped particle and hence the force exerted on it ($F= kx$).

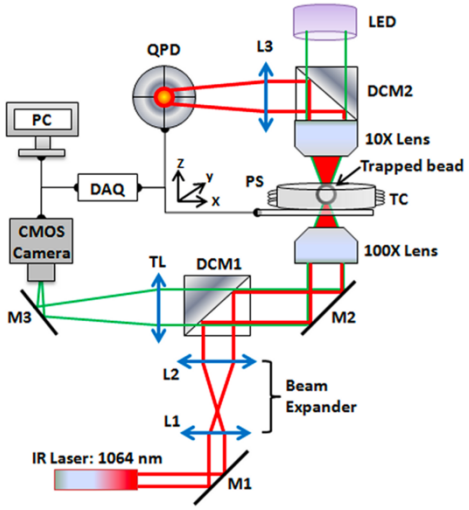

Figure 3.5. Optical Tweezers' setup layout. Laser trapping (1064 nm) beam path (red) and bright-field imaging path (green). PS: 3-axis nano-piezo stage; DAQ: digital analog acquisition card; TL: tube lens; L1–L3 convergent lenses; M1–M3: mirrors; DCM 1–2 dichroic mirrors, TC: temperature controlled holder [183].

Since the attractive force is directly proportional to the displacement of the particle following the Hooke's law, the spring constant k represents the stiffness of the optical trap with values in the ranges 100 - 1 pN/μm [179].

Despite AFM, which force ranges from hundreds of pN to μN [171], the forces measured by OT are in the range 0.1-100 pN [184]. This is due to the spring constant which characterizes each technique. In fact, for a hypothetic displacement (x) of 1 μm with 1 pN force, 10 pN/μm spring constant (k) is needed and provided by OT. On the contrary for 500 nN force, k should be about 0.5 N/m which is the typical spring constant of AFM cantilevers.

Both techniques had been used in this project and their application to cell studies will be further presented.

GOAL OF THE THESIS

The Thesis is focalized on morphological and mechanical properties of cells which had been investigated by multimodal imaging and mechanical probing techniques. The tools discussed above have been used to investigate both eukaryotic and prokaryotic cells from the micro- and down to the pico-level.

In the following Chapters results and discussions about four main investigative approaches will be introduced.

A consistent work has been done on cardiac fibroblasts. Cytoskeletal elements' role in the regulation of mechanical, morphological and adhesive properties had been investigated by exploiting the synergy between two distinct tools owning distinct strengths. Together the advantages of the techniques allowed the achievement of interesting and novel results highlighting the powerfulness of multimodal approaches. Thereafter, cardiac fibroblasts mechanosensitivity had been studied. The leading biological question aimed to unveil hidden mechanosensitive mechanisms which are suggested to be implicated in cardiac fibrotic disease. Even in this work a multimodal approach allowed to obtain relevant and complementary results.

The attention will be moved, then, on red blood cells and the validation of a novel approach combining MA and multimodal imaging as a tool able to retrieve a multiplexity of information with several advantages.

In the final part, I will introduce an extensive work performed on bacteria where an imaging-based method had been validated as a clinical alternative for fast urine samples screening.

In the conclusive part, I will summarize the strengths of multimodal investigations. The use of both complementary techniques and multiple accessible information within the same multimodal-operating device, which characterize the thematic areas covered by the Thesis, will be evidenced as successful workflow when working with living cells.

To sum up, the Thesis represents a journey across several nanotechnology techniques employed in biophysical applications, with important suggestions about possible multimodal combination and related advantages, and proposes the relevant results achieved so far.

Part II

RESULTS AND DISCUSSIONS

4 THE ROLE OF CYTOSKELETON REVEALED BY QUARTZ CRYSTAL MICROBALANCEAND DIGITAL HOLOGRAPHIC MICROSCOPY

In this Chapter, a published research article with me as first author is proposed (*Braidotti, N.; do R. B. F. Lima, M.A.; Zanetti, M.; Rubert, A.; Ciubotaru, C.; Lazzarino, M.; Sbaizero, O.; Cojoc, D. The Role of Cytoskeleton Revealed by Quartz Crystal Microbalance and Digital Holographic Microscopy. Int. J. Mol. Sci. 2022, 23, 4108*). In this work a useful combination of DHM and QCM is exploited. Even if the two techniques lead to obtain independent results, the novel multimodal approach proposed allowed to retrieve synergic and significant results about cardiac fibroblasts morphological, dynamical and mechanical properties, with a particular focus on cell-interface interaction which falls in a nanometric region of interest.

In particular, we investigated and presented results on rheological, adhesive, and morphological properties of primary rat cardiac fibroblasts, the cytoskeleton of which was altered by treatment with cytochalasin D (Cyt-D) and nocodazole (Noc), respectively. Qualitative data on cell viscoelasticity and adhesion changes at the cell-substrate near-interface layer were obtained with QCM, while DHM allowed the measurement of morphological changes due to the cytoskeletal alterations. A rapid effect of Cyt-D was observed, leading to a reduction in cell viscosity, loss of adhesion, and cell rounding, often followed by detachment from the surface. Noc treatment, instead, induced slower but continuous variations in the rheological behavior for four hours of treatment. The higher vibrational energy dissipation reflected the cell's ability to maintain a stable attachment to the substrate, while a cytoskeletal rearrangement occurs. In fact, along with the complete disaggregation of microtubules at prolonged drug exposure, a compensatory effect of actin polymerization emerged, with increased stress fibers formation.

4.1. INTRODUCTION AND AIM

As previously mentioned at the very beginning of this Thesis, the cytoskeleton is a vital cellular component which is involved in conferring rigidity to the cells but also in cell mechanotransduction and adhesion processes [35-37, 41]. It's dysfunctions had been linked to several functional impairments and diseases [30]. In particular, it was shown that some of its alterations can be related to some cardiomyopathies [33, 34, 37]. However, since the adhesions plays an important role as mechanosensitive elements involved in substrate properties signaling [43], both in normal tissue development and pathological conditions, cell cytoskeletal alteration can be reflected in impaired cell response at the substrate interface [3], with subsequent dysfunctional outcomes.

Therefore, this justifies the efforts for a deeper investigation of the cell-substrate interface, both in physiological and altered cell conditions.

Many studies investigated mechanical, viscoelastic, and morphological changes in cells as a result of the effects of some drugs, able to alter cytoskeletal components: microfilaments, intermediate filaments, and microtubules [150, 185-188]. Actin is known to be the main cytoskeletal element responsible for preserving mechanical and morphological properties in healthy cells [27, 35, 188, 189]. It is thus involved in the cytoskeletal reorganization that occurs as a consequence of mechanical signaling or mechanotransduction, which is a process often altered under pathological conditions [37, 186]. Microtubules and intermediate filaments seem to have secondary importance but, even if their alteration is not correlated with evident effects at first glance, they are required for the cell mechanical equilibrium [190, 191]. For the purpose of cell mechanics investigation, many tools are nowadays

employed such as optical tweezers [185], atomic force microscopy [35], and cell stretchers [188]. Among these, there is an emerging interest in the use of QCM.

Since QCM allows the detection of minute changes at the near-interface layer with its quartz sensor surface, as anticipated before, it has been successfully employed to study several cellular properties with particular attention to the cell-substrate interface [156-158]. However, the technique is limited to qualitative interpretation due to the absence of suitable models for cell layers requiring the use of quantitative tool in support of it. Among the quantitative tools, DHM is a free-label quantitative phase microscopy technique, able to retrieve the height of transparent samples, such as living cells [121, 126, 127, 129, 130, 192, 193]. Thus, quantitative morphological parameters (cell area, volume, and thickness) can be easily obtained, as well as dynamical measurements such as cell membrane fluctuation (CMF) [130, 192].

In this study, QCM was employed for recording changes in frequency (Δf) and dissipation (ΔD) values for cells under the action of two cytoskeletal drugs. The near-interface investigation of cellular rheological variations was performed by studying the effect of Cyt-D and Noc, which inhibit actin [189, 194] and microtubule polymerization, respectively [195, 196]. Afterward, we exploited the advantages of the DHM technique to gain morphological quantitative information on cell area, volume, and thickness.

In this way, the rheological, morphological, and adhesive properties variations due to cytoskeletal alterations were studied by confirming the qualitative interpretations (QCM) with quantitative analysis (DHM).

4.2. MATERIALS AND METHODS

4.2.1. Cell Culture

Post-natal day 4/5 neonatal Wistar rats were euthanized by decapitation. To isolate cardiac fibroblasts, the hearts were extracted from the abdominal cavity and placed in CBFHH (calcium and bicarbonate-free Hank's Buffer with HEPES) supplemented with 10 U/mL heparin (H3149, Sigma-Aldrich, St. Louis, MO, USA) and stored on ice. After extraction, fibroblasts were cultured at 37 °C in a 95% H_2O and 5% CO_2 atmosphere in Dulbecco's modified Eagle's medium (DMEM), high glucose, GlutaMAX™, pyruvate (Thermo Fisher Scientific, Waltham, MA, USA), and supplemented with 10% fetal bovine serum (FBS) (Sigma-Aldrich, St. Louis, MO, USA) and 1% antibiotic–antimycotic (Thermo Fisher Scientific, Waltham, Ma, USA). Fibroblasts were used at P0/1 either from fresh cultures, or liquid-nitrogen-stored after previous extractions.

For QCM measurements, cells at a density of 20,000 cells/cm^2 were drop-seeded on the surface of the sterilized Au-coated quartz sensor. Afterward, cells were allowed to attach to the incubator for 24 h.

For DHM experiments, 24 h before measurements cells were seeded into 35 mm Petri dishes at a density of 2600 cells/cm^2, in order to obtain enough isolated cells.

4.2.2. Drug Solutions

Cytochalasin D (Cyt-D) (C8273, Sigma-Aldrich, St. Louis, MO, USA) and nocodazole (Noc) (M1404, Sigma-Aldrich, St. Louis, MO, USA) were used to depolymerize actin and microtubules, respectively. Stock solutions were made by dissolving the drugs in DMSO (Sigma-Aldrich, St. Louis, MO, USA) at 4 mg/mL (Cyt-D) and 3.88 mg/mL (Noc). On the day of treatment, the stock solutions were diluted directly inside the medium to a final working concentration of 5 μM (Cyt-D) and 10 μM (Noc), with less than 0.1% of DMSO content. Since the tests were performed in air, 25 mM of HEPES (Thermo Fisher Scientific, Waltham, MA, USA) was used to keep the proper pH balance.

4.2.3. Quartz Crystal Microbalance (QCM)

The basic principles of QCM, as well as mathematical formulas, had been previously reported (see Chapter 3, Section 3.1).

The QCM device used for the experiments in this study was built by Novaetech Srl (openqcm.com), Pompei (NA, Italy). All of the measurements were performed with an AT-cut quartz crystal sensor with a 10 MHz resonant frequency and 11.5 mm diameter gold electrode, placed in the QCM's chamber of 30 µL in volume. The quartzes used were characterized by a sensitivity (C), shear modulus (μ_q), and density (ρ_q) of, respectively, C = 4.42 ng/Hz·cm^2, μ_q= 2.947 × 10^{11} g/cm·s^2, and ρ_q= 2.648 g/cm^3. The experiments were performed at 37 °C in an oven (M 40–TB, Tecnovetro Srl, Monza, Italy); thus, we could approximate the QCM acoustic shear wave decaying into the liquid to δ = 180 nm, which corresponds to that of a 10 MHz AT-cut quartz crystal under water loading at 37 °C [153].

The quartz, with attached cells, was positioned in sterile conditions in the chamber, which was closed and subsequently filled with medium using a tubing system connected to a peristaltic pump (Masterflex C/L^{TM}, Cole Parmer, Vernon Hills, IL, USA). Each experiment began with a first calibration phase with medium-only until steady state, when an equilibrium in the temperature profile was observed.

Afterward, the drug-containing medium was fluxed inside the chamber. Once all of the liquid was replaced, the flux was stopped, and the frequency (f) and the dissipation (D) values were continually monitored for the subsequent four hours at intervals of 0.66 s.

4.2.4. Digital Holographic Microscopy (DHM)

Once obtained the holograms, in which the information about the OP is contained (see Chapter 2, section 2.2), the cell projected surface area (*PSA*), volume (*V*) [130], and cell membrane fluctuation (*CMF*) [192] had been calculated as follows:

$$\mathrm{PSA} = N * p_a, \tag{4.1}$$

$$V = p_a * \sum_{i=1}^{N} h_i, \tag{4.2}$$

$$CMF = \frac{1}{N}\sum_{i=1}^{N} STD_i, \tag{4.3}$$

where N is the number of pixels within the projected surface area, p_a is the area of a single pixel of the CMOS sensor in the object plane, and STD_i is the phase standard deviation for each pixel.

In this study, DHM in off-axis configuration, based on a Mach–Zehnder interferometer, was used [121, 130, 192]. The laser beam (λ = 630 nm, 05-LHP-151, Melles Griot, Bensheim, Germany) was split into object and reference beams and recombined by a cube beam splitter (BS079, Thorlabs Inc., Newton, NJ, USA) to generate the hologram, which was recorded on an sCMOS camera (CS2100M-USB Quantalux, Thorlabs Inc., Newton, NJ, USA). The samples were exposed to a power (P) of the laser set to P≈0.2 mW and the exposure time (t) was 0.5 < t < 1 ms. The magnification of the microscope was set at 33.2X, with a lateral spatial resolution d≈600 nm. An aspheric lens (C230TMD-A, Thorlabs Inc., Newton, NJ, USA) with the numerical aperture NA = 0.55 was used as the objective lens. The size of the sCMOS sensor was 1920 × 1080 pixels (4.8 × 4.8 µm per pixel).

The digital procedure applied to holograms, in order to achieve the reconstruction of the optical phase, was previously reported by our group [126, 130]. DHM was employed for monitoring area and volume variation by achieving information from the reconstruction of a single full-frame (1920 × 1080 pixels) image. Cells were segmented, in order to separate them from the background, by manual segmentation of the reconstructed optical phase image, using Image Segmenter, a MATLAB built-in environment. Cell height, area, and volume were calculated, as already explained in [130], considering the refractive index of cell and medium, respectively, as n_c = 1.37 and n_m = 1.35 [197, 198]. Moreover, *CMF* were achieved by using a customized algorithm based on the approach

developed by Rappaz et al. [192], which was applied on at least 2 s of a movie recorded with a window of 480 × 290 pixels and a frame rate of 110 frames per second (FPS).

Two types of experiments were performed: multicell and single-cell analyses. In multicell experiments, for each drug treatment, five groups of cells were tested considering the effective range of the drug's action on cells. For Cyt-D, we analyzed untreated cells and cells after 10, 20, 40, and 60 min of Cyt-D 5 μM treatment. For 10 μM Noc treatment, we considered the following intervals: 0, 1, 2, 3, and 4 h. For each group, we obtained an overall measurement of more than 30 cells for which area, volume, and *CMF* were calculated, as previously explained. Instead, for the second type of experiment, we monitored single cells' area and volume variations with time-lapse performed at 2 FPS for 15 min, starting immediately after the Cyt-D injection. Before the measurements, each sample was washed with PBS 1X and subjected to medium substitution with a fresh one, for both untreated and time-lapse samples, or to drug solution, for treated cells.

4.2.5. Fluorescence Microscopy

Epifluorescence imaging was performed to observe the cytoskeletal rearrangements. Cells were seeded on round glass coverslips (18 mm diameter) for 24 h before being treated with the desired drug's solution. For both treatments, one glass was left untreated and used as a negative control. Treated samples were fixed (paraformaldehyde 4%, 20 min) after 10 and 30 min of incubation in Cyt-D or after 30 min and 2 h of incubation in Noc.

After being permeabilized with Triton X-100 0.1% and blocked with bovine serum albumin (BSA) 0.5% for 5 and 30 min, respectively, fixed cells were incubated with the following antibodies or staining solutions: primary antibody to α-tubulin (ab7291, Abcam, Cambridge, England, 1:500), secondary antibody conjugated to Alexa 488 (ab150113, Abcam, Cambridge, England, 1:500), TRITC-conjugated phalloidin (90228, Millipore, Burlington, MA, USA, , 1:250) and DAPI (90229, Millipore, Burlington, MA, USA , 1:1000).

Fluorescent observations were performed using an inverted Axiovert 200M microscope (Carl Zeiss AG, Oberkochen, Germany) upgraded with the appropriate excitation–emission filters for TRITC, FITC, and DAPI spectra, and coupled with a 63X/1.4 Plan Apo oil immersion objective (Carl Zeiss AG, Oberkochen, Germany) as well as an X-cite® 120Q fluorescence illuminator (Excelitas Technologies Corp., Waltham, MA, USA). Images were taken with an XM10 monochrome CCD camera (Olympus Corporation, Tokyo, Japan), connected to a 0.63X adaptor tube, at an exposure of 5 s (FITC and TRITC) or 1 s (DAPI) and by averaging 5 frames for noise reduction. Subsequent image processing was performed using the open source Fiji image processing package (https://imagej.net/software/fiji/, accessed on 1 April 2022).

4.3. RESULTS AND DISCUSSION

QCM experiments were performed by using equipment and operation protocols as explained in Section 4.2. In order to ensure that cell signals (Δf and ΔD) were not hidden by other factors (e.g., viscous properties of the medium and the toxic effect of DMSO on cells), we also performed control experiments (see Section 4.3.1.3). Subsequently, for confirming the rate of drug action on the cell's cytoskeleton, we performed actin and tubulin staining. Finally, DHM allowed us to confirm our qualitative deductions by gaining information on quantitative area and volume variations during the treatment.

4.3.1. QCM Results

QCM experiments were performed with different sets of cells under the same seeding and growth conditions. Cell seeding density on the quartz surface and procedures employed are reported in Section 4.2. After the achievement of steady state, the introduction of the drug solution was carried

out and the signals were monitored for four hours. Based on values provided by QCM (Δf and ΔD), the two drugs showed evident differences in rheological response. Control experiments (Section 4.3.1.3) were performed either with a DMSO-containing medium, in equal volume as that used in the relative drug solution, or separately with the drug solution in the absence of cells. The low content of DMSO on cells did not show any detectable toxic effect, and the only change in liquid properties from the medium to the drug-containing medium was found to be negligible. These lines of evidence guaranteed the possibility of gaining interpretations of the behavior of cells as a direct consequence of the cytoskeletal alterations due to Cyt-D and Noc.

4.3.1.1 Frequency Shifts (Δf)

The comparison of frequency shift (Δf) signals obtained for Cyt-D- and Noc-treated cells is reported in Figure 4.1.

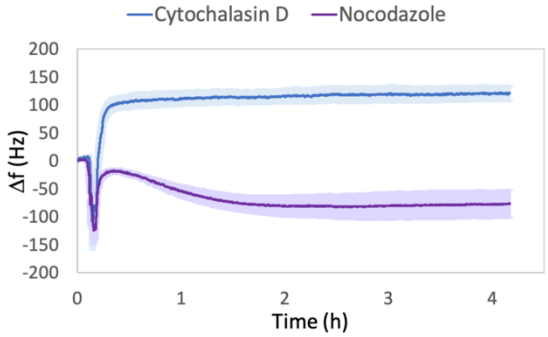

Figure 4.1. Comparison between frequency shifts (Δf) of Cyt-D- and Noc-treated cells. The mean values are relative to three independent replicas performed with different sets of cells. The reported Δf values are relative to f signals recorded from 10 min before the drug solution injection (Cyt-D 5 µM or Noc 10 µM) until the end of four hours of treatment.

In both curves, we observed initially a fast decrease, due to the activation of the flux for the liquid chamber substitution. After this common feature, the two drug treatments led to independent and different behaviors. Using Cyt-D, the frequency increased and reached the maximum value within a few minutes, comparable with the range of activities on actin [194, 199]; then, it was maintained almost constantly in a steady-state-like condition until the end of the experiment. Conversely, using Noc, we observed an initial increase, followed by a gradual decrease for the subsequent two hours. These trends suggest that the rapid loss of cell viscosity due to Cyt-D, observed by other techniques [200-203], can be also sensed by the quartz sensor. In fact, since the operating condition is outside the limits of Sauerbray's Equation (3.1), a positive shift cannot only be assigned to the loss of mass, and Kanazawa's Equation (3.2) should also be considered. Moreover, it is known that Cyt-D treatment induces cells to lose the cytoskeleton–integrin–ECM links; thus, some focal adhesions could disappear, and consequently the body of the cell results retracted. This was also observed in human fibrosarcoma [185], NIH3T3, human dermal fibroblasts [159], murine fibroblast-like L929, and the kidney [200, 204] cell lines. This suggests that the area in contact with the quartz is highly reduced during the treatment, and even desorption of some cells can occur.

However, this observation does not agree with the considerations of Tymchenko et al. [159], who claimed that Cyt-D exposure leads to cell body retraction but does not involve changes in the surface area. In order to support our deductions about the decreased area in contact with the quartz surface, we carried out quantitative measurements with DHM (Section 4.3.3) and observed that this body retraction (cell rounding up) was indeed coupled with a decrease in the projected cell area and an increase in height. Since with our quartz sensor measurement, the penetration depth (δ) of the acoustic wave under water loading was about 180 nm, and assuming that cells have similar properties to those

of water, the rounding up action led cells to collocate a major part of their body out of the quartz sensitivity limit. Therefore, the measurement of the cell mass in contact with the quartz decreased and influenced the shift in frequency, as Sauerbray's equation suggests.

On the other hand, the initial slight increase in Δf observed in Noc-treated cells could be attributed to the tentative to restore the thermalization value achieved immediately before the solution's injection. Since the effect of Noc needs more time, compared with that of Cyt-D, for a significant cytoskeletal modification [205, 206], the decrease in Δf for the subsequent two hours could reflect the progressive damage of microtubules with increased viscosity [196, 207] and subsequent cytoskeletal rearrangement. In fact, meanwhile, the compensatory effect of actin polymerization occurred, emerging from the slight increase in frequency rather than maintaining a firmly steady-state-like condition at prolonged drug exposure. This stimulated effect on actin is well accepted [208, 209] and is explained by Noc's ability to activate the downstream Rho-associated protein kinase (ROCK) pathway, leading to myosin activation and increased actin stress fiber expression, which we were able to confirm qualitatively through immunofluorescence (Section 4.3.2).

4.3.1.2. Dissipation Shifts (ΔD)

Similar to frequency signals, it is possible to observe a clear difference in viscoelastic cells behaviors also in the dissipation profiles (Figure 4.2).

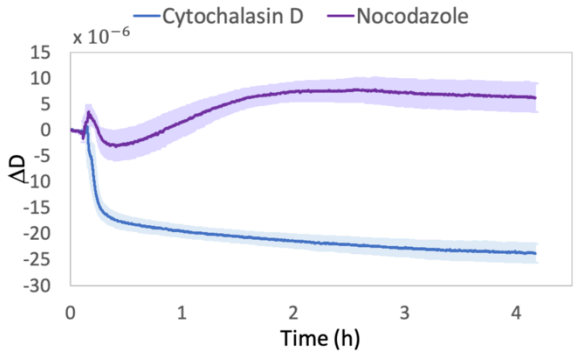

Figure 4.2. Comparison between dissipation shifts (ΔD) of Cyt-D- and Noc-treated cells. The mean values are relative to three independent replicas performed with different sets of cells. The reported ΔD values are relative to D signals recorded from 10 min before the drug solution injection (5 µM Cyt-D or 10 µM Noc) until the end of four hours of treatment.

In Cyt-D, we observed a fast decrease in dissipation, which mirrors the rate of increase in Δf profile. This negative shift can be attributed to the change in cell-substrate adhesion with a transition to a more round-like shape [152, 159, 199] as a consequence of the Cyt-D effect. In addition, since D corresponds to the ratio between the energy dissipated during the oscillation (G″) and the energy stored (G′) (3.4), the displacement toward a lower value of D is assumed to be caused by a transition to a more liquid-like cells state [150]. In fact, it was largely demonstrated that, under Cyt-D treatment, both storage and loss moduli decrease [201, 210, 211]. However, our results show that G″ decreased faster than G′. Since cells are usually characterized by G′ > G″ [201, 210, 211], at first glance, we found it contradictory. In fact, the increased difference between the two moduli upon treatment suggests a predominant elastic outcoming [212]. Nevertheless, some studies have stated that, since Cyt-D acts on actin filaments, elastic properties of cells, such as Young's Modulus, are reduced upon treatment [201, 213, 214]. At the same time, it was also shown that the ECM behaves elastically in the absence of significant energy dissipation [151]. Therefore, since the mass in contact with the quartz was reduced upon treatment, it is reasonable to believe that the sensor surface is more sensitive to the larger presence of ECM rather than the presence of cells. In fact, even in the absence of surface precoating, which was not necessary for supporting fibroblast adhesion in our case and was

intentionally avoided in order to limit the risk of hiding cell signals, spontaneous adhesion of serum proteins and secretion of extracellular proteins by cells themselves may occur [157].

Conversely, in Noc, we observed a gradual increase in ΔD within the first two hours. This is probably due to the damage of microtubules, resulting in a more viscous behavior, with higher energy dissipation. In fact, during Noc treatment, the tubulin is redistributed through the cytosol [208], as we observed in immunofluorescence experiments (see Section 4.3.2), and, at this time, cells may be able to oppose more resistance to the quartz oscillation, reflecting an initial increase in the loss modulus (G″). Meanwhile, the actin's compensatory effect could emerge, becoming preponderant at prolonged drug exposure and resulting in a slight decrease in dissipation during the last two hours, accompanied by an increase in G′ [210].

Unlike the liquid-like behavior and cell detachment observed in Cyt-D-treated cells, under Noc treatment, we did not observe any rounding or loss of adhesion even if a shape reorganization occurred. Despite the Cyt-D effect, is well known that Noc causes a loss in cell polarity [215], accompanied by a redistribution of the surface projected area, which we quantitatively demonstrated with DHM (see Section 4.3.3). However, the increased loss in viscosity could be attributed to the ability to maintain a firm attachment to the substrate while the reorganization of the cytoskeleton occurs.

4.3.1.3. Control Experiments

Since the Δf and ΔD shifts caused by changes in viscous properties between medium and drug-containing medium could, in principle, hide cells' information, control experiments were performed without cells on the quartz, to exclude this hypothesis. Furthermore, even if cells were subjected to a final concentration of DMSO lower than the toxic limit (0.1%), in order to exclude its effect on the behavior of the cells, we performed additional control experiments. For this purpose, as the injecting solution, we used only a DMSO-containing medium by keeping the same volume as that of Cyt-D or Noc used for the drug solution, and then we compared the results.

As it can be seen from Figures 4.3 and 4.4, the frequency and dissipation shifts due to the liquid variation in the absence of cells (no-cell lines) are negligible, compared with those of cells on quartz. The frequency curves resulted in a fast decrease, due to the activation of the flux, which then gradually restored, approaching thermalization values. A similar trend was observed in the dissipation curves. In DMSO lines, we observed a progressive slight increase in frequency signals and a decrease in dissipation. Since post-experimental microscopic observations showed healthy cell morphology, we ascribed the two signals trend to a state of continuous cell spreading.

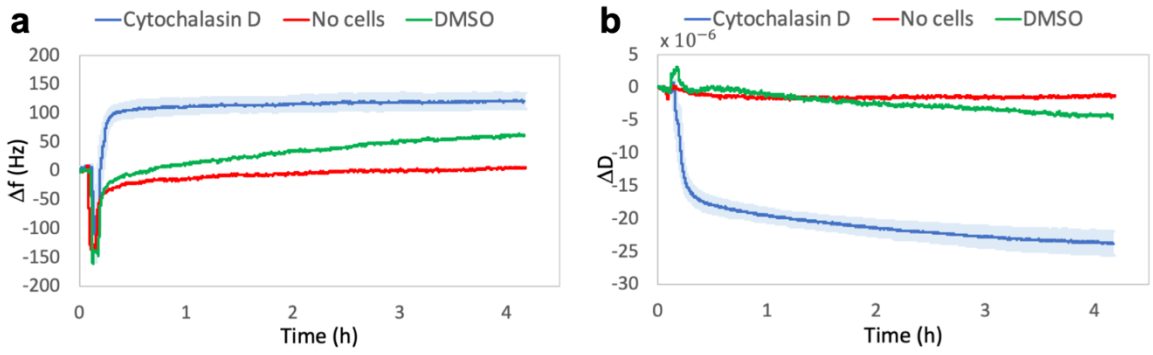

Figure 4.3. **Comparison between Δf (a) and ΔD (b) shifts in the experimental condition (Cytochalasin D) and in control condition: only drug solution in the absence of cells (No cells) or DMSO-containing medium in equal quantity as that one used for the drug solution (DMSO). The reported Δf and ΔD values are relative to f and D signals, recorded from 10 min before the solution injection until the end of four hours of treatment.**

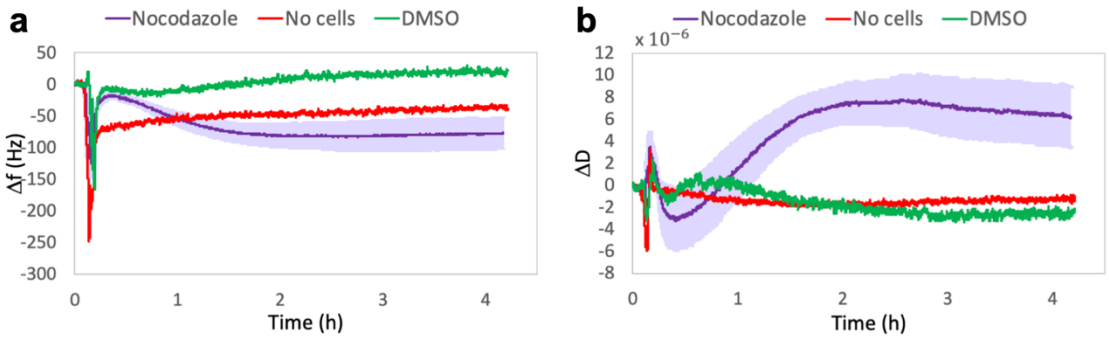

Figure 4.4. **Comparison between Δf (a) and ΔD (b) shifts in the experimental condition (Nocodazole) and in control condition: only drug solution in the absence of cells (No cells) or DMSO-containing medium in equal quantity as that one used for the drug solution (DMSO). The reported Δf and ΔD values are relative to f and D signals, recorded from 10 min before the solution injection until the end of four hours of treatment.**

In fact, several studies about healthy cells on quartz surfaces show that, under adhesion and subsequent spreading, positive frequency shifts are observed during the reorganization of the cytoskeleton and formation of focal adhesions [150, 152, 199]. Even if the spreading appears as the opposite of rounding up, we need to highlight again that the QCM's signals depend on the contributions of different factors, which are not separable. Thus, qualitative interpretations were made, but the weight of a single contribution to the whole formula could not be determined. With this in mind, a positive frequency shift could be attributed to a reorganization of the cytoskeleton and thus an increase in G′ [148, 199], while the higher sensed mass could be responsible for the delay resulting in a progressive trend instead of a sudden shift, as the one observed in Cyt-D treatment. On the other hand, the relative negative dissipation shift could also probably be attributed to a rise in the spreading and rigidity, which allow cells to better follow the quartz oscillation. This gradual energy dissipation decrease reached values higher than those observed in Cyt-D treatment and lower than those in Noc. This means that a healthy spread cell is more energy-dissipative than a cell with a disrupted actin network, in which the strong association between cytoskeleton, cellular membrane, and ECM is lost [216, 217] but remains less dissipative than a cell with disrupted microtubules, which is characterized by a higher viscous behavior.

These negligible effects enabled us to provide deductions on QCM signals by considering only changes in cell rheological behavior due to the effect of cytoskeletal drugs.

4.3.2. Immunofluorescence

Immunofluorescence experiments were performed in order to highlight the rate of drugs action on cytoskeletal elements. From the characteristic times observed in QCM signals and known from data provided in the literature, we decided to monitor the effect of Cyt-D at a shorter exposure time than that of Noc. For this purpose, we treated cells for 10 and 30 min with Cyt-D, and 30 min and 2 h with Noc.

Cyt-D showed the ability to achieve substantial F-actin depolymerization into G-actin monomers in a very short time (10 min), without any additional visible effect at prolonged drug exposure (Figure 4.5).

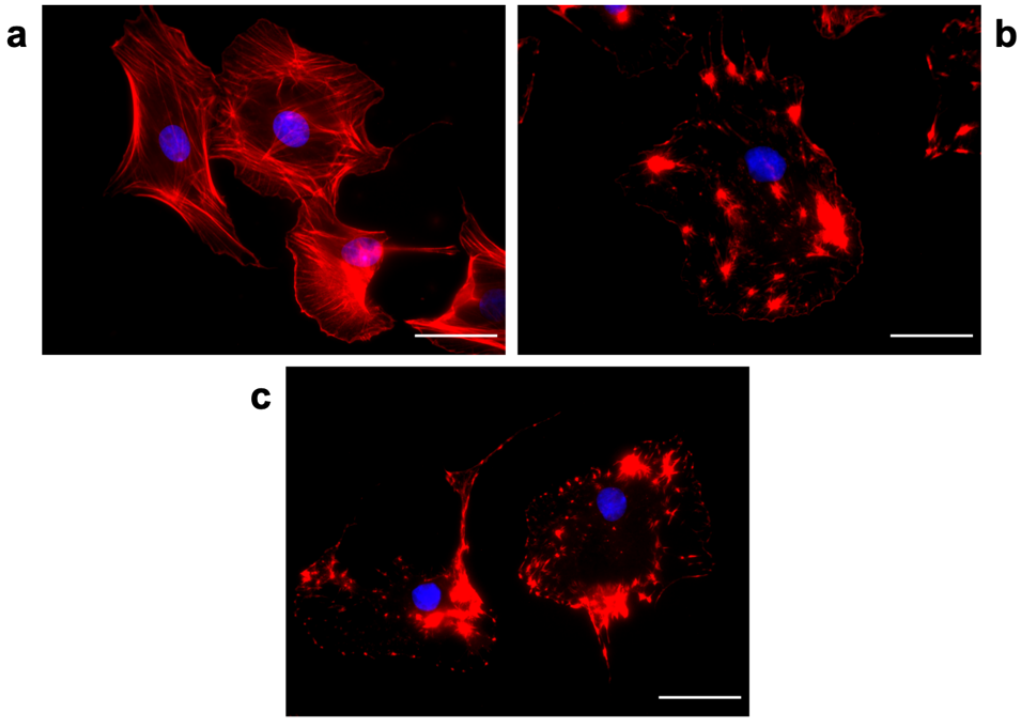

Figure 4.5. **Effect of Cyt-D 5 µM on cytoskeletal actin. Fluorescent images for control (a) and cells after 10 min (b) and 30 min (c) of treatment. Scale bar: 40 µm.**

This result is also reflected in the QCM signals in which we observed a fast change in frequency and dissipation, followed by a stationary trend.

Conversely, 10 µM of Noc treatment showed enough microtubule depolymerization at 30 min, during which some filaments were still present but completely disappeared at prolonged treatment (2 h). In the meanwhile, the compensatory effect of actin emerged with increased stress fibers formation (Figure 4.6).

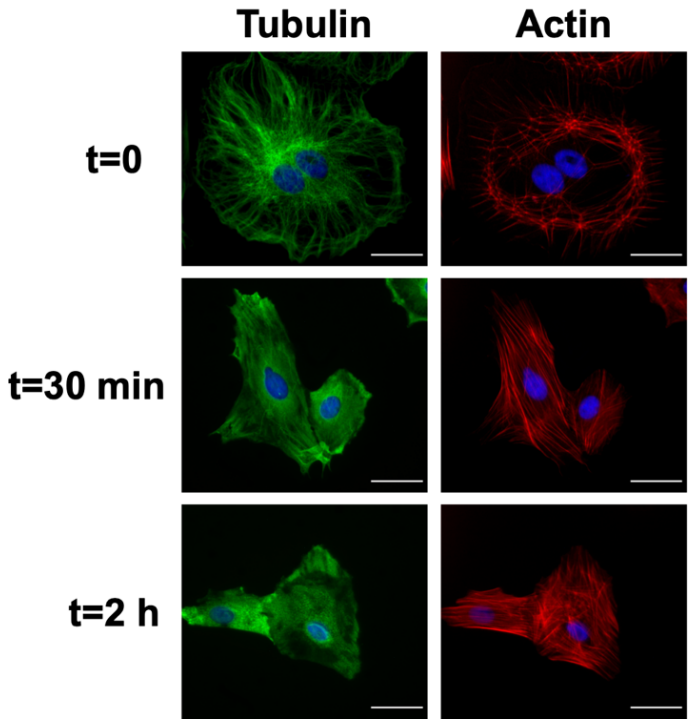

Figure 4.6. **Effect of 10 µM Noc treatment on cytoskeletal tubulin and actin. Fluorescent images for control (t = 0) and cells after 30 min (t = 30 min) and 2 h (t = 2 h) of treatment. Scale bar: 40 µm.**

This demonstrates that, despite Cyt-D, the absence of a steady-state condition in QCM profiles during the treatment is related to a continuous cytoskeletal rearrangement.

4.3.3. DHM Results

In order to confirm the deductions achieved from QCM results, DHM was employed by using experimental protocols, as explained in "Materials and Methods". For the multicell analysis, we performed three independent experiments (N = 3) from which we obtained an overall measurement of more than 30 cells for each measured group within the relative drug treatment. We decided to monitor different intervals of drug exposure by considering the rate of the drug's action on cytoskeletal biopolymers accessed by QCM and immunofluorescence. Thus, 5 µM Cyt-D treatment exerted a rapid effect on actin with a high contribution within 10 min, while in 10 µM Noc treatment, we observed a more time-dependent and progressive effect on cells. For this purpose, we analyzed treated cells at five different time points, which were 0, 10, 20, 40, and 60 min for Cyt-D and 0, 1, 2, 3, and 4 h for Noc.

From the numerical calculation after hologram reconstruction, we observed a progressive reduction in the projected area, due to Cyt-D, with more than 30% of reduction in the first 10 min and an overall decrease of 65% in 60 min of treatment (Figure 4.7a). Moreover, we observed an almost constant volume during the entire treatment period (Figure 4.7b). Conversely, in Noc treatment, we did not observe any evident morphological variations (Figure 4.8), even if prolonged drug exposure was monitored.

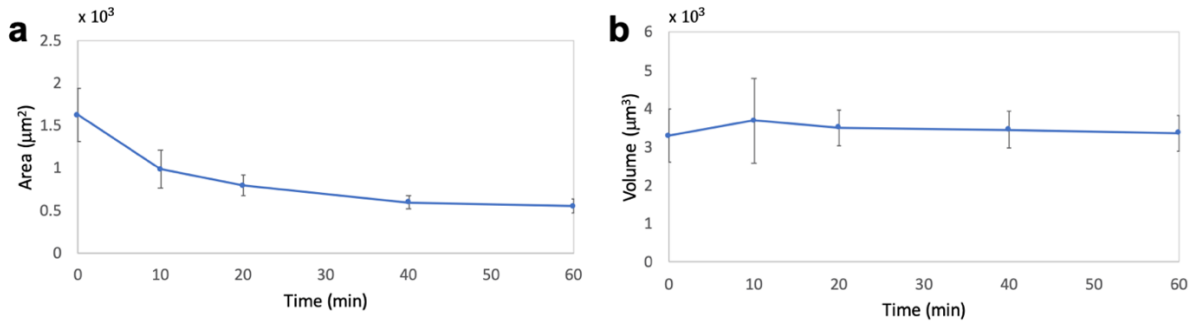

Figure 4.7. **Morphological parameters variations due to Cyt-D at 0, 10, 20, 40, and 60 min. Reported mean values and standard deviations for area (a) and volume (b) are relative to three independent replicas (m = 3).**

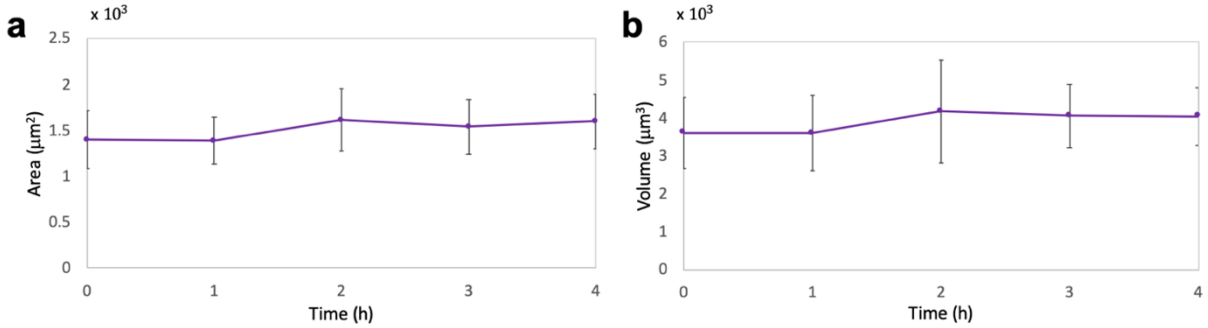

Figure 4.8. **Morphological parameters variations due to Noc at 0, 1, 2, 3, and 4 h. Reported mean values and standard deviations for area (a) and volume (b) are relative to three independent replicas (m = 3).**

Noc is known to act on fibroblasts cell shape with the displacement toward a more symmetric cell morphology with less polarity [215]; this is likely accompanied by a redistribution of the surface projected area, which led us to observe constant quantitative morphological trends.

These results confirmed the adhesive properties of the cells during the treatment and our morphological considerations about QCM signals.

In addition, the decreased area along with constant volume observed in Cyt-D treatment led us to consider a possible increase in cell thickness. For this reason, in order to achieve a complete morphological characterization, by exploiting the 3D quantitative information provided by DHM, we decided to delve deeper into the exploration of this treatment. For this purpose, we performed a single-cell analysis, as explained in "Materials and Methods". Time-lapse experiments (n = 5) were able to confirm the results of the multicell analysis with a higher relevance in the real-time monitoring, consistent with the QCM approach.

In Figure 4.9a, an example of the cells' hologram reconstruction corresponding to 0 and 15 min of Cyt-D treatment is shown.

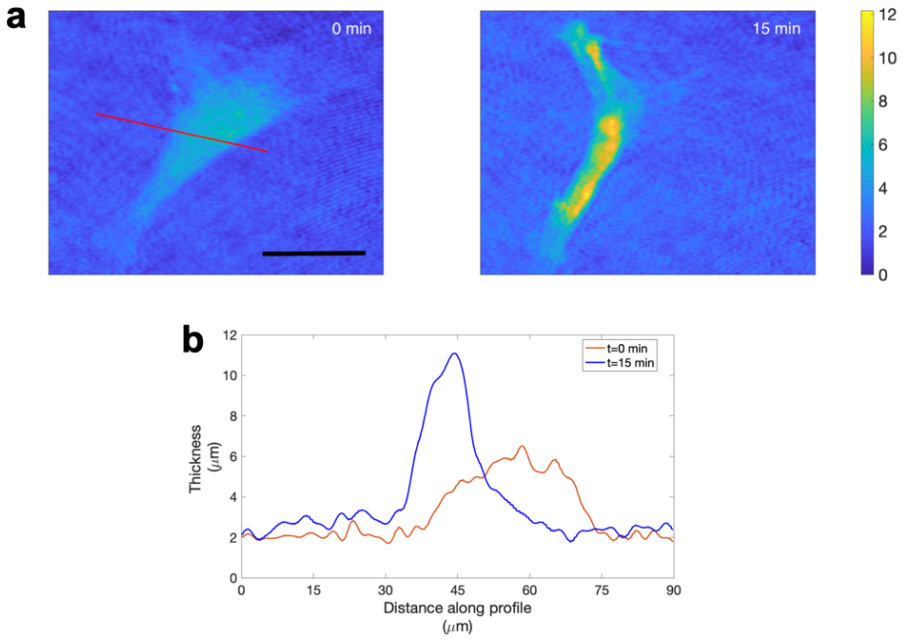

Figure 4.9. **Thickness map (µm) and cell-thickness profiles: (a) thickness map (µm) of reconstructed holograms extracted from the time lapses at 0- and 15-min. Scale bar: 50 µm; (b) cell-thickness profiles relative to t = 0 min (orange line) and t = 15 min (blue line) were plotted along the red line across the cell.**

For each time lapse, the projected surface area (PSA) and volume (V) were calculated, as explained in "Materials and Methods" for holograms corresponding to 0, 3, 6, 9, 12, and 15 min. Moreover, the mean height (V/PSA) was plotted in order to highlight the increase in thickness.

We were able to appreciate the increase in thickness also from the retrieved 3D images after reconstruction, and for comparing thickness profiles at different time points, we used MATLAB's Improfile function. We plotted the cell-thickness profiles by choosing a line that crossed the cell in a region where the retraction obviously occurred. In Figure 4.9b, it is possible to observe cell profiles for t = 0 min and t = 15 min relative to the red line shown in Figure 4.9a.

For all time lapses, we observed comparable results as the standard deviations suggest in Figure 4.10, in which the values for the mean percental variations in the area, volume, and mean height are presented. For plotting the results, the percental variations were calculated from the difference between the final and initial value, normalized to the initial one, and multiplied by 100 as follows:

$$\%\ variation = \frac{x_f - x_i}{x_i} * 100, \qquad (4.1)$$

where x corresponds to *PSA*, *V*, or *V/PSA* (mean height); i is the initial value, and f is the final value.

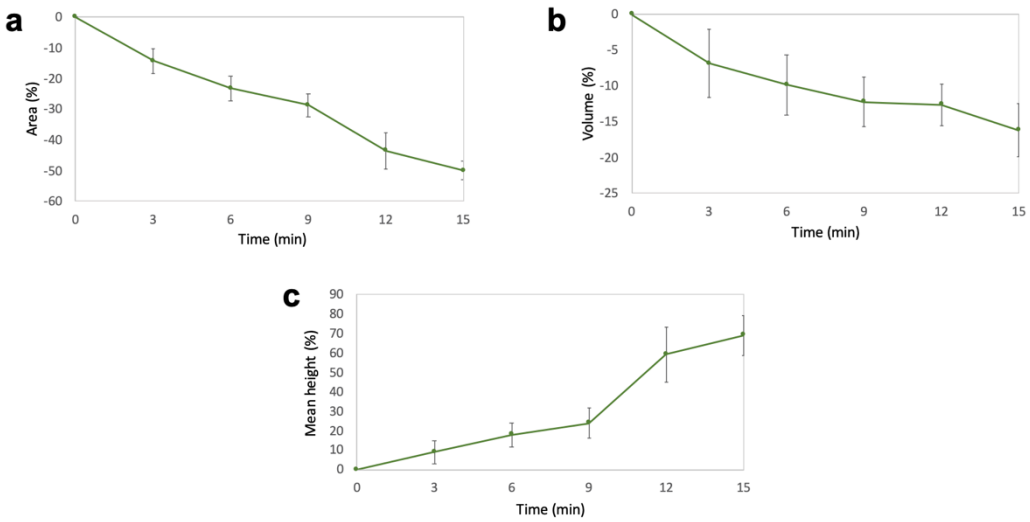

Figure 4.10. **Percental variations in area (a), volume (b), and mean height (c) obtained in single-cell experiments (n = 5) relative to 0, 3, 6, 9, 12, and 15 min of Cyt-D treatment.**

Moreover, we noticed clear comparability in the values extracted from all of the experiments performed in both multicell and single-cell analyses. In summary, we observed a decrease of about 30–40% in the projected area within the first 10 min of treatment and an overall decrease of about 50% in 15 min. This means that, in the last 45 min of treatment, the reduction was only about 25%. Therefore, this proved that the main contribution, due to Cyt-D, was verified within the first 15 min with a larger effect during the first 10 min. Moreover, by monitoring single cells, we were also able to calculate the cell's mean height by normalizing its volume upon the projected area, again marking the tendency of the cell thickness to increase over the treatment time.

Despite the morphological investigation, dynamical analysis was unable to provide us with quantitative evaluations. Since cell fluctuations (*CMF*) were in the instrumental noise range, we did not observe any dynamical variations for both treatments.

In conclusion, from quantitative phase information, we confirmed the morphological variation occurring during the Cyt-D treatment, which justifies the reduction in the mass in contact with the quartz surface and related effects on Δf and ΔD. In order to better understand QCM's frequency shifts, taking advantage of DHM quantitative information, an approximative estimation of the mass variation, occurring under Cyt-D action, was performed. We evaluated the mass variation sensed by quartz, within the penetration depth, due to area variation. For this calculation, values from the multicell analysis were used. The mean area value of untreated cells was considered, as well as that of treated cells at the end of one hour of treatment, which was presumably maintained constantly for the subsequent hours since no relevant changes in Δf and ΔD were observed. We believe that, if Sauerbray's equation is only considered, such a variation in mass should lead to a higher frequency shift (about 1300 Hz) than that observed; this demonstrates that Kanazawa's contribution must be involved in the interpretation of our results. Conversely, if Kanazawa's equation is only considered, an estimation of treated cells' viscosity could be achieved by considering the viscosity of a healthy cell. For example, by using the apparent viscosity of healthy 3T3 fibroblasts measured with QCM by Wegener et al. [156], we obtained a decrease of about 13% in viscosity after Cyt-D treatment.

However, during the treatment, we observed a morphological variation in cells in which the rounding up led cell bodies to be mostly outside the penetration depth of the acoustic wave. For this reason, the thus calculated decrease in viscosity is mainly influenced by the presence of medium rather than cells and cannot be interpreted as the real viscosity of cells themselves.

Despite the tentative assumption of simplifications for achieving quantitative information, under our working conditions, the elastic (Sauerbray) and viscous (Kanazawa) contributions cannot be decoupled, as previously stated. Even if QCM's signals depend on entities of different nature, such as mass, density, viscosity, storage, and loss modulus, there are currently limitations in modeling viscoelastic films composed of live cells, preventing us from the quantitative estimation of these parameters. Thus, unlike quantitative DHM analysis, only qualitative evaluation can be achieved from our QCM's results.

4.4. CONCLUSIONS

We used a new combination of approaches to achieve information on the near interface cellular dynamical variation. The use of two complementary techniques allowed us to overcome the complications related to the use of QCM in the cellular investigation. The lack of models for determining the cell layer behavior on the oscillating quartz allows for only qualitative interpretations. Quantitative DHM was used in this study to confirm the deductions by gaining information on morphological parameters such as area, volume, and cell thickness. We used and compared the effects of two cytoskeletal drugs able to interact with actin and microtubules. QCM was employed for studying the cell–substrate interface changes as a result of the effects of 5 μM Cyt-D and 10 μM Noc treatments for four hours, by measuring and analyzing the Δf and ΔD signals.

In agreement with a typical range of Cyt-D action, confirmed also by immunofluorescence, we observed consistent Δf and ΔD changes within the first 10 min after medium substitution. During the first hour, maximum values were reached, which were maintained almost constantly until the end of the experiment. This suggested the ability of QCM to detect the loss of cell-substrate adhesion and also decreased viscosity. Morphological variations were confirmed by quantitative DHM, which highlighted again the main contribution of Cyt-D within the first 10 min, without significant additional effect at prolonged exposure.

Despite Cyt-D, we did not observe any quantitative morphological variations in Noc treatment. This led us to the conclusion that QCM signals, in this case, can be interpreted as a direct result of cytoskeletal rearrangement rather than cell mass variations. In agreement with immunofluorescence, we observed a time-progressive effect on cells and thus on rheological properties. These results involved a double-step trend with the first redistribution of tubulin through the cytosol, with increased viscous behavior (increased G″), followed by the actin's compensatory effect and stress fiber formation, which led to a slight decrease in dissipation (increased G′) at prolonged drug treatment.

We should note that there are relatively few reports on the successful application of QCM for live cell studies. This could be due to the complications correlated to the execution of experiments, as well as the interpretation of their results. To our knowledge, this is the second study in which QCM real-time monitoring is used with primary cultures and the first in which primary cardiac fibroblasts are employed. Moreover, the combination of the two approaches allowed us to compare QCM results to the quantitative DHM technique, achieving synergic and complementary interpretation of cells behavior, with a focus on the near-interface layer.

In conclusion, we studied the rheological, morphological, and adhesive changes in primary cardiac fibroblasts treated with two known cytoskeletal drugs: Cyt-D and Noc. We were able to highlight the pivotal role of actin in maintaining shape integrity, adhesion stability, and mechanical structure. In fact, we observed that in its absence (by using Cyt-D), the cell's ultimate condition is marked by a loss of adhesion, with the highest possible detachment from the surface and liquid-like behavior. Conversely, cells devoid of microtubules are not involved in a compromised shape or adhesion and, as a result of a counterbalance play, their cytoskeleton emerged with increased actin stress fibers. This last line of evidence, reported also in other studies, could be justified by considering the

Tensegrity model's principles for which the cell' mechanical stability is guaranteed by a tensile pre-stress [190, 191].

The viscoelastic and morphological changes studied again reveal the importance of the right understanding of cellular reorganization that occurs when cells are subjected to defects.

Cytoskeletal alteration is known to be the cause of many diseases, such as cardiomyopathies. Even if our approach is relatively far from direct use in disease diagnosis, the lack of comprehensive knowledge regarding biophysical cell behavior needs to be filled, which is planned for future research. Therefore, a deep understanding of the interconnection between alterations in nano/microstructures and macroscopic behavior plays a central role in the development of future powerful biomarkers of mechanical nature for diagnostic purposes.

5 THE LOCAL MECHANOSENSITIVE RESPONSE OF PRIMARY CARDIAC FIBROBLASTS IS INFLUENCED BY THE MICROENVIRONMENT MECHANICS

This Chapter is dedicated to the results obtained by investigating the mechanosensitivity of primary rat cardiac fibroblasts and reported in the following submitted manuscript: *Braidotti, N.; Demontis, G.; Conti, M.; Andolfi, L.; Ciubotaru, C.D.; Sbaizero, O.; Cojoc, D. The local mechanosensitive response of primary cardiac fibroblasts is influenced by the microenvironment mechanics.*

It is well known that cardiac fibroblasts (CFs) preserve myocardial function and integrity through perceiving stiffness variations of the cardiac tissue by using various cellular mechanosensors, including the Ca^{2+} permeable mechanosensitive channel Piezo1. Nevertheless, how CFs adapt the mechanosensitive response to stiffness changes remains unclear. In this work we adopted a multimodal approach, combining the local mechanical stimulation (from 10 pN to 350 nN) with variations of culture substrate stiffness. We found that primary rat CFs cultured on stiff (GPa) substrates showed a broad Piezo1 distribution with particular accumulation at mitochondria membrane. CFs displayed a force-dependent behavior in both calcium uptake and channel activation probability, showing a threshold at 300 nN, which involves both cytosolic and mitochondrial Ca^{2+} mobilization. This trend decreases as the myofibroblast phenotype within the cell population increases, in accordance with Piezo1 reorganization and accumulation at plasma membrane adhesion sites. In contrast, the inhibition of fibroblasts to myofibroblasts transition with soft substrates (kPa) considerably reduces both mechanically- and chemically-induced Piezo1 activation and expression. Our findings elucidate how Piezo1 function and expression are regulated by substrate stiffness and highlight its involvement in the environment-mediated modulation of CFs mechanosensitivity.

5.1. INTRODUCTION AND AIM

Cardiac fibroblasts (CFs) are non-excitable cells that are present in the heart in large amount [70]. The key role of CFs consists in maintaining extracellular matrix (ECM) homeostasis, which, together with cardiomyocytes interaction, leads to the formation of a complex tissue texture [69, 70]. This is subjected to substantial remodeling during most cardiac diseases where CFs homeostatic role is impaired. In fact, when subjected to stress or injury, CFs undergo an activation process that leads to a phenotypic conversion into myofibroblasts (MFs). As already anticipated in Chapter 1, Section 1.6, MFs are characterized by a radically organized cytoskeleton and the neo-expression and incorporation of α-smooth muscle actin (α-SMA) into stress fibers. This guarantees the cells the ability to exhibit higher contractility and thus higher traction forces [218, 219]. Moreover, MFs are responsible for the increased production of ECM proteins inducing tissue stiffening [220, 221] and resulting, therefore, the primary drivers of fibrosis and related pathologies [69, 70, 218, 219]. In order to investigate the features related to the phenotypic conversion of quiescent fibroblasts to MFs, several studies exploited the modulation of substrate stiffness showing that stiff environments are suitable for establishing MFs phenotype [69, 87, 222]. This finding suggests the existence of a positive feedback loop, in which MF-induced stiffening promotes the activation of new fibroblasts and further raises the stiffness.

Among the most important mechanosensors involved in signaling the mechanical changes of the microenvironment associated with the fibrotic condition [223] there are mechanosensitive ion channels [61, 224].

Several non-selective ion channels are expressed in cardiac fibroblasts, as reviewed in our previous work [68]. However, most of the Transient Receptor Potential (TRP) channels, some of which are also expressed by CFs and have been historically reported as elements involved in mechanosensory processes, have recently confirmed to be intrinsically insensitive to membrane stretch [225]. Moreover, the Piezo1 channel [52] has been demonstrated to work as a stretch-mediated upstream activator of some of these channels [226-228], and has recently been confirmed as an important regulator of heart mechanobiology by initiating force-induced hypertrophic signaling in cardiomyocytes [229].

Importantly, calcium has been suggested to sustain most of the myofibroblasts' features by altering MFs collagen turnover, cell growth [230], proliferation and differentiation [231]. In addition, calcium signaling in CFs was proposed as a regulator of cardiac hypertrophy [232] while mitochondrial calcium signaling was suggested as a regulatory mechanism in MFs differentiation and fibrosis [233].

In light of this, we discussed in our previous work the evidence for Piezo1 involvement in the fibrotic mechanisms and hypothesized the potential advantages of directly targeting Piezo1 in CFs in the context of cardiac fibrosis [68]. More recently, Piezo1 was confirmed to be an essential mechanosensor for cardiac MFs features along with its implicated overexpression in stiff environment [234].

However, despite these promising accomplishments, a deep understanding of how various mechanical stimuli can regulate Ca^{2+} gating through mechanosensitive channels in CFs is still lacking. To quantitatively investigate this phenomenon, we mechanically stimulated primary CFs by local indentation and modulation of culture substrate stiffness, or a combination of both, and monitored their activity through calcium imaging. Local indentation was performed using two techniques: Optical Tweezers (OT) and Atomic Force Microscopy (AFM), which allowed us to span from piconewtons to nanonewtons and investigate a wide range of pressures, resembling those of the cardiac cycle. By culturing CFs on substrates with different degrees of stiffness (from GPa to kPa), we described how the mechanics of the environment modulate Piezo1 expression and activity in response to a local mechanical stimulus. We demonstrated that Piezo1 channel is primarily involved and regulates the response of CFs at all physiological states (quiescent fibroblasts and myofibroblasts). Overall, our findings evidence the essential role of Piezo1 in controlling fibroblasts mechanosensitivity, confirming its important role in microenvironment-mediated mechanotransduction which is at the base of cardiac fibrosis.

5.2. MATERIALS AND METHODS

5.2.1. Cell Culture

Post-natal day 6 neonatal Wistar rats were scarified (the study was conducted according to the guidelines of the Declaration of Helsinki and approved by the OPBA Committee of the University of Trieste, under the Italian Ministry of Education, University, and Research, Protocol Code 1FF80.N.PZB). Hearts were extracted from the abdominal cavity and placed in CBFHH (calcium and bicarbonate-free Hank's Buffer with HEPES) supplemented with 10 U/mL heparin (H3149, Sigma-Aldrich, St. Louis, MO, USA) and stored on ice. Thereafter, cardiac fibroblasts were isolated by trypsin digestion and cultured at 37 °C in a 95 % H_2O and 5 % CO_2 atmosphere in Dulbecco's modified Eagle's medium (DMEM), high glucose, GlutaMAX™, pyruvate (Thermo Fisher Scientific, Waltham, MA, USA), and supplemented with 10% fetal bovine serum (FBS) (Sigma-Aldrich, St. Louis, MO, USA) and 1% antibiotic-antimycotic (Thermo Fisher Scientific, Waltham, Ma, USA). For all the experiments fibroblasts were used at P1 after about 5 days in culture before passaging. Cell at a density of 1.04 cell/cm^2 were seeded in 35 mm petri dishes and used after 24- or 48-hours respect to the type of experiment. For experiments on petri coated with PDMS, the surface of the elastomer was first activated under plasma oxygen and then incubated in 20 μg/ml fibronectin

(F4759, Sigma-Aldrich, St. Louis, MO, USA). In parallel, petri dishes without elastomer were functionalized similarly and used as control.

For OT and immunofluorescence experiments, cells were plated on 18 mm diameter glasses at the same seeding density.

For qPCR, confluent cultures were cultured in T25 flasks or in petri dishes (60 mm diameter) prepared as described previously.

5.2.2. Calcium loading protocol

Fluo-8 AM, green fluorescent calcium binding dye (ab142773, Abcam, Cambridge, England) was used at 4 μM. After PBS 1X wash, the fluorophore was incubated for 50 minutes at 37°C in normal physiological saline solution (NPSS) composed by 140 mM NaCl, 5 mM KCl, 2 mM $MgCl_2$,1 mM $CaCl_2$,10 mM HEPES,10 mM Glucose. After incubation, the samples were washed two times with NPSS and de-esterification in the same solution was performed at 37°C for at least 15 minutes before the experiment. For Yoda1 experiment a solution of Yoda1 (CS-5095-5mg, Chemscene, Monmouth Junction, NJ, USA) in NPSS was injected into the sample at a final concentration of 20 μM.

5.2.3. OT stimulation and calcium imaging

The OT setup was used in several works of our lab previously [235]. For this work software improvement was done. The setup consists of an inverted microscope with high numerical aperture objective (Olympus 60x, NA=1.4 oil immersion, Olympus Corporation, Tokyo, Japan) and infrared laser at 1064 nm (IPG Laser, Burbach, Germany) which allows the optical trapping. A Focused Tunable Lens (EL-10-30- NIR-LD, Optotune AG, Dietikon, Switzerland) is computer controlled by the software provided and adjusted to displace vertically the focus of the optical trap and move trapped 3 μm in diameter silica beads (Bangs Laboratories Inc, Fishers, IN, USA). For the mechanical stimulation, sinusoidal oscillations were performed at a frequency of 0.5 Hz and a laser power of 70 mW for the entire acquisition time. A fluorescence path is then coupled to the optical apparatus and consists of a fluorescence excitation source (X-Cite XLED1, Excelitas Technology, Waltham, MA, USA) which excite Fluo-8 AM at λ=460 nm. The intensity of the LED was 25% with an external trigger set to 25 ms exposure with an interframe of 500 ms. Time-lapse images were then acquired with a CCD dual sensor camera (Orca-D2, Hamamatsu, Iwata, Japan) able to show bright field and fluorescent channels at the same time. The exposure of the camera was set to 25 ms and videos were acquired at a frame rate of 2 frame per second (FPS) starting about 10 seconds before performing stimulation. 100 cells coming from two different cultures, relative to different litters (one litter was made by 6 pups), were investigated.

5.2.4. AFM stimulation and calcium imaging

For AFM-mechanical stimulation silica beads of 5 μm in diameter were glued with UV sensitive glue (NOA 73 Norland Optical Adhesive, Jamesburg, NJ, USA) at the end of tipless cantilevers (NANOSENSORS™, TL-FM-20, Neuchatel, Switzerland) with nominal spring constant (k) of 0.5-9 N/m. A silica bead was picked under microscopy control, cured for at least 30 minutes with a UV lamp. Before each measurement the spring constant of bead-mounted cantilever was calibrated in the fluid chamber of measurements by using the thermal noise method [236].

The AFM module (NanoWizard II AFM JPK Instruments AG, Berlin, Germany) is coupled to an optical Axiovert 200M microscope (Carl Zeiss AG, Oberkochen, Germany) equipped with an X-cite® 120Q fluorescence illuminator (Excelitas Technologies Corp., Waltham, MA, USA), excitation-emission filter for FITC spectrum and a 40X/0.6 objective (LD Plan_Neofluar, Carl Zeiss AG, Oberkochen, Germany). Physical stimulations were performed as function of increasing applied forces: 150 nN, 200 nN, 250 nN, 300 nN, 350 nN while monitoring fluorescence of calcium binding dye. The stimulation ramps consist in: (i) approaching the cell at 10 μm/s speed, (ii) contact time 0.5 s, (iii) cantilever retraction from the cell at the same speed. Each cell was stimulated only once.

Fluorescence time lapse movies, started about 10 seconds before stimulation, for a total of 120 frames per each stimulation at 2 FPS were recorded by an XM10 monochrome CCD camera (Olympus Corporation, Tokyo, Japan), connected to a 0.63X adaptor tube, at exposure time of 200 ms. Two different cultures, relative to different litters, have been investigated. Since the cell responding trends were similar (Supplementary Material, Figure AI.1, Appendix I) all the stimulated cells were pulled together (N=105 cells).

For chemical Piezo1 channel stimulation with Yoda1 a 20X/0.3 objective (LD A-Plan, Carl Zeiss AG, Oberkochen, Germany) was used. Time-lapse videos were recorded at 2 FPS for a total of 650 frames and started about 10 seconds before Yoda1 injection.

5.2.5. Calcium transients analysis

The acquired fluorescence time-lapse movies were analyzed by a custom MATLAB code. In the case of mechanical stimulation (OT and AFM) a region of interest (ROI) was placed close to the physically stimulated cell area, and another one in the background. The differential fluorescence signal was calculated as follows:

$$\frac{\Delta F}{F_0 - B_0} = \frac{(F - B) - (F_0 - B_0)}{F_0 - B_0}$$

where F is the fluorescence signal within the cell ROI, B the fluorescence signal within the background ROI, F_0 and B_0 the mean fluorescence signals calculated for the first n= 4 frames over the two ROIs.

In the case of mechanical stimulation by OT and AFM, the background fluorescence fluctuation was very low and hence neglectable ($B= B_0$ with $B_0 \rightarrow 0$). A cell was considered to respond if the stimulus induced $\Delta F/F_0 > 0.01$.

For the analysis of Piezo1 channel chemical activation with Yoda1, fluctuation in the background (B) were observed due to the poor solubility of Yoda1 in aqueous media. In this case, the background signal could not be neglected and only responses exceeding the background fluorescence intensity variations ($\Delta F/F_0 > 0.1$) were considered.

5.2.6. Evaluation of cell elasticity

Cell stiffness was obtained by evaluating the Young's Modulus (E) of the cell, which was obtained by analyzing the force-distance curves acquired on single cells. Silicon nitride cantilevers (MLCT, E, Brucker, Camarillo, CA, USA) with nominal spring constant of 0.1 N/m were used to indent the cell at 0.5 nN and 5 μm/s. To obtain the E value for each measured cell, the approaching part of the force-distance curve was converted into force-indentation curve and fitted with the Hertz-Sneddon model (quadrilateral pyramid as indenter) at indentation depth of 200 nm [25, 237]. This analysis was performed by using the JPK DP software.

5.2.7. Immunofluorescence

Immunofluorescence was performed for the observation of actin, α-SMA and Piezo1. Cells were seeded on round glass coverslips (18 mm diameter) for 24 or 48 h before being fixed in paraformaldehyde 4% for 20 min. In the case of permeabilized samples, cells were incubated for 5 minutes in 0.1% Triton X-100. Both permeabilized and non-permeabilized samples were blocked with bovine serum albumin (BSA) 0.5% for 30 min. Thereafter cells were incubated for 1 h at room temperature in the following antibodies: primary antibody to mouse α-SMA (ab7817, Abcam, Cambridge, England, 1:500) and rabbit Piezo1 (15939-1-AP, Proteintech, Rosemont, IL, USA, 1:150). Secondary antibodies used were: anti-mouse Alexa 488 (ab150113, Abcam, Cambridge, England, 1:500) and anti-rabbit IgG H&L (FITC) (ab6717, Abcam, Cambridge, England, 1:500). For actin staining phalloidin-iFluor 555 (ab176756, Abcam, Cambridge, England, 1:1000) was incubated with secondary antibody for 30 minutes at room temperature. Finally, DAPI (GTX16206, GeneTex,

Irvine, CA, USA, 1:10) was incubated for 5 minutes. Samples were mounted by using ProLong™ Diamond Antifade Mountant (Thermo Fisher Scientific, Waltham, MA, USA, P36970). For mitochondria staining, living cells were incubated for 30 min at 1 μM with MitoTracker® Red CM-H2Xros (Thermo Fisher Scientific, Waltham, MA, USA, M7513) before being fixed.

Epifluorescent images were taken with microscope described in Section 5.2.4 equipped with a 63X/1.4 Plan Apo oil immersion objective (Carl Zeiss AG, Oberkochen, Germany). Confocal images were acquired through a Nikon A1R confocal microscope (Nikon Instruments Inc., Melville, NY, USA) equipped with 403, 488 and 560 lasers, with a z step of 0.1 μm and an 60x/1.4 Nikon Plan Apo oil immersion objective (Nikon Instruments Inc., Melville, NY, USA).

5.2.8. Quantitative PCR

Total RNA from primary rat cardiac fibroblasts was extracted with Rneasy Protect Mini Kit (Quiagen, Hilden, Germany, 74124). 1 μg of RNA was reverse – transcribed to cDNA using the PrimeScript RT Reagent Kit (Takara Bio USA Inc., San Jose, CA, USA, RR047A). Quantitative PCR was performed using SsoFast™ EvaGreen® Supermix (Bio-Rad, Hercules, CA, USA) on the CFSX384™ Real-Time PCR Detection System (Bio-Rad, Hercules, CA, USA). Plate was sealed and placed in CFSX384 Real-Time System (Bio-Rad, Hercules, CA, USA). GAPDH was used for normalization. Each sample in each group was detected in triplicate. The following sets of primers (Sigma-Aldrich, St. Louis, MO, USA) were used in the study:

Piezo1 forward primer: TACTGGCTGTTGCTACCCTG;

Piezo1 reverse primer: CCTGTGTGACCTGGTATGCT;

α-SMA forward primer: CCTCTTCCAGCCATCTTTCAT;

α-SMA reverse primer: CGAGAGGACGTTGTTAGCATAG;

GAPDH forward primer: AAGTTCAACGGCACAGTCAAGG;

GAPDH reverse primer: CATACTCAGCACCAGCATCACC.

Resulting data were visualized with CFSX Manager software. Data are shown as $2^{-(\Delta Cq)}$ (mean ± STD). For comparisons of two groups, Student's t-test was used.

5.2.9. Fabrication of soft substrates

To fabricate soft culture substrates, polydimethylsiloxane (PDMS) was used and prepared by mixing the silicone elastomer with the crosslinker (Dow Corning Corporation, Midland, MI, USA, Sylgard™ 184 silicone elastomer kit) at a ratio of 35:1 to obtain a Young's Modulus of 88 kPa [238-241]. After degassing in a vacuum chamber, the mixture was poured into a Petri dish (35 mm or 60 mm diameter) and cured in an oven at 65°C for 15 hours. Due to its intrinsic hydrophobicity, surface functionalization of the PDMS substrates is required to improve cell adhesion. For this purpose, after treatment with plasma O2 (40 W, 30 sec), the substrates were incubated with fibronectin (20 μg/ml) for 30 minutes at RT and then washed in PBS 1X.

5.3. RESULTS AND DISCUSSION

5.3.1. Local mechanical stimulation of primary rat CFs evokes force-dependent Ca^{2+} transients

We adopted a synergic approach combining OT and AFM to locally apply forces from few piconewtons to hundreds of nanonewtons and probe the CFs response.

To exclude possible culture-specific artefacts, primary CFs from two different cultures were used, derived from different hearts isolations. Cells were cultured for 24 h on stiff substrates (on the order of GPa) prior to the cellular response investigation. We started with forces between 10-50 pN

(corresponding to 3 Pa pressure) that were applied by OT in an oscillatory mode (0.5 Hz). An example of mechanosensitive activation is shown in Figure 5.1a,b. Silica microbeads (3 µm diameter) were pipetted into the sample chamber and one bead was trapped above the cell (green circle indicated in the brightfield image of Figure 5.1a). The trapped bead was moved up and down to touch the cell membrane exerting a maximum pressure of about 3 Pa. The contact with the membrane was monitored by tracing the bead position (green trace in Figure 5.1b). An increment of the fluorescence signal can be detected when the trapped bead adhered to the cell membrane while the laser trap continues to move. This signal was first observed in the ROI 1 (fluorescence) near the bead-cell contact and then it propagated towards the cell edge, as indicated by the signals corresponding to ROIs 2 and 3. At these pressures, the response of CFs was very weak, and only 1 % of cells responded, indicating that the activation of calcium permeable mechanosensitive channels in CFs requires higher pressures.

In order to increase the local pressures, we indented the cells with the AFM (Figure 5.1c-f). Since we did not observe relevant cell response at forces lower than 100 nN, we employed higher forces, in the range of 150-350 nN, with 50 nN force steps. These forces were applied with a microbead indenter (5 µm diameter) attached to the top of the cantilever (green trace in Figure 5.1d,f). Therefore, by considering half area of the bead surface as contact area [242], the applied pressure ranges from 4 to 9 kPa, which is close to the physiological pressures reported for the cardiac cycle [243, 244].

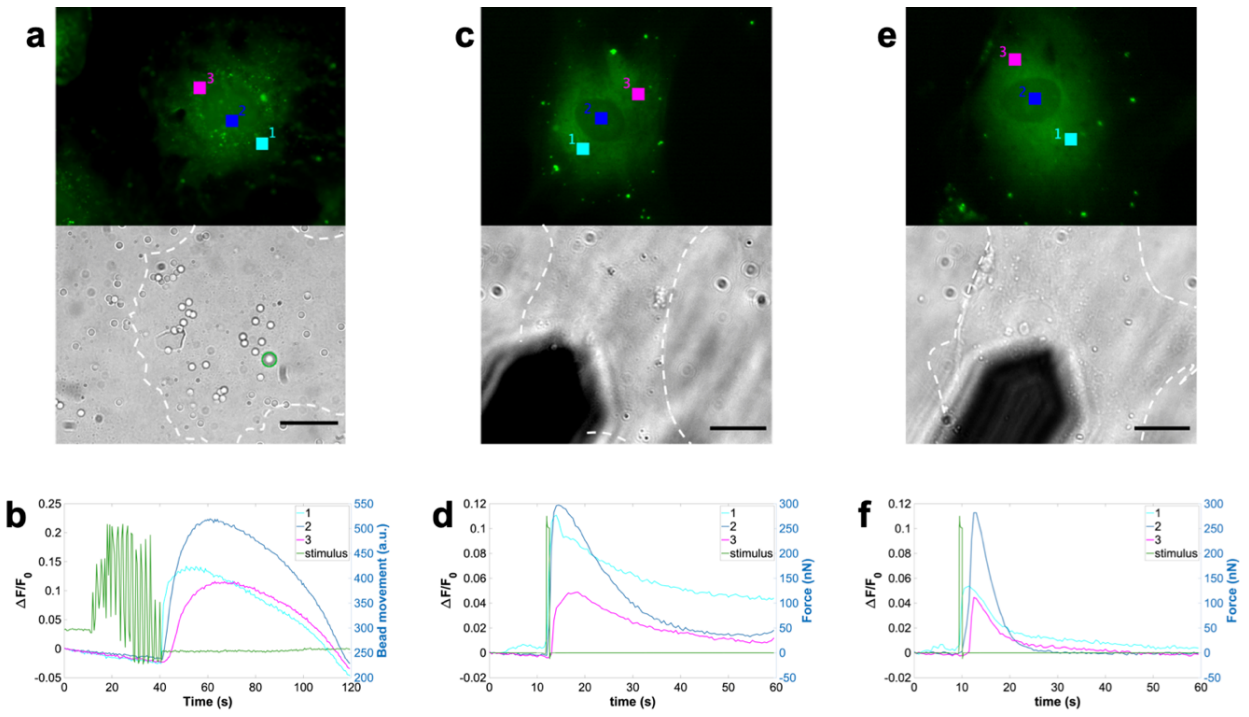

Figure 5.1. Stimulus-induced calcium signals evoked by using OT (a, b) and AFM (c-f). In (a, c, e) the upper channel corresponds to the fluorescent signal while the lower one is relative to the bright field. Owing to thin morphology of adherent fibroblasts which provides very low contrast in bright field image, cell boundary was marked for a better visualization. (b) The optical trapped bead movement (green) is overlapped to the $\Delta F/F_0$ signals. When the bead touches the cell membrane the fluorescence signal is detected first for ROI 1 (stimulated area, cyan signal) followed by its propagation to 2 (blue) and 3 (magenta). (d, f) Show examples of generalized and transitory response respectively highlighting the differences in the decay times (τ). ROI 1 (cyan) represents the cell-tip contact point, ROI 2 (blue) and 3 (magenta) are relative to areas in which calcium is propagated. Green traces correspond to the AFM stimulus. Scale bar: 20µm.

By analyzing the fluorescence signals induced by the stimuli, we observed two distinct types of cellular responses, which we called "generalized" (Figure 5.1d) and "transitory" (Figure 5.1f). In the "generalized" response, the fluorescence signal occurs immediately after tip-cell contact and

propagates across the whole cell. In this case, the fluorescence signal takes more than 10 s (τ>10 s) to decay by a factor of 3 from maximum (Figure 5.1d). Conversely, a faster decay (τ<10s) defines the "transitory" response (Figure 5.1f).

When AFM forces were applied, we observed an increased amount of responding cells compared to OT, as shown in Figure 5.2. Here we can clearly observe that the cells response increases with increasing forces. Moreover, we can see that the generalized response preferentially occurs at higher forces, as shown in Figure 5.2. In fact, the normalization of generalized responses over the sum of generalized and transitory, obtained by the formula:

$$\frac{\%\ Generalized}{\%\ Generalized + \%\ Transitory}$$

shows an increment from 66 % at 150 nN to 82 % at 350 nN.

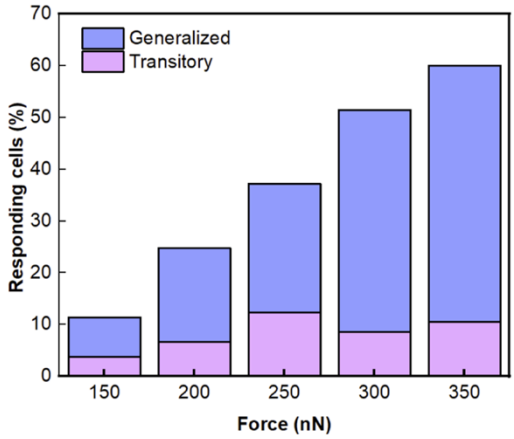

Figure 5.2. Percentages of CFs that exhibit force-dependent behavior with generalized and transitory responses to mechanical stimulation. Cells investigated came from two different replicas performed on different cultures after 24 h plating for a total of 105 cells for each force.

Interestingly, we observed that, in cells responding with a generalized behavior, the initial cytosolic Ca^{2+} influx is followed by a long lasting Ca^{2+} accumulation in inner filamentous elements that appear to be responsible for the longer decay time. To better understand this behavior, we analyzed the corresponding time-lapse fluorescence images. In Figure 5.3, frames extracted at time 0, 10, 30 and 60 s are shown for both the generalized (Figure 5.3a) and transitory (Figure 5.3b) responses. For the generalized response, 20 s after stimulus application, we can notice the presence of such structures indicating Ca^{2+} accumulation. Calcium release from these elements, resembling mitochondria [245, 246], is relatively slow. In fact, some of them are still calcium-enriched even 50 s after the stimulation. Such an event occurs preferentially at higher forces, where a higher percentage of generalized responses is observed, while it is less evident, or even absent, in transitory responses, as shown in Figure 5.3b.

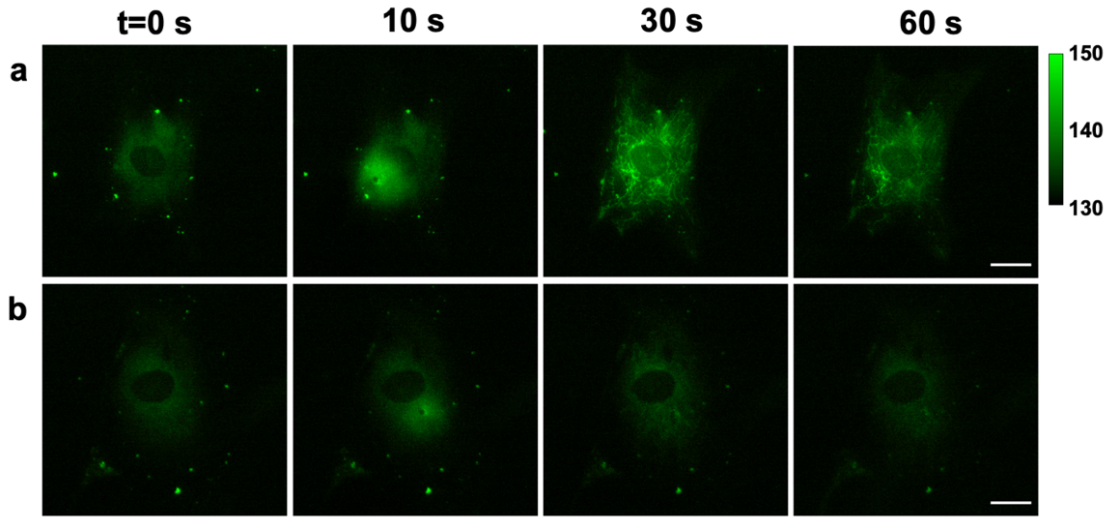

Figure 5.3. Frames extracted from time-lapse movies at t= 0, 10, 30 and 60 s are reported for generalized (a) and transitory (b) responses. Calcium uptake in filamentous-like structures at the intracellular side is evidenced for the generalized response at 30 s. Even at 60 s some of these structures are still visible supporting the long-lasting storage. Image contrast was adjusted to the same maximum and minimum intensity values and the corresponding color bar is reported on the top right. Scale bar 20μm.

Our observations are consistent with the role of mitochondria in buffering high cytosolic Ca^{2+} concentrations, culminating in long lasting calcium uptake respect to the cytosolic one [247]. Therefore, it is reasonable to hypothesize the presence of a force-dependent mechanism for Ca^{2+} storage in mitochondria.

To determine whether this mechanism is associated with increased calcium concentration at high forces, we evaluated the maximum $\Delta F/F_0$ values for each responding cell stimulated in the force range of 150- 350 nN. We indeed found that more calcium was mobilized (Figure 5.4) at higher forces, supporting the hypothesis that higher forces induce high Ca^{2+} concentration which led to mitochondrial calcium uptake.

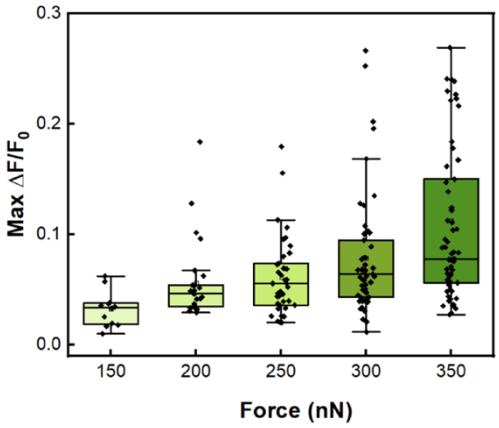

Figure 5.4. $\Delta F/F_0$ distribution for responding cells as function of the applied forces from 150 nN to 350 nN, (N=150 for each force). Ca^{2+} mobilization follows a force-dependent behavior which suggests that at higher forces an increased number of channels are stimulated.

To rule out the background fluctuations from the results of our measurements, we also analyzed the background fluorescence signals for each responding cell (Supplementary Material, Figure AI.2, Appendix I), and found them to be negligible.

Finally, to evaluate the activation threshold for CFs, we plotted the activation probability as a function of the applied force and fitted the experimental data with the Bell's function [248], using the formula:

$$P(F) = \frac{1}{1 + e^{\frac{-(F-300)}{80}}}$$

The fitting shows that at 300 nN we have a 50 % probability of the activation of the mechanosensitive channels (Figure 5.5).

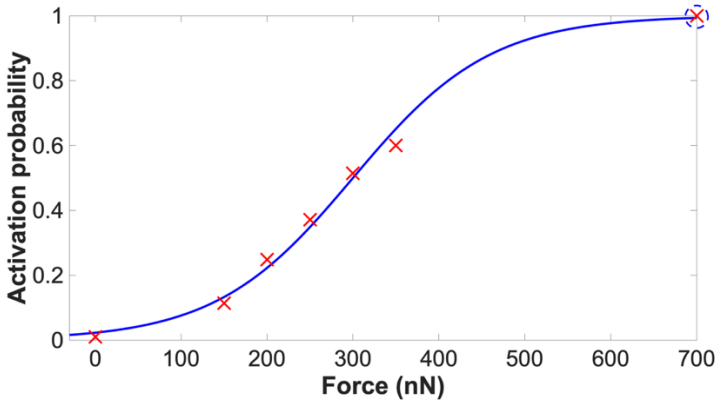

Figure 5.5. Channel activation probability fitted by Bell distribution (blue line). A threshold at 300 nN corresponding to 50 % of channel activation probability is observed. For the fitting we hypothesized a 100 % probability for 700 nN of applied force. Red crosses represent the experimental data.

On the base of these results, we suggest that the number of activated channels increases with the force (Figure 5.4), and that the force-dependent channel activation probability follows the Bell's function (Figure 5.5).

5.3.2. Piezo1 in CFs is localized also in mitochondria

To understand the extent of Piezo1 involvement in the response of CFs to mechanical cues, we examined the presence and localization of Piezo1 in CFs by immunostaining and confocal imaging. The analysis was performed both on permeabilized (Figure 5.6a) and not permeabilized (Figure 5.6b) cells for accessing both outer and inner information on its localization.

We found that Piezo1 is consistently expressed in CFs and highly localized in intracellular filaments (Figure 5.6a), with a distribution bearing the resemblance to the typical mitochondria morphology [245, 246]. Moreover, this organization is also similar to the filamentous structure detected in the mechanical stimulation experiments. To confirm this observation, we double stained permeabilized sample for Piezo1 and mitochondria (Figure 5.6c). As shown in Figure 5.6c, one can indeed notice the colocalization of mitochondria and Piezo1.

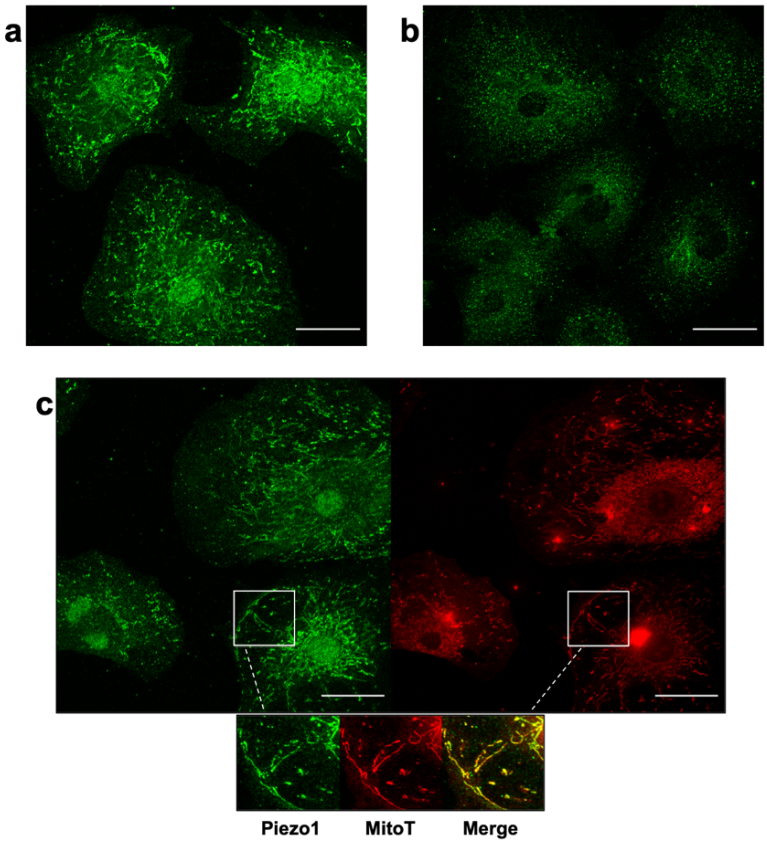

Figure 5.6. Piezo1 is colocalized with mitochondria. Permeabilized (a) and not permeabilized (b) samples stained for Piezo1 reveal a consistent protein expression both intracellular and at the plasma membrane. Permeabilized samples stained for both Piezo1 (green) and mitochondria (red) by using MitoTracker (MitoT) show the colocalization of signals (inlets) (c). Scale bar 40μm.

To our knowledge, Piezo1 localization in CFs' mitochondria is a new finding, accompanying the lonely similar report on the presence of Piezo1 at mitochondria in pulmonary arterial smooth muscle cells [35].

Additionally, the accumulation of Ca^{2+} at high stimulating forces, together with the localization of Piezo1 at the mitochondrial membrane, provides evidence for a Piezo1-mediated Ca^{2+} regulation to occur at the mitochondrial level when high cytosolic Ca^{2+} needs to be buffered.

We suggest a two-phase mechanism involving first the transmembrane Piezo1 in response to a local stimulation. When Ca^{2+} mobilization occurs, which was demonstrated to be force-dependent (Figure 5.4 and Figure 5.5), the second part of the mechanism involving Piezo1 at mitochondria could take place in order to manage the substantial amount of mobilized calcium [247].

This hypothesis suggests a double Piezo1 role (both at the membrane and intracellular) in managing high value force stimuli.

5.3.3. Myofibroblasts phenotype alters the mechanosensitive response to local stimulation

Based on the suggested Piezo1 role in implicated mechanisms linked to cardiac MFs phenotype [68, 234], we focused our attention on the investigation of the mechanical response of this fibroblast state.

A method to achieve a cellular population characterized by a natural increasing amount of myofibroblasts is to extend the culturing time [88]. Therefore, we investigated the influence of a myofibroblasts-enriched population cultured for 48 hours. We compared the results of stimulated cells at 24 and 48 hours after seeding (Figure 5.7a) and observe that for 48 h the percentage of responding cells increases with force, but the increment is lower as respect to that observed at 24 h.

To avoid artefacts due to culture-specific responses we investigated 24-48 hours cultured cells (N=45) by using the same culture.

The analysis of the maximum fluorescence intensity ($\Delta F/F_0$) indicates a similar trend, and also negligible background fluctuations (Supplementary Material, Figure AI.3, Appendix I), to that observed for 24 h. However, by comparing the 24 h with the 48 h values, a reduction in $\Delta F/F_0$ at 48 hours is highlighted (Figure 5.7b), which implies a lower calcium uptake.

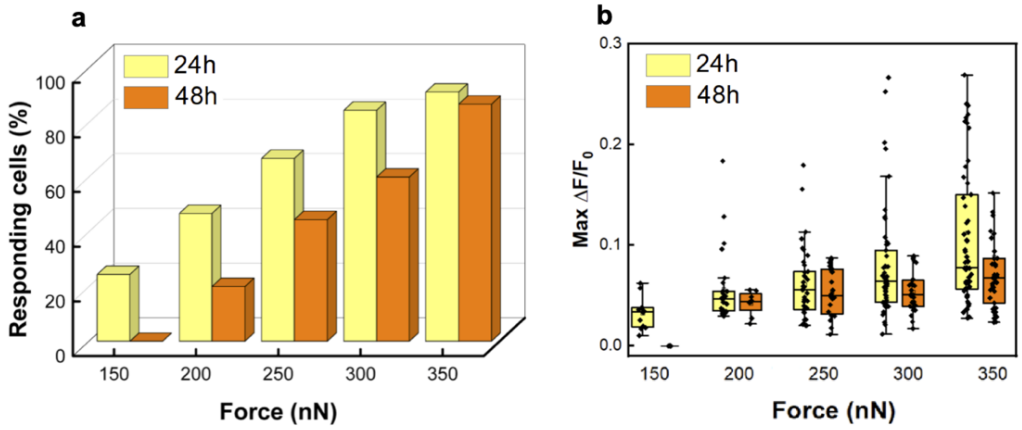

Figure 5.7. Differences in gating behavior between 24- and 48-hours cultured cells (N=45). The investigation of cells from the same culture and tested at 24 and 48 hours highlights the reduction in channel activation probability (a) and in $\Delta F/F_0$ values (b) corresponding to a lower calcium uptake and reduced stimulated channels number at 48 h.

Altogether these results indicate both a decrease in channel activation probability (Figure 5.7a), and a decrease in channel number expressed at the stimulated area, as shown by a decrease in calcium signal at 48 hours (Figure 5.7b).

In order to understand the reason for the different gating behavior, we performed a brightfield and epifluorescence microscopy analysis of the samples at 24 h and 48 h. As compared to 24 hours (Figure 5.8a), the cells at 48 h show enhanced spreading (Figure 5.8b), with increased actin stress fibers and α-SMA expression, primarily englobed in these structures rather than in the cytoplasm (Figure 5.8c).

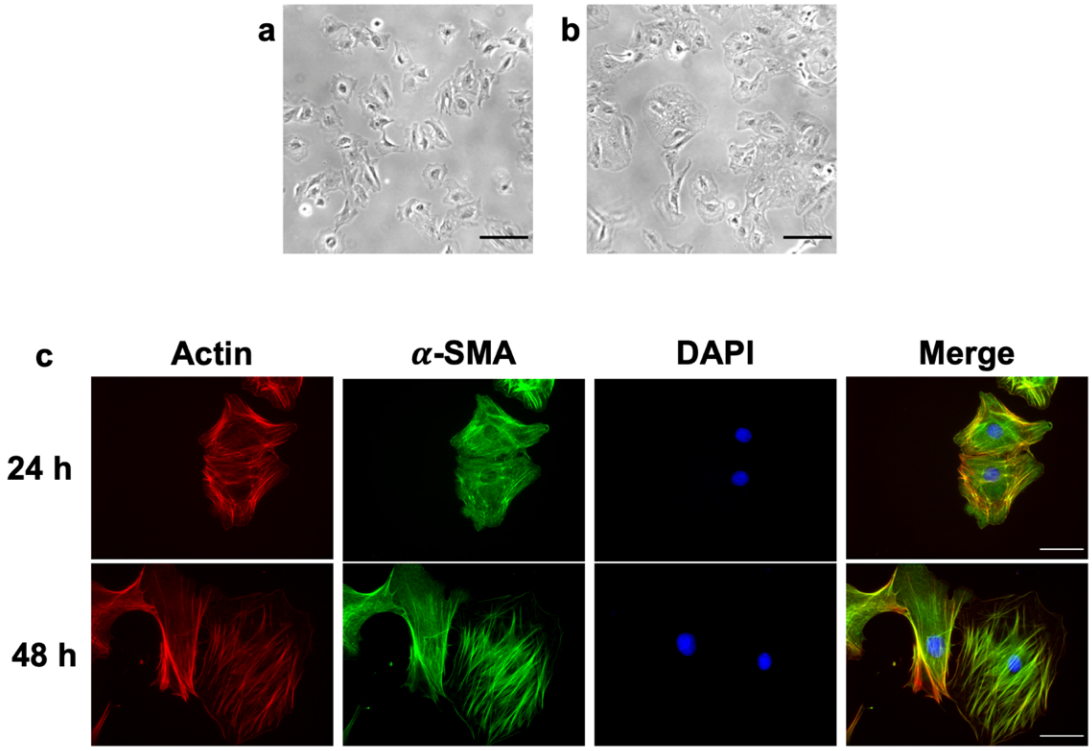

Figure 5.8. Brightfield and epifluorescence microscopy investigations. Brightfield images for 24 h (a) and for 48 hours cultured cells (b) show an increase in cell spreading with the time. Scale bar: 100 µm. Fluorescence images (c) for 24- and 48-hours cultured cells were obtained by staining cell for actin (red), α-SMA (green) and DAPI (blue). At 48 h an increment in α-SMA incorporation into actin stress fibers is observed, as evidenced by the merge image. Scale bar: 40 µm.

Immunolabelling for transmembrane Piezo1 showed not substantial differences between 24 and 48 h culture (Supplementary Material, Figure AI.4, Appendix I). Likewise, a similar channel expression between 24 h and 48 h was confirmed by both qPCR (Figure 5.9a) and by chemical stimulation with Yoda1, the selective agonist of Piezo1 (Figure 5.9b). Although previous works supported the increased expression of Piezo1 channels in activated CFs [234, 249], we did not observe any relevant differences in protein expressions. This is most likely because the myofibroblasts phenotype is preferred over the quiescent one even at 24 hours due to the stiff environment [5]. The myofibroblasts population increases over the time [88] and relative variations in Piezo1 expression between 24 and 48 hours could not be easily detected on the cells pool. On the contrary, is likely more probable to detect differences through mechanical stimulations which are performed on single cells.

In addition, we analyzed also the cell mechanics, to investigate whether the variation in cells elasticity could be responsible for a different gating mechanism. However even in this case we did not observe significant differences between the cell Young's Modulus for the two culturing times (Figure 5.9c).

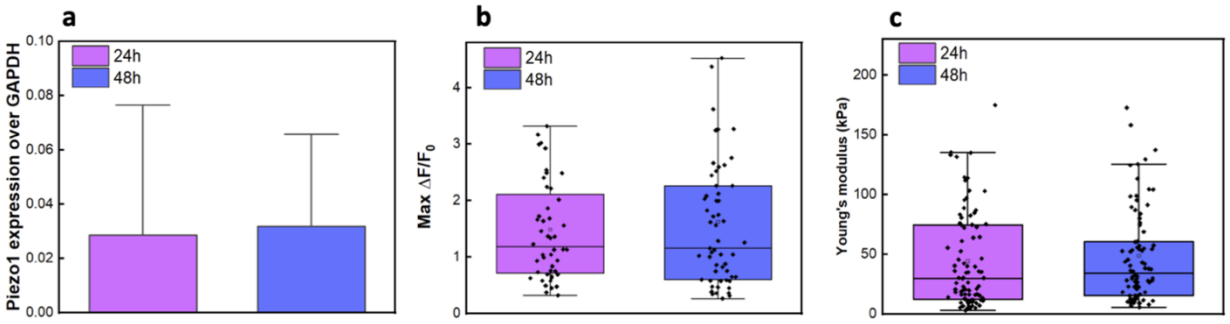

Figure 5.9. Neither changes in channel expression nor cellular mechanics are the underlying causes of different gating behavior between 24 and 48 h. (a) Piezo1 expression normalized to GAPDH for 24- and 48-hours cultured cells (n=3). (b) Distribution of $\Delta F/F_0$ values for all responding cells chemically stimulated with Yoda1 20μM (N=49 for 24h and 60 for 48h). (c) Young's Modulus measurement for 24- and 48-hours cultured cells, N=87.

These data suggest that the modulation of gating behavior is not caused by changes in channel expression or cellular mechanics. On the other hand, the increased spreading and a large integration of α-SMA into stress fibers characterize the cellular population at 48 hours, which involves an increased amount of myofibroblasts, known to develop high traction forces and contractility [218, 219]. Therefore, we can hypothesize that the different gating behavior may be correlated with these features.

5.3.4. Inhibition of myofibroblasts phenotype reduces Piezo1 mechanical and chemical activation

To better understand the activity of Piezo1 channels in CFs phenotypes, cells were grown for 24 hours on softer substrates, that can limit the activation of fibroblasts into myofibroblasts [69].

PDMS produced in ratio of 35:1, as described in Methods, refers to a stiffness of approximatively 88 kPa [238-241]. This results in a Young's Modulus that is about five order of magnitude lower than that of common culture polystyrene petri dish surfaces, which are typically on the order of GPa [250].

The analysis of α-SMA expression by qPCR confirmed a reduced fibroblast activation on softer substrates (Figure 5.10a), in agreement with data reported in the literature [69, 73]. At the previously determined threshold of 300 nN, no cell response was detected in cells cultured on PDMS as respect to the control, which instead confirmed a response of about 50 %. This prompted us to formulate two hypotheses: (i) the channel expression could decrease; (ii) the cell stiffness could decrease, requiring higher pressure to induce the membrane tension variation necessary to trigger the channel opening.

To assess these hypotheses, we performed several analyses. By using qPCR, we observed a decrease in Piezo1 expression on soft substrates (Figure 5.10b). Analogously, the Young's Modulus of cells decreases on soft PDMS substrates (Figure 10c), in agreement with what reported in [251]. Moreover, in this case we observed a narrower data distribution than with rigid substrate, reflecting a homogeneous population of quiescent fibroblasts. In parallel, a significant difference in chemical activation of Piezo1 with Yoda1 was observed (see Figure 5.10d), consistent with the reduced expression of the Piezo1 in qPCR.

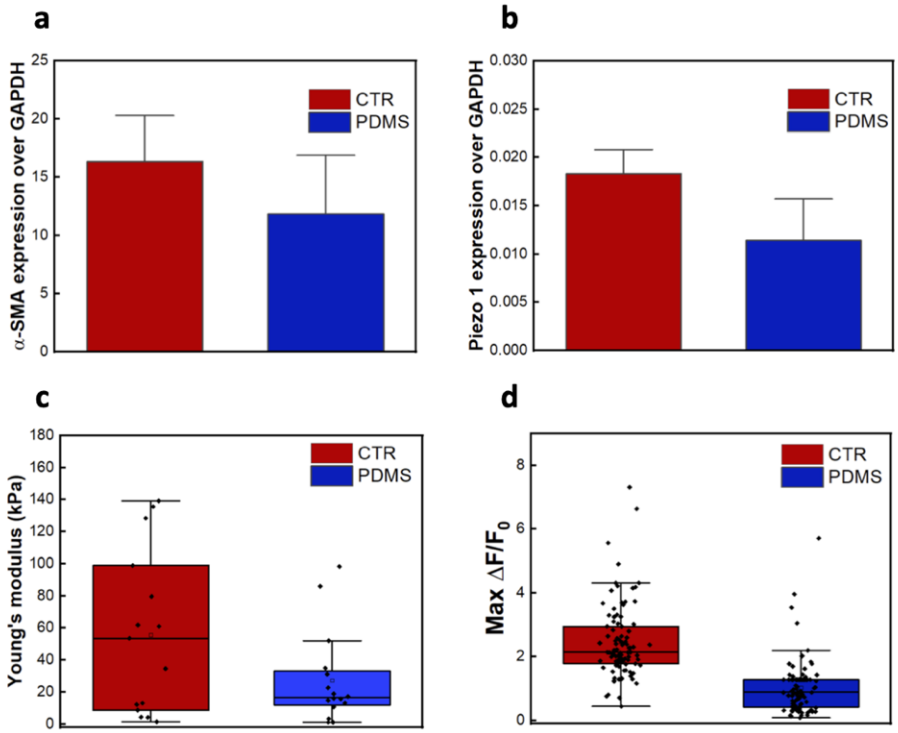

Figure 5.10. Inhibiting myofibroblasts content within the population lowered the cell elasticity and the channel expression, and, thus, also the mechanical and chemical channel activation. (a) α-SMA expression normalized to GAPDH for cells cultured on plastic (CTR) and elastomeric substrates (PDMS), n=3. (b) Piezo1 expression normalized to GAPDH for cells cultured on plastic (CTR) and elastomeric substrates (PDMS), n=3. (c) Young's Modulus for cells cultured on plastic (CTR) and elastomeric surfaces (PDMS) (N=17). (d) Distribution of $\Delta F/F_0$ values for all responding cells chemically stimulated with Yoda1 20μM (N=93 for CTR and 76 for PDMS).

These results indicate that the probability to mechanically stimulate Piezo1 is reduced owing to lower channel expression, and is likely to be further reduced by the cell softness, which could impair the proper conditions for Piezo1 activation, as demonstrated in previous works [252, 253].

5.4. CONCLUSIONS

Alteration of mechanical stimuli from cellular microenvironment is of great relevance in fibrotic diseases and determines the fate of the pathology. In particular, cardiac fibrotic remodeling, which is associated with almost every type of myocardial disorders, impairs cardiac compliance and relaxation, ultimately leading to heart failure [254, 255]. The mechanisms that drive the feedback loop pathological remodeling in fibrosis are largely based on an impaired fibroblasts mechanosensitivity [75, 101]. Therefore, to better understand this pathological condition, it is relevant to further investigate the cellular mechanisms involved in sensing and transducing biomechanical cues. The CFs mechanosensitivity has been described by solely considering the investigation of the mechanical response of CFs to the modulation of substrate stiffness. Several works investigated how the mechanical microenvironment can regulate CFs phenoconversion [69, 87, 222], cytoskeletal reorganization and proliferation [67, 256], and also calcium flickers [257]. However, from our knowledge there are no studies concerning the mechanosensitive channel function as a consequence of local stimulation of CFs. Moreover, this field is poorly investigated in relation to fibroblasts of any origin, with only few publications up to date [258, 259].

In addition, cells embedded in tissues are subject to complex three-dimensional stimuli; therefore, the adoption of bimodal mechanical investigations is required for a full description of CFs mechanosensitivity.

In light of these considerations, here we investigated not only the local mechanosensitive response but we were also able to define how this was modulated by the mechanical cues of the microenvironment. Thanks to this bimodal approach we found a force-dependent Ca^{2+} mobilization in CFs cultured on stiff substrates and observed that the calcium uptake involves both the cytoplasm and intracellular structures for higher forces.

Not only Piezo1 was found consistently expressed all over the cell, but we also detected a Piezo1 localization at mitochondria. Moreover, the long lasting Ca^{2+} uptake within intracellular filaments observed at higher stimulating forces, which is compatible with both mitochondria morphology and mitochondria role in buffering high cytosolic calcium concentration [247], allowed us to postulate a double role for Piezo1: at the cell membrane Piezo1 firstly transduces the mechanical stimuli while a Piezo1-mediated mechanism at the mitochondria level occurs in order to cope with high Ca^{2+} concentration.

Subsequently, by increasing the amount of myofibroblasts we detected a reduction in cellular response but similar channel expression. On the other hand, the increased spreading and α-SMA incorporation into stress fibers allow us to associate these MFs' features to the modulation of Piezo1 mechanosensitivity. In fact, based on the demonstrated force-dependent Piezo1 recruitment at the adhesion sites during spreading [260], it's reasonable to think that in MFs Piezo1 undergoes reorganization with preferential accumulation at the cell membrane. Therefore, the reduction in Piezo1 expression at the mechanical stimulated region balanced by the enrichment of Piezo1 at the opposite site (maintaining an equal channel expression) is the reason underlying the different Ca^{2+} gating behavior observed. Altogether these results likely highlight once more the channel role in regulating traction forces, focal adhesion maturation and substrate signaling [51, 260, 261], which are important features of fibrotic-driven MFs phenoconversion and persistence [262].

On the contrary, by limiting MFs presence using soft substrates [69] both mechanical and chemical Piezo1 activation are drastically reduced as Piezo1 expression diminishes. These findings suggest that Piezo1 is the main player in transducing mechanical cues in CFs, confirming the hypotheses discussed previously [68], making it a suitable target for blocking mechanically-driven fibrotic mechanisms, in which it is most likely involved. Cardiac fibrosis and implicated heart functional impairments are still a debated big challenge as well as a serious health and clinical problem. In fact, such cardiac remodeling driven by fibroblasts is a common feature of several cardiovascular diseases but effective specific therapies are still limited, and one of the main obstacles in this is the restricted knowledge of the fibrotic mechanisms [78, 263, 264].

During the initial optimization of protocols for culturing cells on soft substrates, PA hydrogels were first selected. However, some problems in cell compatibility were experienced. Despite we chose to not include PA discussions in the submitted work, preparation methods, drawbacks and preliminary results are provided in Appendix II.

6 INVESTIGATING MECHANOSENSITIVE CHANNELS ACTIVATION IN CONCERT WITH THE MECHANICAL PROPERTIES OF RED BLOOD CELLS

The present Chapter refers to the following work: *Braidotti, N.; Ciubotaru, C.D.; Rizzo, D.; Bergamo, L.; Bernareggi, A.; Cojoc, D. Investigating mechanosensitive channels activation in concert with the mechanical properties of red blood cells*. This work was accepted for publication in Discover Mechanical Engineering and is now in print. In this work we presented a novel multimodal approach for investigating both mechanical properties and Piezo1 activity at the same time in red blood cells.

The usefulness of our adopted approach resides in the fact that the activity of the mechanosensitive Ca^{2+} permeable channels expressed in the membrane of the red blood cells (RBCs) is determined both by the mechanical stimuli and the mechanical properties of the cell. Therefore, it is of most importance to correlate the triggering stimulus with the mechanical properties. In this work, we proposed an approach to determine the activation pressure of the mechanosensitive channels and concomitantly evaluate cell mechanical properties as Young's Modulus, membrane tension and viscosity, for individual cells. Cell deformation was accomplished by micropipette aspiration with a controlled pressure ramp and recorded by brightfield imaging to determine the mechanical properties. The Ca^{2+} transient was concomitantly monitored by fluorescence imaging, to get the activation pressure. The technique was validated comparing the behavior of three pools of RBCs, probed at different intervals of time after the cell suspension preparation by the same mechanical stimuli. We found relevant changes of the activation pressure, associated with the alteration of the mechanical properties, the latest becoming significant with the passage of time. Our approach opens a new direction to investigate the correlation between mechanosensitivity and mechanical properties for individual RBCs, which can be extended to other cells, in suspension or plated, under controlled environmental conditions.

6.1. INTRODUCTION AND AIM

It is known that the main function of the RBCs in the human body is to oxygenate the tissues and collect back the carbon dioxide [265]. To accomplish this function, RBCs require exceptional deformability due to the geometrical and chemical constraints in the circulatory system. Moreover, this property must be maintained for about 100,000 circulation cycles during their 120 days life cycle [265, 266]. RBCs have a biconcave shape minimizing the volume to surface area (60% the volume of a sphere with the same area surface) and a flexible membrane which confer them the possibility to easily change shape. The membrane encapsulates the hemoglobin solution and the underlying membrane skeleton, a two-dimensional network composed by actin filaments interconnected by spectrin tetramers bound to transmembrane proteins [267, 268]. This structure grants to RBCs an exceptional deformability, as well as the resistance to bending and shear stress [269]. However, these distinctive mechanical properties can drastically undergo changes under some pathological conditions, as for example in sickle cell disease, malaria, diabetes mellitus, and sepsis [270, 271]. Therefore, determining the mechanical properties of RBCs under different conditions had acquired a lot of interest and different techniques have been developed in the last two decades to this purpose: micropipette aspiration [161, 272], microfluidics [273], atomic force microscopy [274], ektacytometry [275], optical tweezers [180], optical stretcher [276] and acoustic tweezers [277]. All these techniques allow the measurement of single cells deformation under a controlled mechanical stress by using optical microscopy imaging and force recording, followed by the application of different biomechanical models to extract mechanical parameters as Young's Modulus, bending

modulus, membrane tension or viscosity. Beside these mechanical properties, morphological properties such as cell volume or surface area are also considered to assess cell functionality [278, 279]. For instance, volume regulation was evaluated in pathologies resulting from either overhydration and dehydration of erythrocytes [280].

The exchange of Ca^{2+}, Na^{+} and K^{+} cations through the membrane ion channels plays an important role for the regulation of the RBCs volume [266, 281]. Recently, Piezo1 channel was demonstrated to contribute in volume regulation [266] and gene mutations had been linked with RBCs dehydration and related pathologies [282].

Piezo1 is a mechanosensitive permeable cation channel discovered by Coste and collaborators [52] which can be activated by changes in the membrane tension [63, 283], regulating in turn the influx of Ca^{2+} in RBCs in response to the membrane stretch [266].

The influx of Ca^{2+} through the Piezo1 channel was shown to trigger the Gárdos channel and release of K^{+} ions and water from the cell [284], regulating in this way the RBCs volume [266]. Recently, the presence of the transient receptor potential channel vanilloid type 2 (TRPV2) was also reported in RBCs [285]. TRPV2 is a mechanosensitive non-selective Ca^{2+} permeable cation channel which contributes to the osmotic balance [285] and Ca^{2+} dissipation in storage lesion [286]. Even if TRP channels family is known to take part into the mechanosensory cell system, most of them have been demonstrated to be insensitive to membrane stretch [225] and being activated downstream of other channels such as Piezo1 [226-228].

The activation of the mechanosensitive channels depends on both the external mechanical stimuli and the mechanical properties of the cell. However, channel gating and mechanical properties of cells are usually studied separately on different pools of cells, and sometimes even employing different experimental approaches [274, 287]. Therefore, the possibility to make a correlation between gating behavior and mechanical properties for individual cells is lost in this way. Recently, we have introduced a bimodal imaging approach enclosing fluorescence and brightfield imaging to monitor calcium transients and stimulus probe position on the cell and study the activation of mechanosensitive channels in neuronal cells by piconewton forces applied by optical tweezers [235, 288]. Moreover, a micropipette aspiration technique with concurrent RBCs morphology imaging and intracellular calcium has also been reported by another group for the determination of the RBCs calcium dynamic range [169, 289]. Here we implement a similar bimodal imaging in combination with the micropipette aspiration technique, able also to retrieve mechanical properties of RBCs. Our approach is, thus, characterized by the multiple complementary information achievable at the same time from single cells. In fact, we determined the activation pressure by fluorescence Ca^{2+} imaging and simultaneously evaluated the mechanical properties (Young's Modulus, membrane tension, viscosity) by monitoring cell deformation versus the aspiration pressure. To validate the technique, we investigated human RBCs at three distinct intervals of time: 0-20, 20-40 and 40-60 min after their preparation, showing that both the activation pressure and the mechanical properties were subjected to changes during storing time.

6.2. MATERIALS AND METHODS

6.2.1. Combined micropipette aspiration and bimodal imaging setup

The experimental setup is based on our previously developed systems combining optical tweezers for mechanical stimulation with piconewton forces, electrophysiology, and bimodal imaging [235, 288]. Here, the employed micropipette aspiration module allows us to apply negative pressures in the range 0 to -60 mbar, attracting single RBCs to the pipette tip and drawing them into a capillary.

The picture in Figure 6.1a illustrates the setup with the inverted microscope (Olympus IX 81), the pressure control (Press-ctrl) Flow ZE (Fluigent, Le Kremlin-Bicêtre, France), the dual CCD camera

Orca D2 (Hamamatsu, Tokyo, Japan), the micromanipulator MM (Narishige, Tokyo, Japan), the halogen lamp (HL), the LED system (X-Cite XLED1, Excelitas Technology, Waltham, MA, USA), the sample chamber and the motorized microscope stage (SC-MS).

As it is shown in the layout of the setup (Figure 6.1b), the cells are placed in a fluidic chamber (Coverslip clamp chamber. ALA Sci. Instr., Farmingdale, NY, USA) and illuminated by the HL through a high pass optical filter F to remove the light with wavelength $\lambda > 750$ nm. Thus, brightfield imaging is achieved, without exciting the fluorescence dye, through a microscope objective MO (Olympus 60X, NA 1.25, Olympus Corporation, Tokyo, Japan) on one of the two CCD sensors of a dual CCD camera (Orca D2, Hamamatsu, Tokyo, Japan). A LED at λ=460 nm (X-Cite XLED1, Excelitas Technology, Waltham, MA, USA) is used to excite the calcium indicator Fluo-4 (F10471, Fluo-4 Direct™ Calcium Assay Kit, Invitrogen, Waltham, MA, USA) and the fluorescence image is obtained on the second sensor of the dual camera.

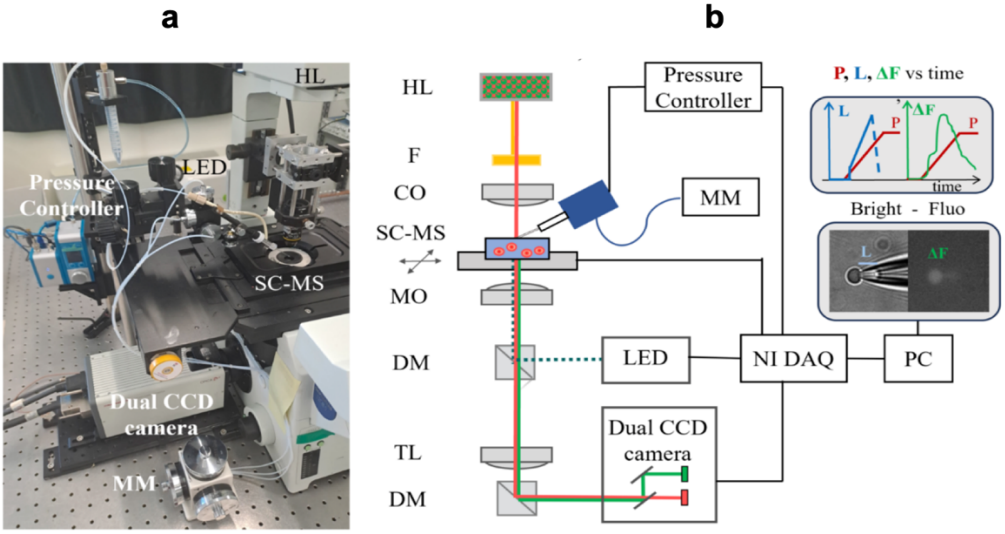

Figure 6.1. Combined micro-pipette aspiration and bimodal imaging setup. a) picture of the setup; b) scheme of the setup: HL – halogen lamp, F – optical filter, CO – condenser objective, SC-MS – sample chamber and microscope stage, MO- microscope objective, DM – Dichroic mirrors, TL – tube lens, MM – micromanipulator; the bimodal imaging (inset) shows the cell entering the micropipette and forming a tether of length L (left side) together with the fluorescence corresponding to the activation of the mechanosensitive channels (right); the top inset shows the variation of the applied pressure P, tether length L and fluorescence ΔF.

Applying a low negative pressure ramp (typically -2 mbar / s) the cells move towards the micropipette until the closest one touches the tip and starts to deform expressing a tether of which length L increases with the increasing pressure P (inset Figure 6.1b). At higher pressure the cell is then eventually sucked into the pipette, in the region with larger diameter. The signals from the pressure control, LED system and camera are acquired by a digital acquisition board NI DAQ (National Instruments, Austin, TX, USA) and controlled by custom software, allowing the synchronization of the pressure, cell deformation - tether elongation, and fluorescence signals. Each recording was performed using the LED at 30% of max power with 50 milliseconds exposure, to minimize the bleaching of the fluorescence dye, and at an acquisition rate of 7 frames per second to properly follow the cell deformation. The differential fluorescence signal for the actual frame, *s* is calculated as: $\Delta Fs = (Fs-F0)/F0$, where Fs is the mean fluorescence intensity over a circular region of interest (ROI) of which diameter is defined by the cell in contact with the pipette, and $F0$ is the mean intensity for the first 4 frames, calculated over the same ROI. The background signal ΔFb is measured in the same manner for a background ROI. The final fluorescence signal is calculated as: $\Delta F = \Delta Fs - \Delta Fb$. In few

cases we observed cell rupture after consistent pressure values, where the fluorescence suddenly peaks to high levels. These cases were excluded from the statistic.

6.2.2. Definition of the activation pressure and mechanical parameters

By plotting the pressure and fluorescence signals versus time, as in the example shown in Figure 6.2a, we determined relevant pressure values as defined below:

- **contact pressure, *Pc*** is the pressure corresponding to the first elevation of the fluorescence signal; this small signal is due to the change of the cell shape when it gets in contact with the pipette;
- **activation pressure, *Pa*** is the pressure corresponding to the second fast elevation of the fluorescence signal, reflecting the Ca^{2+} gating as a consequence of mechanosensitive channels opening; *Pa* is chosen as the pressure value corresponding to the differential fluorescence value $\Delta F = \Delta Fc + c*\Delta Fm$, where ΔFc and ΔFm are the fluorescence values at contact and the maximum fluorescence value and *c* is a constant chosen by the user (we chose c=0.1 here).
- **maximum aspiration pressure, *Pma*** is the pressure taken at the time when the fluorescence signal ΔF drops down: $\Delta Fma = 0.9 * \Delta Fm$, indicating the detachment of the cell from the tip of the pipette. This event is confirmed also by the cell morphology change observed in brightfield.

The plot of the pressure versus the tether length (L) allows to determine the elongation $\Delta L = L - L0$, with respect to the value at the contact ($L0$). The variation of the cell diameter during aspiration can also be determined from the brightfield movie.

With the above explained pressure, fluorescence and morphological parameters we can introduce some other characterizing the viscoelastic properties of the cell, using the definitions introduced by Hochmuth [290].

1) Young's modulus, E, given in [Pa]:

$$E = 11.4 * \frac{\Delta P}{\Delta L} * Dp \tag{6.1}$$

where: $\Delta P = Pma - Pc$, $\Delta L = L - L0$, Dp is the pipette diameter

2) Cortical tension, Tc, in [N/m]:

$$Tc = 1.1 * E * Dp \tag{6.2}$$

3) Velocity of the tether pulling into pipette, Vt, in [µm/s]:

$$\Delta L = Lma - L0 \qquad Vt = \frac{\Delta L}{\Delta t} \tag{6.3}$$

where ΔL, is the elongation of the membrane tether between the initial length $L0$ evaluated just after the contact to the maximum length Lma reached just before the cell is sucked into the larger diameter part of the capillary.

4) Cell Viscosity, ν in [Pa s]:

$$\nu = \frac{Dp\Delta P}{12\left(\frac{\Delta L}{\Delta t}\right)\left(1-\frac{Dp}{Dc}\right)} \tag{6.4}$$

where *Dc* is the diameter of the cell outside the tip.

6.2.3. Pipettes preparation

Pipettes were obtained from borosilicate capillaries (Warner Instruments, Hamden, CT, USA, model No. G150-6, OD: 1.50 mm, ID: 0.86 mm, length: 15 cm) using the Narishige puller PP-830 (Narishige, Tokyo, Japan). Temperature steps were selected to obtain pipette with a diameter of about 2 µm. To refine the tips, the polishing was achieved with the Narishige micro-forge MF-830 (Tokyo, Japan). The inner diameter (2 µm) is maintained for a length of 12 µm. After that point the diameter increases abruptly to the original diameter (0.86 mm), as shown in Figure 6.2b, allowing the collection of many cells and hence multiple experiments with the same pipette.

6.2.4. Cell culture and sample preparation

Human blood samples from adult patients were anonymously provided by "Maggiore" Hospital, Trieste, stored at +4°C and used within the following three days. RBCs were obtained from centrifugations and dilution steps in DPBS (14190-094, Thermo Fisher Scientific, Waltham, MA, USA). Then the cell suspension was incubated in 1x Fluo4 solution (F10471, Fluo-4 Direct™ Calcium Assay Kit, Invitrogen, Waltham, MA, USA) for one hour in the dark at +37°C. Cells were then washed by centrifugations in DPBS three times and one more wash was performed in HBSS (L0612, Biowest, Nuaillé, France). Thereafter, cells were 1:100 diluted in a 1:1 solution of HBSS and RPMI (61870010, RPMI 1640 Medium, GlutaMAX™ Supplement, Thermo Fisher Scientific, Waltham, MA, USA) with 10% of Fetal Bovin Serum (FBS). Cells were let to sit in the dark for 20 min. Finally, the final sample was obtained by diluting 1:100 once more the cellular suspension and stored at room temperature. We run experiments on 10 different patients. Each sample was subjected to a maximum acquisition time of 1 hour. Post-experiments and during data analysis, investigated cells were then grouped into three pools (P1, P2 and P3) relative to three different intervals of time (0-20, 20-40, 40-60 min) respect to the time passed from the sample preparation.

6.3. RESULTS AND DISCUSSION

To validate our approach, we explored for a possible correlation between the aspiration pressure required to activate / open the mechanosensitive channels and the mechanical properties of human RBCs. During the preliminary experiments, intended to optimize the aspiration protocol, the sample with RBCs was kept about 1 hour in the sample chamber to perform different aspiration experiments. Since from the brightfield images we noticed that the RBCs tendency to deform slightly differently after 20-30 minutes we decided to run a deeper analysis. Therefore, we considered three pools of cells, according to the time passed from cell preparation: P1, 0-20 min; P2, 20-40 min; P3, 40-60 min. The same experimental protocol, described in Section 6.2.1, was applied to each of the three groups of cells.

An example of a typical experiment is illustrated in Figure 6.2, showing the pressure and the fluorescence signals as a function of time (Figure 6.2a), and two bimodal images showing the cell deformation and the Ca^{2+} mobilization at two different moments (Figure 6.2b).

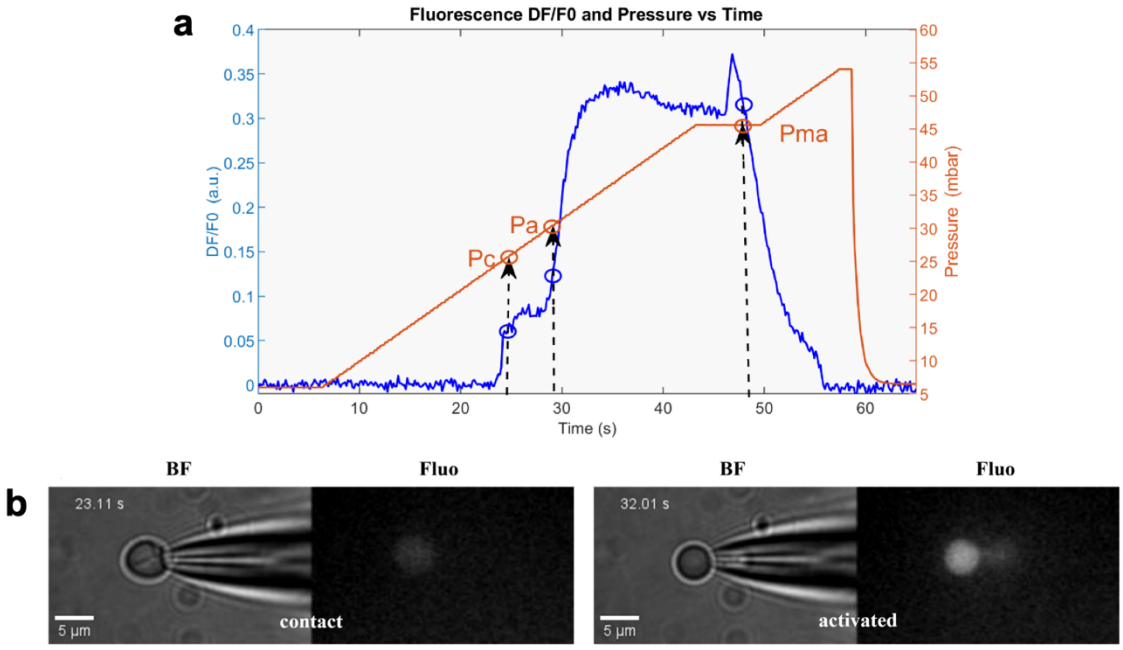

Figure 6.2. Example of data plot from a typical aspiration experiment. a) The pressure values: *Pc, Pa* and *Pma* are determined using the differential fluorescence ΔF curve and the criteria defined in Section 6.2.2. The scale relative to the aspiration (negative) pressure is reported in absolute values. b) Two bimodal images showing the cell morphology and the fluorescence intensity at two different instants of the aspiration: the cell gets in contact (left) and the tether is pulled into micropipette (right) inducing the mechanosensitive channels activation indicated by the elevated fluorescence intensity.

We ran experiments with human RBCs from 10 different patients in 6 different days, samples were prepared by following the protocol described in Section 6.2.4. We tested N1=130 cells for the first pool P1, N2= 70 cells for the second pool P2 and N3= 50 cells for the third pool P3 of RBCs. The differential fluorescence ΔF was firstly evaluated to determine the activation values Δfa corresponding to the channel activation. Responding cells were considered if $\Delta fa > 0.02$, a value which is about four times higher than the maximum of the fluorescence noise, extracted from the background fluorescence fluctuations during the experiment. Thus, excluding cells which did not satisfy the responding criterium, the number of considered cells for further analysis was reduced to: N1= 108, N2= 42 and N3= 21 respectively. This means that about 83.1 % from the first pool, 60 % from the second pool and 42 % from the third pool of cells responded to the mechanical stimuli, indicating that the activation probability is reduced during the storing time. We assigned this trend to possible changes of the cell properties but also to the fluorophore instability and bleaching.

The activation pressures values and their distributions were calculated for the responding cells and data were fitted with the Boltzmann function [291]:

$$Prob = \frac{1}{1+e^{\frac{-(P-b)}{a}}} + c \tag{6.5}$$

where *Prob* is the activation probability corresponding to pressure *P*, and *a*, *b* and *c* are numerical parameters defining the shift and tilt of the fitting curve. When $P = b$, the probability *Prob*= 50% and the corresponding pressure value, *P50* is considered as the activation pressure characterizing the pool of cells. The experimental data and the fitted curves are presented in Figure 6.3 for the three groups of cells. The activation pressures corresponding to 50% probability (*P50*) and relative to the fitting parameter *b*, are: *P50_1*= 18.6 mbar, *P50_2*= *P50_3*= 21.65 mbar, showing that the activation pressure value *P50* for the first pool of cells (0-20 min) is lower by about 3 mbar than the activation

pressure corresponding to the second (20-40 min) and third (40-60 min) pools. These values fall in the range of pressures previously investigated [169, 266] and observed to be necessary for calcium mobilization in RBCs. In particular, due to the absence of intracellular stores, the signal observed should be assigned to Ca^{2+} influx which is dependent on Piezo1 activation as suggested by Cahalan and collaborators [266]. The values of the second fitting parameter, *a* indicating the spreading of the data, are: *a_1=4.6*, *a_2=4.8*, *a_3=5.9*. The values of the parameter *c*, are close to 0 for all the three fits (-0.04, -0.06, -0.05). As one can notice from the Figure 6.3, the first two curves, corresponding to pools P1 (red) and P2 (green) are similar, while the third (P3 – blue) is tilted more, indicating a larger spreading of the activation pressure data.

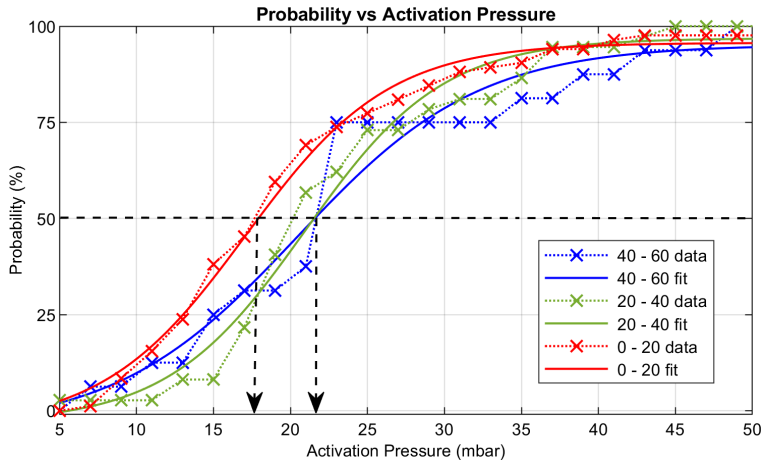

Figure 6.3. Activation Pressure distributions, experimental data (dotted line) fitted with the Boltzmann fit function for the three pools of cells: P1(red), P2 (green), P3 (blue).

By calculating the mean and standard deviation of the activation pressure (*Pa*) values for each of the three pools of cells (Table 6.1), we observed that the mean values are higher than the activation pressures at 50 % probability (*P50*) in all three cases. The standard deviations are big, indicating wide data spreading. Moreover, since the distributions are not normal (see Figure 6.4a,b) and the samples are independent and of different sizes, we compared them by using the Wilcoxon rank sum test, which takes the null hypothesis as equal medians [292]. The box plots illustrated in Figure 6.4c indicate that the null hypothesis is rejected (p-value, $p< 0.05$) only for the pair of samples P1-P2 ($p=0.01$), which means that the activation pressure medians of the pools P1 and P2 are significantly different. Few experiments (cells) for which the activation pressure was found out of the range [5 – 60 Pa] were excluded from the box plots in Figure 6.4c, even if they satisfied the criterium of the fluorescence threshold, because too low or too high values for the activation pressure are not practical.

	P1 0-20 min		P2 20-40 min		P3 40-60 min	
	Mean	std	Mean	std	Mean	std
Activation Pressure, *Pa* [mbar]	22.55	11.3	24.76	8.8	25.47	11.5
Young's modulus, *E* [Pa]	57.83	46.3	67.24	49.8	113.57	48.4
Membrane Tension, *Tc* [pN/um]	96.7	76.1	125.1	87.5	187.4	79.8
Tether velocity, *Vt* [um/s]	1.13	1	1.12	0.9	0.54	0.5
Viscosity, ν [Pa s]	208	204	277	244	527.02	331.5

Table 6.1. Mean and standard deviation values of the activation pressure and four mechanical parameters of the RBCs tested by micropipette aspiration.

In conclusion, we found that the activation pressure at 50 % probability, *P50* calculated by fitting the experimental data with the Bell's function was lower for P1 than P2 and P3. Moreover, the activation pressure mean values indicated an increase from P1, to P2 and P3 with a significant difference between P1 and P2. Altogether these results suggest that storage in the sample chamber alters RBCs mechanosensitivity even after just 20 minutes.

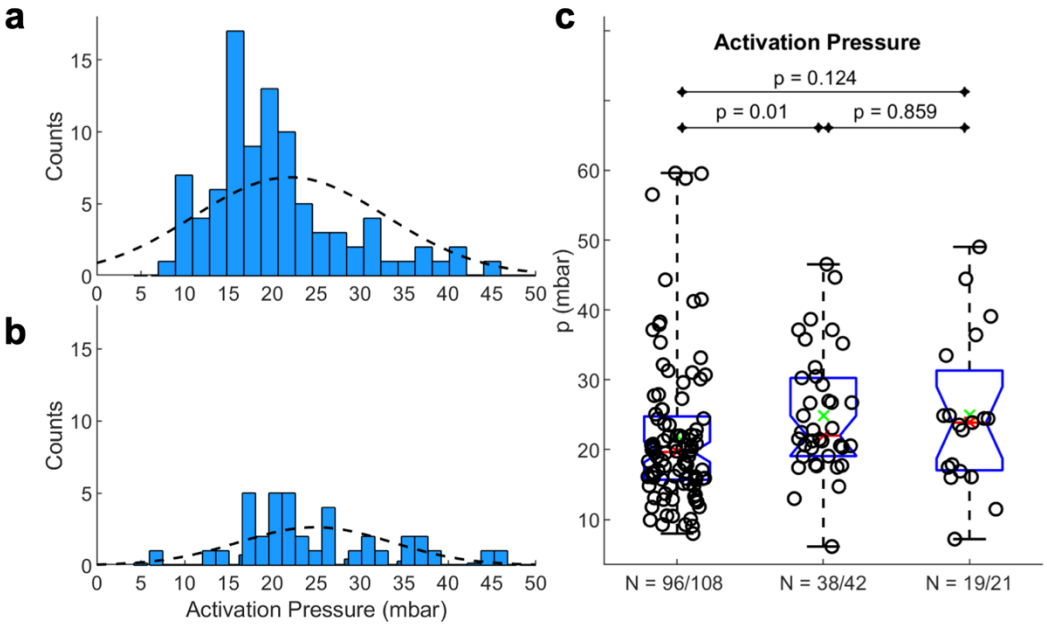

Figure 6.4. Histograms of the activation pressure distributions for the pools of cells P1, 0-20 min (a), P2, 20-40 min (b) and the box plot representation with the p-value resulting from the Wilcoxon test for all the three pools of cells (c). N represents the number of cells for which the values of the activation pressure are within a practical range: *Pa* [5 – 60 mbar].

Since the cortical membrane tension was recognized as one of the cell mechanical parameters which can modulate the activity of the mechanosensitive channels [283] and based on the possibility to run concurrent measurement of the cell deformation in our approach, we decided to determine also the associated mechanical parameters: Young's Modulus (E), membrane cortical tension (Tc), the flow velocity (Vt) of the cell tether pulled into the pipette and the viscosity (ν), as defined in Section 6.2.2.

The mean and standard deviation values shown in Table 6.1 indicate that the storing time produces an increment in the values of the following parameters: E, Tc and ν, while Vt is decreases. However, by checking the distributions we found that they are once again not normal and hence, to interpret the data, we proceeded with the box plot representation and the Wilcoxon test.

The results are shown in Figure 6.5 and indicate a significant difference for both pools P1 and P2 with respect to pool P3, while the differences between P1 and P2 are not significant.

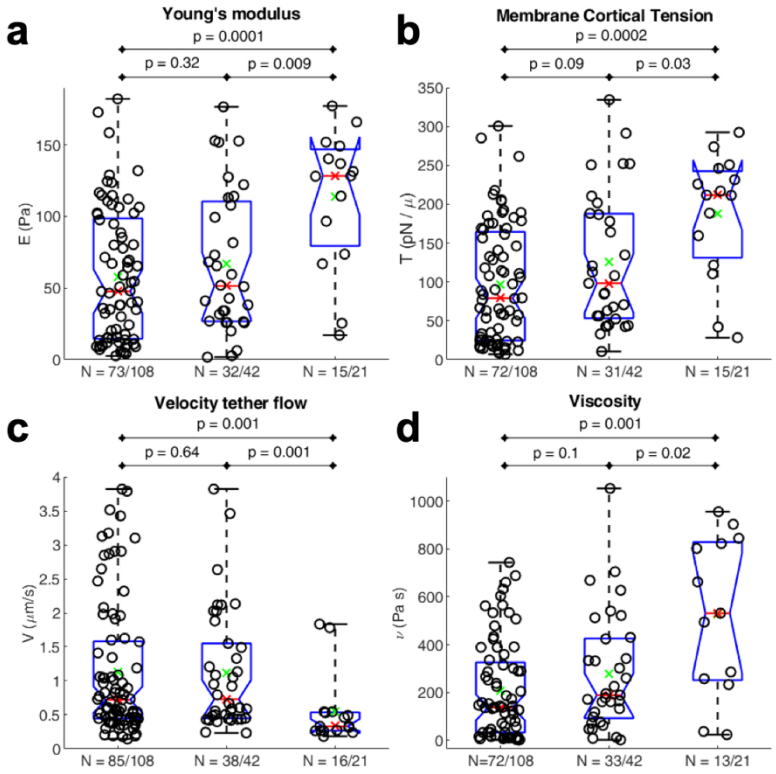

Figure 6.5. Box plot and Wilcoxon test (p-values) for the mechanical parameters: Young's Modulus (a), cortical membrane tension (b), tether flow velocity (c) and viscosity (d). N represents the number of cells (over the number of responding cells)) for which the values of the mechanical parameter are within a practical range: *E* [5-185 Pa], *Tc* [5-350 pN/µm], *Vt* [0.1 – 4 µm/s], *ν* [5-1100 Pa s].

In the comparation of these results with the activation pressure ones, one can observe that the mechanical properties are also altered with the storing time, but this alteration is retarded with respect to the activation pressure change. Interestingly, the activation pressures at 50 % probability for P2 and P3 are equal, and higher than the activation pressure for P1, suggesting that after a relatively fast change, this parameter remains stable. This is also confirmed by the significant difference found in the activation pressure mean values by comparing P1 and P2. Nonetheless, we also obtained two unexpected results: 1) cells mechanical properties are changed after about 40 minutes, and 2) the alteration of the activation pressure preceded that of the mechanical properties.

It is known that RBCs mechanical properties can deteriorate during anaerobic storage, but this was observed after days and not after just tens of minutes [293]. The alteration after about 40 min that we observed here might be due to the experimental conditions, which are different from the blood storage conditions. In fact, for our Ca^{2+} imaging in aspiration experiments, cells are loaded with Fluo-4 fluorescence dye and maintained at low concentration in buffer solution consisting of HBSS, RPMI and FBS. Despite differences in interval times, our results are consistent with literature. For example, the increment in cell stiffness, as evidenced by the increment in Young's Modulus assessed by us, agrees with storing time experiments performed by Xu and collaborators [294]. Moreover, the increment in viscosity which accompanies the stiffening is also well demonstrated [295-297]. At the same time also the rise in tension is compatible with published observations [298], while the reduction in cell velocity which suggests an increased resistance to flow as a consequence of increased viscosity finds also support in literature [267, 299].

Our work evidenced a relatively short experimental shelf time (about 1h), after which the morphology and the deformation properties of the cells changed considerably, making the experiments irrelevant.

Thus, the time becomes a critical methodological aspect to be considered when this type of cell mechanics experiment is planned for RBCs and possibly also for other types of cells.

As for the second unexpected result, although we have not yet found a convincing explanation for the preceding of channel gating variations to the mechanical properties changes, we hypothesize that the local membrane-associated elements such as cholesterol may result firstly affected inducing membrane tension alterations [300] and mechanosensitive channels activity modulation [301]. This may be then followed by cytoskeletal reorganization which effect emerges at longer time scale (> 40 min) and mechanical properties impairment. It's reasonable to think that the activation pressure might result further affected after a significant alteration of the mechanical properties. Unfortunately, we could not follow properties variation for more than 1 hour with the cells in the sample chamber due to the instability of the fluorophore.

6.4. CONCLUSIONS

We introduced a new approach for measuring the activation pressure of mechanosensitive channels in RBCs, at the same time with some mechanical properties evaluation. A bimodal microscopy including brightfield and epifluorescence imaging was implemented to monitor in parallel cell deformation and mechanosensitive channels activation during RBCs aspiration into a glass micropipette by a negative pressure which decreases at a constant rate. Even if a similar approach has no previous reports from our knowledge, we compared our results to published data obtained by independent investigations with different techniques. The analogy found in our results with respect to the literature reported ones is the proof that our bimodal approach can precisely measure both mechanical properties and assess channel functionality at the same time with superior strengths.

We found that both activation pressure and the mechanical properties change during 1-hour cells storing in the sample chamber. Unexpectedly, we found that the activation pressure was altered before mechanical parameters changes could be noticed and remained stable after these changes occurred. We think that the alteration of the mechanical properties after longer times would further influence the activation pressure but, unfortunately, we could not run experiments longer than 1 hour to check this hypothesis, due to the fluorophore instability. To further understand how much the activation pressure is correlated to altered mechanical properties of the cell, in future we plan to use drug treatment to induce significant changes in the actin filaments of the cytoskeleton, and thus induce mechanical properties changes in shorter time.

7 LABEL-FREE ANALYSIS OF URINE SAMPLES WITH IN-FLOW DIGITAL HOLOGRAPHIC MICROSCOPY

In this last Chapter results published in *Gigli, L.; Braidotti, N.; Lima, M.A.d.R.B.F.; Ciubotaru, C.D.; Cojoc, D. Label-Free Analysis of Urine Samples with In-Flow Digital Holographic Microscopy. Biosensors 2023,13,789* are reported. These are focused on the validation of a novel approach exploiting DHM. The work had been carried on in collaboration with Alifax srl, an international company working in the hematology, microbiology, molecular biology, serology and autoimmunity fields, and promoting the production of innovative diagnostic tools.

The work allowed the validation of an alternative method for fast bacteria analysis in native urine samples. The leading motivation of such investigation resides in the great demand of urine samples from patients to be precisely screened as a consequence of urinary tract infections which are among the most frequent infectious diseases. However, a high percentage of samples result as negative after urine culture plate tests (CPTs), requiring a simple and fast preliminary technique to screen out the negative samples. We propose a DHM method to inspect fresh urine samples flowing in a glass capillary for 3 min, recording holograms at 2 frames per second. After digital reconstruction, bacteria, white and red blood cells, epithelial cells and crystals were identified and counted, and the samples were classified as negative or positive according to clinical cutoff values. Taking the CPT as reference, we processed 180 urine samples and compared the results with those of urine flow cytometry (UFC). Using standard evaluation metrics for our screening test, we found a similar performance for DHM and UFC, indicating DHM as a suitable and fast screening technique retaining several advantages. As a benefit of DHM, the technique is label-free and does not require sample preparation. Moreover, the phase and amplitude images of the cells and other particles present in urine are digitally recorded and can serve for further investigation afterwards.

7.1. INTRODUCTION AND AIM

Urinary tract infections (UTIs) are among the most common infections, with major impacts on the individual health and social cost of the healthcare system [302]. UTIs include the presence of bacteria in urine and hence the detection and measurement of bacteria concentration represent important means to support diagnosis based on clinical symptoms. To evaluate UTIs, the urine culture plate test (CPT) is the gold standard method [303]. However, the CPT has the disadvantages that it usually requires more than 24 h and it is costly. Faster and more cost-effective approaches, based on dipstick analysis, are not satisfactory in terms of specificity and sensitivity [303, 304]. Urine flow cytometry (UFC) is an attractive alternative for diagnosis of UTIs, leading to a reduction in cultures and antibiotics [305-308]. One of the most diffused UFC systems on the market is the Sysmex urine particle analyzer UF-1000i, which uses fluorescence flow cytometry technology, offering two separate channels: one for bacteria and one for sediment particles [309, 310]. The sample, after being prepared by mixing the urine with a diluent and staining solution at a specific ration, is delivered to a flow cell using a sheath flow technique to produce a single-object stream which is intercepted by a laser beam. Fluorescence forward- and side-scattered light signals are detected and analyzed. Recently, a new flow cytometer (UF-5000) proposed by Sysmex [311] included an additional depolarized side-scattered light for better discrimination of red blood cells and crystals and the ability to differentiate Gram-negative bacteria.

Traditional flow cytometers and flow microscopes, as presented above, provide single-cell fluorescence signal and 1D or 2D spatial information on the objects suspended in liquid jet. Conversely, DHM is a phase imaging technique that provides phase information (optical path difference, OPD) and hence 3D information of the sample [127]. Several DHM instruments with different optical configurations have been commercially proposed for living cell studies. Some examples include Ovizio [312], LyncéeTec [313] and Phase Holographic Imaging PHI AB [314]. For instance, the Ovizio system has been recently employed for label-free leukemia detection by using in-flow DHM to extract cell parameters as the optical volume and height [312]. The technique employs sample preparation and 2D hydrodynamic focusing.

Different versions of custom DHM have been reported in the literature in the last years for new applications in biomedicine. Thus, quantitative phase imaging (QPI) has been proposed to extract spatial signatures of cancer cells by discriminating the different stages of oncogenesis [315]. A set of 15 parameters, derived from the cellular 3D morphology and texture have been extracted for suspended healthy and cancer cells (without flow). These quantitative phase-based parameters were useful to discriminate cancer cells. Since QPI allows accurate measurement of single-cell dry mass, it was undertaken to improve the diagnostic accuracy of malignancy in urine cytology [316]. QPI of unstained samples on ThinPrep urine cytology slides from 28 patients with four categories of cytological diagnosis (negative, atypical, suspicious and positive for malignancy) were analyzed. Nuclear/cell dry mass, their entropy and nucleus-to-cell mass ratio were calculated for several hundred cells for each patient and were then correlated with follow-up diagnoses.

Despite these promising DHM applications, to our knowledge, there are no studies reporting the use of DHM for urine analysis in flowing samples. In this paper we introduce an in-flow DHM method to analyze urine samples from patients without any sample preparation. The sample flows in a capillary and a DHM movie is recorded for 3 min. Bacteria and other particles present in urine are detected from numerical reconstruction of the holographic movie using the size, shape and OPD value as parameters. Samples are classified in positives and negatives according to standard clinical cutoff values for bacteria, white blood cells, fungi and epithelial cells. The presence of red blood cells and crystals is also discussed. DHM results are compared with the results obtained with UF-1000i and CPT for the same samples, showing a similar performance as UF-1000i, when compared to CPT as a reference.

7.2. MATERIALS AND METHODS

7.2.1. In-Flow DHM

The measurement setup is composed of a custom digital holographic microscope (DHM) based on a Mach-Zender interferometer, a capillary positioned on a xyz microstage, fluidics tubing and a syringe pump (Smart Syringe Pump, Parker, Hendrik-Ido-Ambacht, The Netherlands), as shown schematically in Figure 7.1.

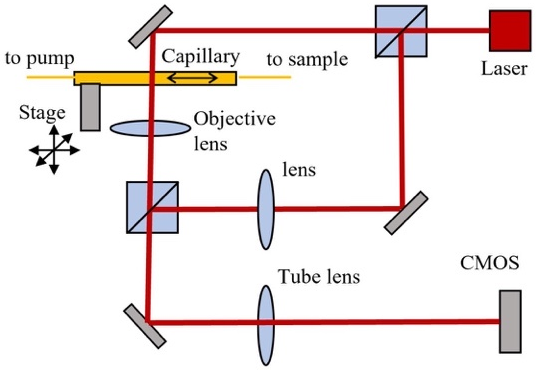

Figure 7.1. DHM Setup: laser beam (red) is split in two and recombined by two cube beam splitters, which are being directed to the CMOS; the urine is flowing in the capillary and imaged by the objective lens and tube lens on CMOS.

A laser beam with wavelength λ= 632.8 nm, 3 mW (HNL 050R, Thorlabs Inc., Newton, NJ, USA) is split in two beams by a cube beam-splitter (50/50). The first beam illuminates the sample, which is imaged by an objective lens f = 4.51 mm, NA = 0.55 (C230TME-B, Thorlabs) and the tube lens f = 200 mm (TTL200, Thorlabs) on the sCMOS sensor (CS2100M, Thorlabs) with 45× magnification. The second (reference) beam is directed through an identical lens as the objective lens and then deviated by a second beam-splitter to merge the object beam and obtain an interference pattern on the CMOS. Rotation of the second cube beam splitter allows the adjustment of the angle between the reference and object beams. This was adjusted to have an inter-fringe of about 7–8 pixels on the interference pattern, which allows a good spatial separation of the diffraction orders in the Fourier space, as required for an optimal reconstruction. A glass capillary (inner/outer diameter 0.8/1.0 mm, length 200 mm) and fluidics tubing are connected to the pump and the flow rate of the liquid in the circuit is computer controlled. The capillary position was adjusted to have the focal plane of the objective lens at about 5–7 μm from the bottom of the inner wall. A maximum volume of 1 mL liquid can be introduced in the circuit from input/output reservoirs. The liquid sample can be flowed at controlled flow rates between 10 and 100 μL/min for video recording with rates between 1 and 30 frames per second (fps) and 2 ms exposure time/frame, resulting in a holographic movie. Each video frame has 1920 × 1080 pixels, 16 bits depth/pixel. After video recording, the phase and amplitude functions are numerically reconstructed using custom Matlab code (Mathworks) and then the phase function is processed using image processing plugins Fiji (version 1.53t) [317] to facilitate bacteria localization. Brightness/contrast adjustment is applied to the phase image to help the operator localize small bright spots as region of interest (ROI). The size, shape and phase profile are then analyzed for each ROI in the original phase image to confirm the presence of bacteria within the ROI. An example of a recorded hologram (frame) and phase images obtained by numerical reconstruction are shown in Figure 7.2. One can notice the curved shape of the fringes in the hologram, due to the cylindrical beam shaping by the capillary intercepting the object beam. As background hologram in the reconstruction step, we used the median over all the frames of the holographic movie. The phase images provide useful information about the height (OPD) which allows particle identification.

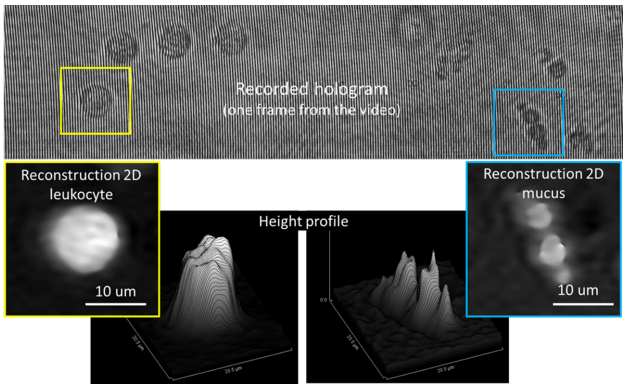

Figure 7.2 Example of recorded hologram (top image) and reconstructed phase images of a leukocyte (bottom-left yellow inset) and mucus (bottom-right blue inset) with their respective height profiles.

7.2.2. Sample Handling

The study was performed on 180 urine samples from anonymous patients, kindly provided by a regional general hospital, from 9 June to 15 September 2022. All the samples were first analyzed in the hospital microbiological laboratory by flow cytometry technique using the commercial urine particle analyzer UF-1000i instrument [304], reporting the concentrations of Bacteria (BACT), White Blood Cells (WBCs), Fungi (F), Epithelial and Squamous Cells (ESCs) [318-322].

DHM measurements were performed in the same day 3–4 h after the flow cytometry, to avoid bacterial growth in the urine samples. Before DHM analysis, each sample was plated on agar medium using a standard CPT protocol and used as a reference to evaluate the results of the other two techniques. Before loading into DHM instrument, the transparence of each sample was screened by a photo-densitometer (Densimat, Biomerieux, Marcy-l'Ètoile, France), and samples exceeding an optical density OD > 1 were discarded and analyzed separately after 1:100 dilution in physiological solution.

7.2.3. Culture Plate Test (CPT)

After homogenizing by manual mixing, 10 µL from each urine sample was streaked on a chromogenic agar plate (ChromID® CPS® Elite, REF. 418284, Biomerieux, Marcy-l'Ètoile, France) by standard loop and incubated for 18–24 h at 35 ± 2 °C. After incubation time, the bacterial colony growth on the culture plate was counted (as CFU/mL) and identified for species [323-325].

7.2.4. Measured Parameters and Evaluation Criteria

To identify and count the particles present in urine samples, we measured the size, shape, area and the optical path difference (OPD) for each potential object detected after the digital reconstruction of the optical phase function from the recorded video. Image processing for digital reconstruction, segmentation and morphological value calculation was performed using ImageJ plugins and custom Matlab code (Mathworks). The analyzed particles were BACT, WBCs, F, Red Blood Cells (RBCs), ESCs and crystals (Crys).

A urine sample was considered positive with a bacteria concentration C_BACT > 40.000 CFU/mL [324, 325]. The results obtained by UF-1000i and DHM techniques were then compared with respect to CPT positives (Pos Ref) and negatives (Neg Ref), determining the true positives (TP), true negatives (TN), false positives (FP) and false negatives (FN).

Moreover, seven evaluation parameters, sensitivity (Sens), specificity (Spec), positive predictive value (PPV), negative predictive value (NPV), true positive ratio (TPR), false positive ratio (FPR) and accuracy (ACC), were calculated as defined in Table 7.1 [326]. A deeper classification in positive

or negative was performed while also analyzing the concentration values for the other particles; cutoff in CFU/mL: WBCs (40.000), F (150.000), ESCs (30.000), RBCs (10.000), Crys (1.000) [324, 325].

Sensitivity %	TP/(TP + FN) × 100
Specificity %	TN/(TN + FP) × 100
Positive predictive value %	TP/(TP + FN) × 100
Negative predictive value %	TN/(TN + FN) × 100
True positive ratio %	TP/Pos Ref × 100
False positive ratio %	FP/Neg Ref × 100
Accuracy %	(TP + TN)/Tot × 100

Table 7.1. Evaluation parameters/metrics for positive/negative classification.

7.3. RESULTS AND DISCUSSION

7.3.1. In-Flow DHM of Microbeads in a Glass Capillary

To test the feasibility of our system to detect microparticles flowing in a glass capillary, we first used 2 μm diameter microbeads of two different materials (silica and polystyrene), which mimic the size, refractive index and density of Escherichia coli bacteria. In fact, the refractive index n = 1.384 for *E. coli* [327] is comparable with that of silica (n = 1.457 at λ = 632.8 nm, ρ = 2.22 g/cm^3) while the density ρ = 1.1 g/cm^3 is closer to polystyrene (n = 1.578, ρ =1.05 g/cm^3) [328].

Colloidal solutions of mixed microbeads in water were prepared at concentration 10^4 particles/mL. Before loading the sample with beads into the fluidic circuit, this was filled with water from the reservoir, and then a volume of 1 mL of solution was aspired from the sample vial. The beads solution was then pushed by the pump in the capillary (length 200 mm) at a flow rate of Q = 30 μL/min for 5 min to obtain a smooth laminar flow and favorize the beads settling at the bottom of the capillary. This initial step was followed by video recording at 2 fps for 3 min, with the focal plane of the objective at about 5–7 μm above the bottom of the capillary. Using the median over all the recorded holograms as a reference hologram, the amplitude and the optical phase difference (OPD) functions were reconstructed numerically (Figure 7.3). The OPD, or the phase delay, is related to the refractive index difference, dn, between the particle and the medium and the geometrical path of the light, l, through the particle [329]:

$$OPD = \frac{2\pi}{\lambda} dn \cdot l \tag{7.1}$$

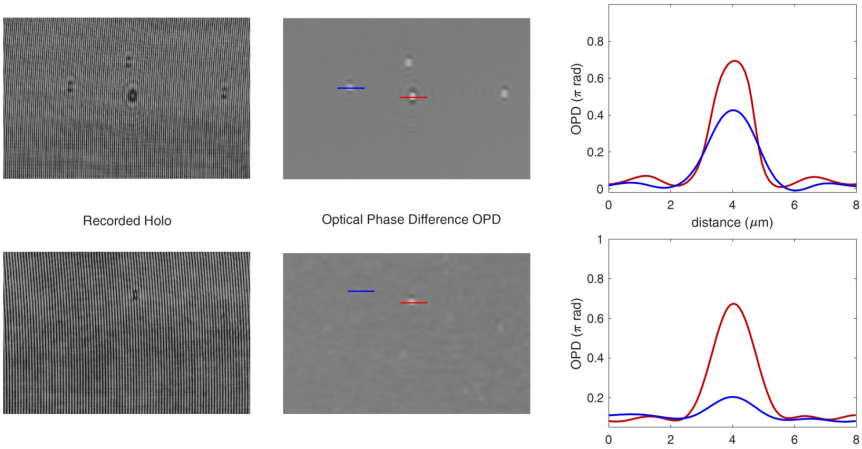

Figura 7.3. Optical phase difference (OPD) functions reconstructed numerically from recorded holograms of silica (blue) and polystyrene (red) microbeads: 2 µm polystyrene and 2 µm silica beads (top); 2 µm polystyrene and 1 µm silica beads (down).

Although both silica and polystyrene beads had the same diameter, they could still be distinguished by their refractive indexes. Thus, considering the refractive index of water, n = 1.333, the refractive index differences, dn, of silica and polystyrene beads are dn = 0.124 and dn = 0.245, respectively, producing a bigger contrast for polystyrene beads in the phase image. The OPD induced by different bead sizes was also investigated by mixing 1 µm silica and 2 µm polystyrene beads in the colloidal solution, showing that 1 µm silica beads also induce a sufficient phase shift to be detectable by their OPD (Figure 7.3).

Note that with a refractive index difference, dn = 0.051, a single *Escherichia coli* of 1 µm size induces an OPD = 0.16π [rad]. With a camera sensor with 16-bit pixel depth and using half range (2^{15} = 32768 levels) to represent the OPD, the phase image is still significative for detection of bacteria of micron and submicrometric size.

Another question is whether and how can we relate the detected particles to the colloidal solution concentration. To answer this question, we considered the distribution of the particles and related the number of detected particles to the volume of the liquid flowed during the measurement.

Since the microparticles are not uniformly distributed in the capillary volume, the probability for a particle to be found at a given height (h) from the bottom of the capillary is ruled by the Boltzmann law [291]:

$$p(h) = \frac{1}{Z} e^{-\frac{(\rho_p - \rho_m)Vh}{KT}} \tag{7.2}$$

where ρ_p and ρ_m are the mass densities of the particle and the medium, V is the particle volume, K is the Boltzmann constant, T is the temperature and Z the partition function: $Z = \sum e^{-\frac{(\rho_p - \rho_m)Vh}{KT}}$.

Since the mass density is high for silica, the particles are located mostly near the bottom of the capillary and the probability of finding them near the focal plane (h < 7 µm) is p = 0.98 for both 2 and 1 µm beads. The corresponding probabilities for the polystyrene beads, which are lighter, are p = 0.96 for beads of 2 µm diameter and p = 0.36 for beads of 1 µm diameter. These probability values indicate the volume near the bottom of the capillary as the best measurement region. If Nd is the number of particles detected during the experiment and p the probability of finding the particles in the volume investigated by the objective lens, the total number of particles Nt flowing in the capillary during the experiment will be:

$$Nt = a \cdot Nd\ /p \tag{7.3}$$

where a= [1.1–1.2] is a correction coefficient taking into account the slight perturbations of the laminar flow. This value was established empirically from experiments with beads at a known concentration. Considering the total volume (Vt) flowing in capillary during the measurement, the corresponding concentration will be:

$$C = Nt/Vt = a \cdot Nd/(p \cdot Vt) \cdot 1000 \quad (7.4)$$

in particles/mL. For instance, to have a concentration C = 10^4 particles/mL, the theoretical number of detected particles in a sample of silica beads with 2 μm (or 1 μm) diameter for a flowing volume Vt = 90 uL is Nd = 800 particles. For polystyrene particles, the number of detected particles, Nd, corresponding to a concentration C = 10^4 particles/mL will be $Nd_{2\mu m}$ = 785 and $Nd_{1\mu m}$ = 295 particles, respectively. To check the relation between the concentration, C, and the number of detected particles, Nd, we prepared ten samples of silica beads. We used 2 μm diameter beads at C = 10^4 beads/mL and measured the corresponding Nd for a volume Vt = 90 uL flowing in 3 min, obtaining a mean/std value of Nd_{mean} = 772/65, which is in agreement with the theoretical expected value. There were about 2.14 beads counted, in average, for each of the 360 recorded frames in the holographic video. These results indicate that our technique can be applied to detect concentrations from 10^3 to 10^5 particles/mL, allowing a good discrimination, at least of one order of magnitude in concentration.

To apply the technique to bacteria cells we must consider that the mass density of bacteria is higher than polystyrene, ρ = 1.1 g/cm^3, and hence the probability of finding 1 μm size bacteria at height h < 7 μm is also higher, p = 0.59.

7.3.2. In-Flow DHM of Urine Sample in a Glass Capillary

Urine samples from patients were handled as described in the "Material and Methods" section. The fluidic circuit was first filled with milliQ water and then the urine sample was loaded by aspiration from the output. A volume of 1 mL was aspired in the pump reservoir and then pushed towards the output at a rate of 30 μL/min for 5 min for flow stabilization, followed by another 3 min for recording. A holographic video was recorded at 2 fps, resulting in a holographic movie of 360 frames for each sample. The OPD was then calculated from a hologram reconstruction. Examples of OPDs obtained for various elements that could be found in different urine samples can be observed in Figure 7.4. A Streptococcus spp chain is shown together with a white blood cell in Figure 7.4a, an Escherichia coli together with a red blood cell in Figure 7.4b, a macrophage in Figure 7.4c and an epithelial (squamous) cell is reported in Figure 7.4d. In addition, a red blood cell together with a spermatozoa cell are shown in Figure 7.4e, fungi in Figure 7.4f and a crystal in Figure 7.4g. As one can see, the phase image provides 2D morphological information and an image, but also relevant information on the height and refractive index which can be used to identify the cell. In fact, the gray levels in the images represent the OPD values, in radian. For bacteria and almost all the other cells OPD < 2π rad. For bigger cells or larger refractive index variations, OPD > 2π rad, and the color jumps from white to black (macrophage and crystal). To obtain the real OPD values in these cases, a phase unwrapping procedure is required. However, since the full reconstruction of these types of objects did not affect our analysis, we did not proceed with unwrapping the OPD function.

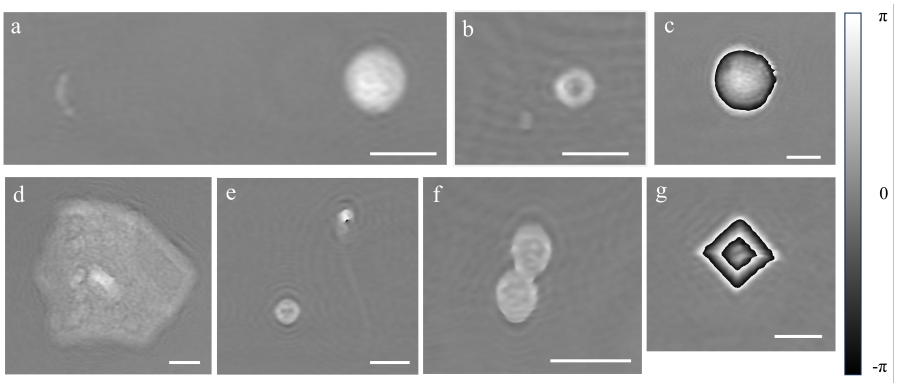

Figure 7.4. Examples of phase images for different components of the urine samples: (a) Streptococcus spp. chain (left) and leukocyte (right), (b) Escherichia coli (left) and red blood cell (right), (c) macrophage cell, (d) epithelial (squamous) cell, (e) red blood cell (down-left) and spermatozoa cell (up-right), (f) fungi and (g) crystal. Scale bar 10 µm.

7.3.3. Bacteriuria Detection and Samples Classification into Positives or Negatives

To test our in-flow DHM technique for detection of bacteria and sample classification, we analyzed 180 fresh urine samples as described in the "Materials and Methods" section. We recorded and reconstructed the holographic movies for each sample as described in the previous section. Then, we processed the OPD function for each sample for the 360 frames/sample containing the phase images. Contrast adjustment followed by shape and size evaluation of the particles in the visual field was used to select bacteria cells and their positions. The presence of bacteria was then confirmed by evaluating the value of the OPD at the respective locations. An OPD value in the range [0.08 π–0.32 π] rad was used to confirm the presence of bacteria. The bacteria were counted in each frame and those bacteria presented in more than one frame were subtracted from the total to obtain the detected number (*Nd*). Following the rationale described in Section 7.3.1, we used the probability value $p = 0.59$ in Equation (7.3) to find the total number of bacteria cells *Nt*. For the other cells (WBCs, RBCs, ESCs) we used a higher probability value $p = 0.88$, as derived from the Boltzmann distribution law. Then the concentration was calculated according to Equation (7.4).

The cutoff value for positive/negative samples was 40.000 CFU/mL [324, 325]. With this criterion we detected 133 (73.89%) positive (POS) samples and 47 (26.11%) negative (NEG) samples using the DHM technique. Flow cytometry with UF-1000i found 114 (64.41%) POS and 61 (34.46%) NEG, while the CPT reported 91 (50.56%) POS and 89 (49.44%) NEG (Table 7.2a, first row). These results show that both DHM and UF-1000i found more POS and less NEG than the CPT.

(a)

White row: 180 samples in total, considering bacteriuria

Green row: 169 samples in total, considering bacteriuria (11 samples excluded)

Blue row: 169 samples in total, considering bacteriuria, WBCs, F and ESCs

*: Only 175 of 180 are considered because UF1000i reports were missing for 5 samples.

	DHM			**UF-1000i ***			**CPT**		
Number	POS	NEG	**TOT**	POS	NEG	**TOT**	POS	NEG	**TOT**
of	133	47	**180**	114	61	**175 ***	91	89	**180**
samples	122	47	**169**	103	61	**164**	91	78	**169**
	110	59	**169**						

(b)								
	DHM vs. CPT				UF-1000i vs. CPT			
Number	TP	TN	FP	FN	TP	TN	FP	FN
of	82	38	51	9	79	52	35	9
samples	82	38	40	9	79	52	24	9
	80	48	30	11				

(c)					
%	**DHM vs. CPT**			**UF-1000i vs. CPT**	
Sensitivity	90.11	90.00	**87.91**	89.77	**89.66**
Specificity	42.70	48.10	**61.54**	59.77	**67.53**
Positive Predictive Value	61.65	66.39	**72.73**	69.30	**75.73**
Negative Predictive Value	80.85	80.85	**81.36**	85.25	**85.25**
True Positive Ratio	90.11	90.00	**87.91**	86.81	**86.67**
False Positive Ratio	57.30	51.90	**38.46**	39.33	**31.65**
Accuracy	66.67	70.41	**75.74**	74.86	**78.78**

Table 7.2. Results of the analysis for N = 180 samples measured by DHM, UF-1000i and CPT. (a) Positives and negatives as reported by DHM, UF-1000i and CPT. (b) True positives (TP), true negatives (TN), false positives (FP), false negatives (FN) for DHM and UF-1000i considering CPT as reference. (c) Evaluation parameters in %.

Comparing the results obtained by all three techniques, we found a set of 11 samples which were indicated as NEG by CPT but were found POS both by DHM and UF-1000i, i.e., they were false positives for both techniques when compared to CPT. This situation might be explained by a possible antibiotic treatment used by the patients, which inhibits bacteria proliferation and hence the urine sample results as NEG in CPT. Therefore, we also ran the analysis on the pool of data after removing these 11 samples (Table 7.2a, second row). Taking CPT as reference we calculated the TP, TN, FP and FN for DHM and UF-1000i (Table 7.2b, first two rows). The percentage of TP and FN for DHM and UF-1000i compared to CPT are similar, while DHM found significantly more FP than UF-1000i. Calculating the sensitivity, specificity and the other five parameters defined in Section 7.2.4, we found similar values for DHM and UF-1000i when compared to CPT, excepting the specificity and false positive ratio, for which the differences were bigger (Table 7.2c, first columns).

To evaluate the importance of the presence of other cells in urine, we selected the samples found in the critical range of positivity for bacteriuria, as measured by DHM: $4 \times 10^4 < C\_BACT < 6 \times 10^4$ CFU/mL. Thus, we found 17 samples in this range and for each of them we analyzed the concentrations of WBCs, ESCs and F cells. The positivity of the urine sample was confirmed if at least one of the concentration values was within conventional positivity values: $C\_WBCs > 4 \times 10^4$ cells/mL, $C\_ESCs > 3 \times 10^4$ cells/mL, $C\_F > 15 \times 10^4$ CFU/mL [324, 325]. Following this criterion, the positives and negatives for DHM changed from 17 positives and 0 negatives to 5 positives and 12 negatives (Table 7.2a,b, blue rows). For positives, the number of TP was reduced by 2, while FP was strongly reduced, by 10. For negatives, the number of TN was much increased (by 10) while the FN also slightly increased (by 2). This led to a clear improvement of the values of DHM evaluation parameters compared to CPT (Table 7.2c, blue column) better approaching the UF-1000i results.

Although the values for the NPV and the TPR (two parameters of most interest when trying to sort out the negative samples) are high (>80%), both methods (DHM and UF-1000i compared to CPT) require further optimization. Moreover, although the FPR is relatively low (<40%), it is still far from

the desirable value (<20%) [323] and hence further optimization or cross-checking of the results with other methods are necessary when using DHM or UF-1000i. Investigating a bigger sample volume might enhance the DHM performance, with the cost of the additional time requested for measurement.

DHM also provided information on the presence of RBCs, salt/crystals and the type of epithelial cells (cylinders, squamous) in the urine samples. For instance, among the 17 samples selected above there were five samples with a concentration of RBCs, C_RBCs > 10^4 cells/mL. Although RBCs concentration cannot be correlated with infection (in fact only 1 out of 5 samples was found as FP by DHM vs. CPT), a high concentration of C_RBCs might indicate a pathological case, hence providing useful information for clinicians. In addition to RBCs presence, three samples were detected with a salt/crystal concentration of C_Crys > 10^3 particles/mL, which was considered critical. However, only one of these samples was classified as positive, while the other two were negative. Interestingly, although in one of the two negative samples the concentration of crystals and RBCs were 8×10^4 particles/mL and 1.1×10^4 cells/mL, respectively, the sample was found negative by all the three techniques (CPT, UF-1000i and DHM) from the bacteriuria point of view. As with the RBCs, the presence of a high number of salts/crystals cannot be correlated with infection but it might indicate improper function of the urinary system.

7.4. CONCLUSIONS

In the present study, we proposed a new application of DHM to analyze urine samples flowing in a capillary. The measurement was performed in 3 min, flowing the sample at 30 µL/min and acquiring holograms at 2 fps. The reconstruction of the holographic movie allowed us to obtain the phase function (optical path difference, OPD) which, together with the size and shape of the particles, provided the necessary information to detect bacteria and other cells such as WBCs, RBCs, spermatozoa, epithelial cells and sediments such as crystals and fungi.

To evaluate the performance of DHM as an inspection technique, we performed a screening test on 180 human urine samples and compared the results with those obtained by the standard culture plate test. Moreover, flow cytometry tests were performed on the analyzed samples in the same day by the microbiology laboratory in hospital. The results obtained by DHM and flow cytometry were similar when compared with the CPT, indicating DHM as a simple and fast technique for a preliminary screening of the urine samples.

Better values of the evaluation parameters, compared to CPT, were obtained for DHM by analyzing the presence of other cells in the urine samples at the border of the bacteriuria cutoff, demonstrating the usefulness of the additional information provided by the phase images of the urine components.

The DHM technique is commonly known as a label-free technique, providing an important advantage over the other two techniques: the phase images of all the particles flowing in the field of view are digitally recorded and can be archived and shared for further consultation by different clinicians.

8 FINAL CONCLUSIONS AND FUTURE PROSPECTS

Mechanobiology is an emerging field in which competences coming from engineering, physics and material science integrate the biological ones for a full description of mechanical properties of cell and tissues. In the aim of mechanical characterization of cells, both imaging and probing devices had been developed. Each of these own peculiar strengths and allow the measurement of different parameters. However, for accessing multiple information on single cells the combination of more than one technique is required. In this way, synergic and significant results can be obtained.

Within the Thesis a successful combination of tools had been adopted for validating qualitative information provided by QCM with quantitative analysis from DHM. In addition, fluorescence visualization of cellular elements allowed to appreciate actin and tubulin network evolvement during treatment with specific drugs. With this approach we highlighted the pivotal role of actin in maintaining shape integrity, adhesion stability, and mechanical structure of primary cardiac fibroblasts with a particular focus at the cell-substrate interface.

Complementary to this investigation, it would be interesting to investigate also the contribution of intermediate filaments, such as vimentin, to viscoelastic and adhesive properties of fibroblasts by using this approach. Even if vimentin has a marginal role in mechanical properties maintenance this technique could be exploited for describing the cell-interface behavior when these structures are selectively disrupted.

Secondly, a multimodal approach consisting in the synergic application of OT and AFM coupled to fluorescent calcium imaging allowed to explore a broad range of physiological pressures. This showed that local forces in the nanonewton range, accessible with AFM, are better suitable for studying calcium gating in cardiac fibroblasts. Moreover, the investigation was enriched by the modulation of substrates stiffness which allowed to describe how the microenvironment can regulate the mechanosensitive response to local stimulation. This work demonstrated the main role of Piezo1 in regulating microenvironment-mediated fibroblasts mechanosensitivity which in turn suggests its important role in cardiac fibrotic mechanisms.

As future prospects, it would be interesting to investigate if changing the geometry of the probe could unveil new features about channel functionality. For example, for achieving the same pressure a larger probe requires a higher force, on the contrary a smaller surface area needs lower forces. However, in the work presented here the probe was maintained the same and only forces were modulated. It is still unknown if, by applying the same pressure, a higher membrane curvature change induced by a smaller probe can locally favor channel aperture or if the absolute pressure value is the solely responsible for channel triggering instead.

In a third experimental approach, a novel methodology enclosing micropipette aspiration with multimodal imaging (bright field and fluorescence) was proposed as a suitable tool for accessing both cells mechanical properties and mechanosensitive ion channels functionality. In particular, we investigated how RBCs storing time can influence mechanical properties and Piezo1 channel activity and found that both of them result changed showing channel alteration preceding the mechanical property variations. The advantage of accessing simultaneously all the information represents the key for investigating the relationship between mechanical properties and Piezo1 functionality.

In this regard, we believe that prolonged storing time could further affect both Piezo1 and cell mechanical properties. However, maintaining cells outside the physiological condition is linked to several uncontrollable variables which could induce us to misinterpret the obtained results. For this reason, accelerating the mechanical properties alteration by treating cells with drugs able to alter

spectrin mesh and/or membrane properties would allow us to assess with larger reliability the relationship between mechanical parameters and Piezo1 function.

In the last application, a DHM-based method has been validated as a fast alternative to urine sample screening. In this case the multiplexity of information accessible with DHM exceeds the limitations related to the gold standards (CPT and flow cytometry). It allows, in fact, a full description of urine-containing particles that goes beyond a simple bacteriological screening but can be used also for other investigations by different clinicians.

In conclusion, the Thesis aim to highlight the advantages of multimodal approaches proposing novel methodologies coming from smart coupling of well-known tools. The results obtained here could be well extend to human cells from pathological donors in order to carry on experiments in conditions closer to the pathophysiological ones.

For example, instead of using chemical drugs for cytoskeletal elements disruption, testing human cells could be the next step. In fact, using cells directly from donors affected by some diseases known for owning cell cytoskeletal alterations would allow their mechanical properties characterization in the prospect of the development of new diagnostic techniques based on biomechanical markers.

Analogously, instead of mimicking the mechanical pathological conditions of the environment for inducing fibroblasts transdifferentiation, human cells from explanted hearts could be used for investigating mechanosensitivity with a focus closer to the physiological condition.

At the same time, also RBCs from donors affected by pathologies involving Piezo1 mutations, could be investigated by using our proposed method for acquiring information on channel dysfunctionality and unveil if this is also associated to mechanical property alterations. Due to the easily way in which RBCs can be isolated from both healthy and unhealthy humans, I believe that there are good chances for achieving new diagnostic protocols and techniques within the immediate next future in this context.

Although the last experimental approach proposed here had already overcame the initial optimization step through artificial injection of cultured bacteria allowing us to already test and validate the technique on hospitalized human urine samples, it represents a good starting point for new clinical perspectives. In fact, based on the entity of information accessible, it may be considered as a new valid diagnostic tool for screening not only bacteriological urinary tract infections but also other pathologies for which biomarkers could be found in urine.

Moreover, the proposed methods are not limited to the cells investigated here but can be well extended to other cells types and purposes.

Therefore, it is believed that these approaches, and main results discussed here, may unveil new investigative research fields and contribute to the development of new diagnostic tools and targeted therapies.

APPENDIX I

This section provides below supplementary figures related to results presented in Chapter 5.

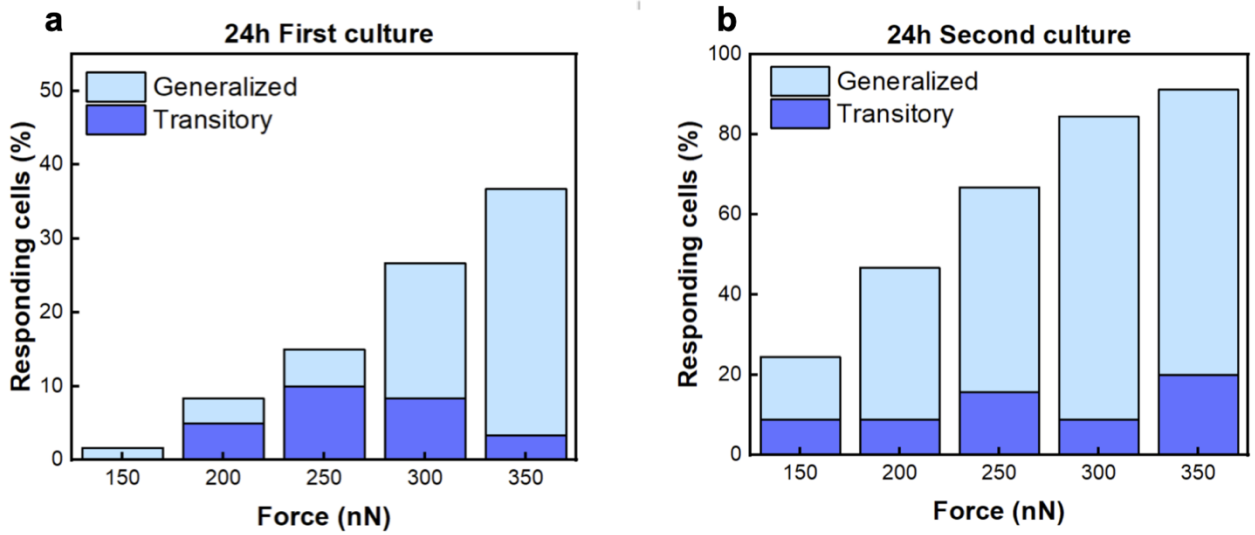

Figure AI.1. Force-dependent cell responses for the two distinct cultures. 60 cells were investigated for the first culture (a) and 45 cells for the second culture (b) after 24 h plating.

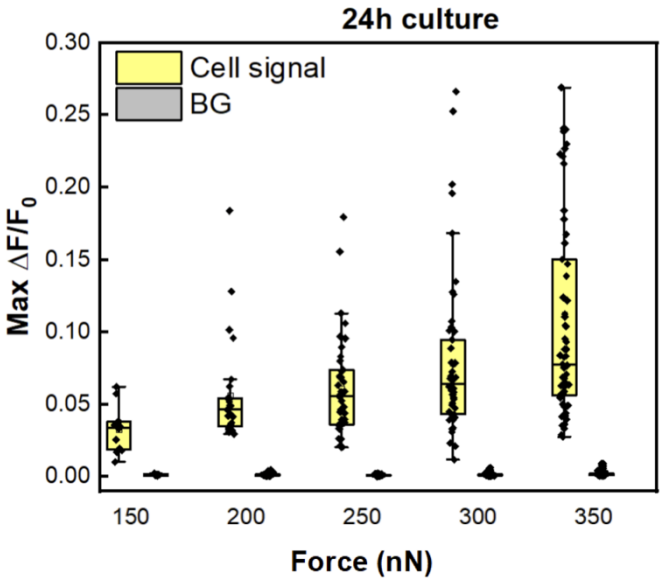

Figure AI.2. Distribution of $\Delta F/F_0$ values for all responding cells cultured for 24 hours and stimulated with forces from 150 nN to 350 nN, (N=105). BG refers to the $\Delta F/F_0$ values for each background in each responding cell and shows its negligibility respect to the cell response.

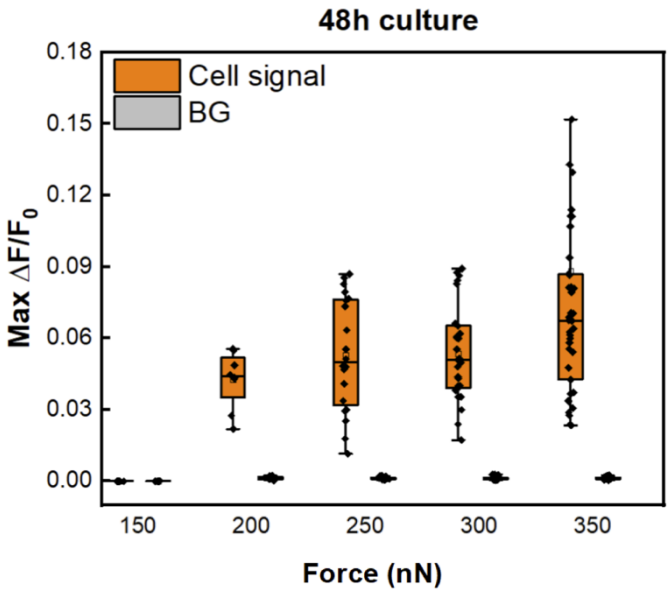

Figure AI.3. Distribution of $\Delta F/F_0$ values for all responding cells cultured for 48 hours and stimulated with forces from 150 nN to 350 nN, (n=45). BG refers to the $\Delta F/F_0$ values for each background in each responding cell and shows its negligibility respect to the cell response.

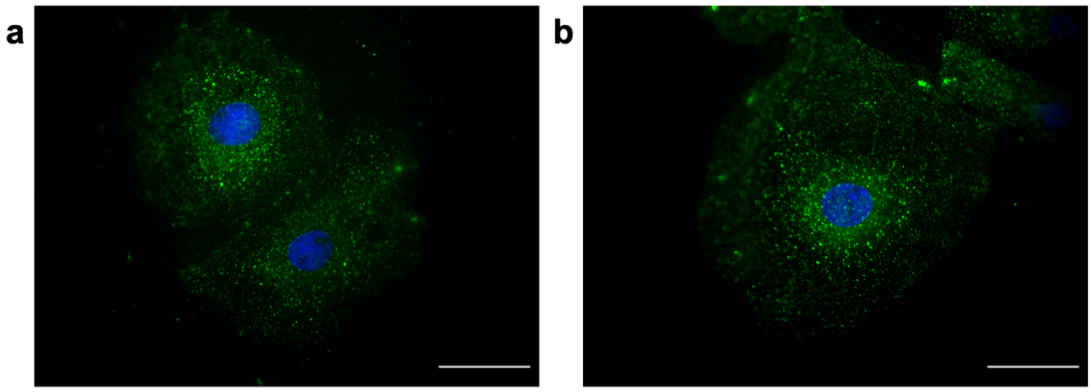

Figure AI.4. No detectable differences were observed in transmembrane Piezo1 between 24 (a) and 48 (b) hours cultured cells. Scale bar: 40μm.

APPENDIX II

As anticipated in Chapter 5, in order to investigate the mechanosensitive adaptation of primary cardiac fibroblasts to soft cultures, polyacrylamide (PA) hydrogels were first selected based on the wide use reported in literature [87-89]. However, due to several encountered problems the results obtained were not included into the submitted work. This Section is dedicated to the description of protocols adopted for substrates fabrication, functionalization, as well as the presentation of preliminary results obtained.

Thanks to the support of Professor Pierangelo Gobbo's group at the Department of Chemical and Pharmaceutical Sciences, the procedure for substrates fabrication was optimized.

Once optimized the substrates fabrication procedure by tuning the acrylamide concentration for achieving three different stiffness, the main problems encountered were relative to cell culture. It is known from literature that PA does not allow direct cell or proteins attachment, as discussed in Chapter 1, Section 1.7.1; however, when we tried to replicate published protocols for substrates functionalization we found some missing information. The widely used method consists in activating the PA surface with the Sulfo-SANPAH, as discussed in the Chapter 1. However, particular attention needs to be conferred to the following steps:

1. glasses washing solution and sulfo-SANPAH buffer should be a non-amine-containing buffers at pH of 7-9;

2. concentration of sulfo-SANPAH needs to be optimize in order to achieve enough proteins attachment and avoid sulfo-SANPAH wasting due to its high cost. The concentration reported in literature ranges from 0.2 to 2 mg/mL [95, 98, 103, 330, 331].

3. photolysis should be performed by using UV lamps that irradiates at 300-460nm

4. the distance of the sample to the lamp should be optimized based on wavelength and exposure time.

5. prolonged waiting time during sulfo-SANPAH irradiation leads to its evaporation and hydrogel drying ultimately promoting a damaged surface appearing squamous.

The lacking of precise protocols covering all these aspects led me to experiment personally a lot of problems in achieving successful substrate functionalization and cell culture. Several attempts in solving encountered problems have been made proceeding by trial and error. All of these will not be discussed singularly here but the final protocol obtained, which allowed successful cell culture, is detailed reported below. It is believed that the described protocol can be faithfully reproduced by any another user without the need of further information and with the same guaranteed successful.

AII.1. PA SUBSTRATES PRODUCTION

PA substrates were produced on glass coverslip (18 mm diameter). Glasses placed in multiwall were first washed in MilliQ water and sonicated for 5 minutes. They were then dipped in NaOH 0.1 M and sonicated for 15 minutes, followed by 15 minutes immersion in silane solution composed by 1% of acetic acid, 2% of 3-(Trimethoxysilyl)propyl methacrylate (M6514, Sigma Aldrich) and 97% ethanol. Thereafter, glasses were dipped in methanol for 5 minutes, washed in MilliQ water, and finally they were let to dry.

PA substrates were produced in the following w/v acrylamide ratios: 7.5 %, 10%, 15%.

Acrylamide (01700-250G, Sigma Aldrich) powder was mixed with N,N′-Methylenediacrylamide (805968, Sigma Aldrich) and solubilized in MilliQ water. Monomer

solutions were dropped on parafilm and in the same drop the catalysator and initiator were added. Ammonium persulfate (APS) (248614-100G, Sigma Aldrich) was prepared at 10% w/v solution in MilliQ water and added in 1.1 molar ratio respect to acrylamide while N,N,N',N'-tetramethylethylenediamine (TEMED), (T22500-100ML, Sigma Aldrich) was added at 5 molar ratio. Rapidly, the glasses were placed on the drop with the silanized face down and the hydrogels were let to polymerize for at least 30 minutes before being dipped in MilliQ water and placed again in the multiwall.

AII.2. PA SUBSTRATES FUNCTIONALIZATION

For PA functionalization, substrates were first washed in Hepes 50 mM and then incubated in Sulfo-SANPAH (A35395, Thermofisher). Sulfo-SANPAH stock solutions were prepared in DMSO at 5 mg/mL and flash freeze in liquid nitrogen; the final working solution was performed by diluting the working solution in Hepes 50 mM to 0.4 mg/mL. Glasses with Sulfo-SANPAH were UV (365 nm) irradiated for 20 minutes at a distance of 6 cm from the light source at 50 W power. This step was performed in multiwall without the lid on the top.

At the end, the lid of the multiwall was then rapidly put on and from this point on the procedure was performed in biological hood. Glasses were washed three times in Hepes 50 mM and then incubated with fibronectin. Fibronectin (F4759, Sigma Aldrich) stock solution was obtained by dilution at 1 mg/mL in water. Thereafter, this was diluted at 20 μg/mL in PBS 1X to obtain the working solution in which the hydrogels were incubated at room temperature for 30 minutes. PA substrates were then washed with PBS 1X and cells were seeded.

AII.3. YOUNG'S MODULUS MEASUREMENT OF PA

Measuring the Young's Modulus with AFM resulted almost impossible due to the severe attachment of the cantilever to the substrates. However, Prof. Gobbo and collaborators have acquired successful experience in measuring mechanical properties of hydrogels and had recently published a new method for soft materials characterization [332]. The microindenter device FT-MTA03 from FemtoTools AG described in their work was used to measure PA hydrogels. The instrument was equipped with an FT-S2000 Microforce Sensing Probe and working with a spherical tip of 50 μm radius which was obtained by attaching borosilicate glass microspheres to the silicon probe with Norland Optical Adhesive 81 and curing with a 365 nm UV LED (Thorlabs, Inc.). Measurement were performed at a speed of 10 μm/s. The Young's Modulus was evaluated by using a custom approach consisting in a python-based application called "ALIAS" and discussed within the work. The results of elastic measurements are following reported in Figure AII.1.

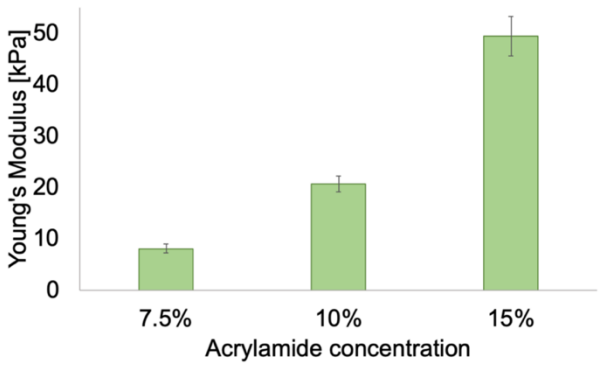

	Mean	St.Dev
7.5%	8.1	0.8
10%	20.7	1.5
15%	49.5	3.8

Figure AII.1. Young's Moduli relative to substrates produced by using 7.5, 10 and 15 % of acrylamide.

AII.4. RESULTS BY USING PA HYDROGELS

Once optimized the protocol for cell attachment, culturing cells on such substrates resulted pretty complicated. Maybe due to their primary nature, cells were visible suffering in culture on PA hydrogels, with only an apparent better aspect on the stiffer substrates. In this last case, cells were able to replicate; however, when they were incubated with Fluo8 for preforming mechanical stimulation and calcium imaging they mostly underwent death. Therefore, the results obtained with such compromised cell were not considered.

For comparing our fabricated substrates with commercial ones, cells were grown on PA hydrogels supplied by Matrigen. 12 well-plates with Softslip™ with the following stiffness: 4, 25 and 50 kPa and coated with collagen (Softslip, SS12-COL-4 EA, SS12-COL-25 EA, SS12-COL-50 EA, Matrigen, Brea, CA, USA) were used.

With respect to self-fabricated substrates, only limited improvement was noticed with commercial ones. At lower stiffness conditions (4 and 25 kPa) cells continued to be characterized by a very low cell attachment as well as an almost absent proliferation. On the stiffer substrate (50 kPa) cells were able to grow and replicate but, when incubated with calcium dye, they once again demonstrated their suffering condition by undergoing death.

Some stimulation experiments were performed only on cells looking healthy but no mechanical responses were observed. Moreover, from Yoda1 stimulation we observed comparable response to that observed with PDMS, as shown in Figure AII.2.

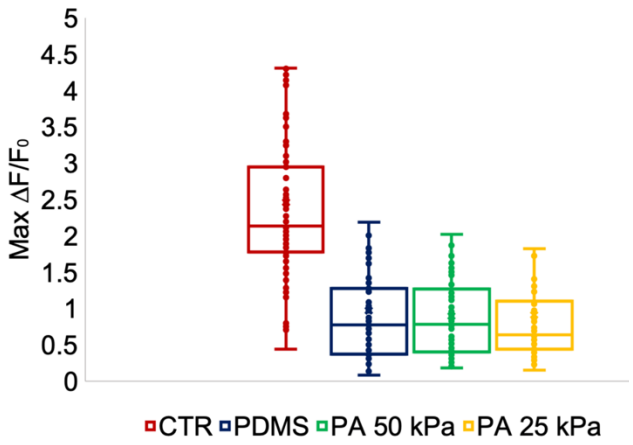

Figure AII.2. $\Delta F/F_0$ values for cells responding to Yoda1 stimulation for control (CTR), PDMS and PA hydrogels with 50 and 25 kPa stiffness.

In the Figure AII.2, results on 4 kPa are not displayed due to the high percentage of dead cells and detachment from the substrates after the Yoda1 injection. This easily detachment from the surface was also assessed in 50 kPa and 25 kPa substrates and this is the reason why these results were not included in the work.

Despite these data need to be managed with caution because of cells condition, they may suggest that PDMS should be the best solution for *in vitro* investigating the cardiac fibroblasts mechanosensitive modulation mediated by the mechanics of the microenvironment.

Even if the PDMS stiffness is well above the physiological condition, it is important to highlight that, as cells are isolated from the native tissue, every tentative in maintaining a "physiological" condition will fail. Cells in culture are pretty far from their physiological environment and therefore substrates stiffnesses which match the native tissue mechanical properties could not satisfy the *in vitro* cells'

requirements. This could be the reason underling the cell suffering observed in both self-fabricated and commercial PA substrates characterized by low stiffness.

BIBLIOGRAPHY

1. Schwarz, U.S., *Mechanobiology by the numbers: a close relationship between biology and physics.* Nature Reviews Molecular Cell Biology, 2017. **18**(12): p. 711-712.
2. Nakanishi, J. and K. Uto, *An Introduction to Material-based Mechanobiology*, in *Material-based Mechanobiology*, J. Nakanishi and K. Uto, Editors. 2022, The Royal Society of Chemistry. p. 0.
3. Janmey, P.A., D.A. Fletcher, and C.A. Reinhart-King, *Stiffness Sensing by Cells.* Physiological Reviews, 2019. **100**(2): p. 695-724.
4. Alasfar, R.H., et al. *A Review on the Modeling of the Elastic Modulus and Yield Stress of Polymers and Polymer Nanocomposites: Effect of Temperature, Loading Rate and Porosity*. Polymers, 2022. **14**, DOI: 10.3390/polym14030360.
5. Ashby, M.F., *Materials Selection in Mechanical Design*. 2016: Elsevier Science.
6. Smith, W.F., et al., *Scienza e tecnologia dei materiali*. Collana di istruzione scientifica. Serie di ingegneria meccanica. 2012: McGraw-Hill Education.
7. Banks, H.T., S. Hu, and Z.R. Kenz, *A Brief Review of Elasticity and Viscoelasticity for Solids.* Advances in Applied Mathematics and Mechanics, 2011. **3**(1): p. 1-51.
8. Noirez, L., P. Baroni, and H. Mendil-Jakani, *The missing parameter in rheology: hidden solid-like correlations in viscous liquids, polymer melts and glass formers.* Polymer International, 2009. **58**(8): p. 962-968.
9. Münstedt, H. *Rheological Measurements and Structural Analysis of Polymeric Materials*. Polymers, 2021. **13**, DOI: 10.3390/polym13071123.
10. Sharma, P., et al., *A Review on Dynamic Rheology for Polymers.* International Journal of Applied Engineering Research, 2018. **13**(6): p. 363-368.
11. Surya Nagendra, P., V.V.S. Prasad, and K. Ramji, *A Study on Dynamic Mechanical Analysis of Natural Nano Banana Particle Filled Polymer Matrix Composites.* Materials Today: Proceedings, 2017. **4**(8): p. 9081-9086.
12. Fazeli, M., et al., *Experimental analyzing the effect of n-heptane concentration and angular frequency on the viscoelastic behavior of crude oil containing asphaltene.* Scientific Reports, 2022. **12**(1): p. 3965.
13. Meyers, M.A., et al., *Biological materials: Structure and mechanical properties.* Progress in Materials Science, 2008. **53**(1): p. 1-206.
14. Carotenuto, F., et al. *From Soft to Hard Biomimetic Materials: Tuning Micro/Nano-Architecture of Scaffolds for Tissue Regeneration*. Micromachines, 2022. **13**, DOI: 10.3390/mi13050780.
15. Akhtar, R., et al., *Characterizing the elastic properties of tissues.* Materials Today, 2011. **14**(3): p. 96-105.
16. Chen, X., et al., *A Feedforward Mechanism Mediated by Mechanosensitive Ion Channel PIEZO1 and Tissue Mechanics Promotes Glioma Aggression.* Neuron, 2018. **100**.
17. Raczkowska, J. and B. Orzechowska, *Effect of tuned elasticity and chemical modification of substrate on fibrotic and healthy lung fibroblasts.* Micron, 2020. **139**: p. 102948.
18. Freeberg, M.A.T., et al., *Mechanical Feed-Forward Loops Contribute to Idiopathic Pulmonary Fibrosis.* The American Journal of Pathology, 2021. **191**(1): p. 18-25.
19. Fu, Y., et al., *Targeting Mechanosensitive Piezo1 Alleviated Renal Fibrosis Through p38MAPK-YAP Pathway.* Frontiers in Cell and Developmental Biology, 2021. **9**.
20. Mueller, S. and L. Sandrin, *Liver stiffness: a novel parameter for the diagnosis of liver disease.* Hepatic medicine : evidence and research, 2010. **2**: p. 49-67.
21. Herum, K.M., et al., *The Soft- and Hard-Heartedness of Cardiac Fibroblasts: Mechanotransduction Signaling Pathways in Fibrosis of the Heart.* Journal of Clinical Medicine, 2017. **6**(5).

22. Weiskirchen, R., S. Weiskirchen, and F. Tacke, *Organ and tissue fibrosis: Molecular signals, cellular mechanisms and translational implications.* Molecular Aspects of Medicine, 2019. **65**: p. 2-15.
23. Kasza, K.E., et al., *The cell as a material.* Current Opinion in Cell Biology, 2007. **19**(1): p. 101-107.
24. Hao, Y., et al., *Mechanical properties of single cells: Measurement methods and applications.* Biotechnology Advances, 2020. **45**: p. 107648.
25. Pogoda, K., et al., *Depth-sensing analysis of cytoskeleton organization based on AFM data.* European Biophysics Journal, 2012. **41**(1): p. 79-87.
26. Schepers, A.V., et al., *Multiscale mechanics and temporal evolution of vimentin intermediate filament networks.* Proceedings of the National Academy of Sciences, 2021. **118**(27): p. e2102026118.
27. Janmey, P.A., et al., *Viscoelastic properties of vimentin compared with other filamentous biopolymer networks.* Journal of Cell Biology, 1991. **113**(1): p. 155-160.
28. Rottner, K., et al., *Actin assembly mechanisms at a glance.* Journal of Cell Science, 2017. **130**(20): p. 3427-3435.
29. Chen, M., et al., *Effect of F-Actin Organization in Lamellipodium on Viscoelasticity and Migration of Huh-7 Cells Under pH Microenvironments Using AM-FM Atomic Force Microscopy.* Frontiers in Physics, 2021. **9**.
30. Damania, D., et al., *Role of cytoskeleton in controlling the disorder strength of cellular nanoscale architecture.* Biophysical journal, 2010. **99**(3): p. 989-996.
31. Kopelovich, L., S. Conlon, and R. Pollack, *Defective organization of actin in cultured skin fibroblasts from patients with inherited adenocarcinoma.* Proceedings of the National Academy of Sciences, 1977. **74**(7): p. 3019-3022.
32. Rao, J.Y., et al., *Quantitative changes in cytoskeletal and nuclear actins during cellular transformation.* International Journal of Cancer, 1997. **70**(4): p. 423-429.
33. Marian, A.J., B. Asatryan, and X.H.T. Wehrens, *Genetic basis and molecular biology of cardiac arrhythmias in cardiomyopathies.* Cardiovascular Research, 2020. **116**(9): p. 1600-1619.
34. Ehler, E., *Actin-associated proteins and cardiomyopathy—the 'unknown' beyond troponin and tropomyosin.* Biophysical Reviews, 2018. **10**(4): p. 1121-1128.
35. Fallqvist, B., et al., *Experimental and computational assessment of F-actin influence in regulating cellular stiffness and relaxation behaviour of fibroblasts.* Journal of the Mechanical Behavior of Biomedical Materials, 2016. **59**: p. 168-184.
36. Roca-Cusachs, P., T. Iskratsch, and M.P. Sheetz, *Finding the weakest link – exploring integrin-mediated mechanical molecular pathways.* Journal of Cell Science, 2012. **125**(13): p. 3025-3038.
37. Garoffolo, G. and M. Pesce *Mechanotransduction in the Cardiovascular System: From Developmental Origins to Homeostasis and Pathology*. Cells, 2019. **8**, DOI: 10.3390/cells8121607.
38. Huang, H., R.D. Kamm, and R.T. Lee, *Cell mechanics and mechanotransduction: pathways, probes, and physiology.* American Journal of Physiology-Cell Physiology, 2004. **287**(1): p. C1-C11.
39. Liu, X. and F. Nakamura, *Mechanotransduction, nanotechnology, and nanomedicine.* Journal of biomedical research, 2020. **35**(4): p. 284-293.
40. Jaalouk, D.E. and J. Lammerding, *Mechanotransduction gone awry.* Nature Reviews Molecular Cell Biology, 2009. **10**(1): p. 63-73.
41. Kanoldt, V., L. Fischer, and C. Grashoff, *Unforgettable force – crosstalk and memory of mechanosensitive structures.* Biological Chemistry, 2019. **400**(6): p. 687-698.
42. Bershadsky, A.D., et al., *Assembly and mechanosensory function of focal adhesions: experiments and models.* European Journal of Cell Biology, 2006. **85**(3): p. 165-173.

43. Seong, J., N. Wang, and Y. Wang, *Mechanotransduction at focal adhesions: from physiology to cancer development.* Journal of cellular and molecular medicine, 2013. **17**(5): p. 597-604.
44. Jin, P., L.Y. Jan, and Y.-N. Jan, *Mechanosensitive Ion Channels: Structural Features Relevant to Mechanotransduction Mechanisms.* Annual Review of Neuroscience, 2020. **43**(1): p. 207-229.
45. Nourse, J.L. and M.M. Pathak, *How cells channel their stress: Interplay between Piezo1 and the cytoskeleton.* Seminars in Cell & Developmental Biology, 2017. **71**: p. 3-12.
46. Jiang, Y., et al., *Structural Designs and Mechanogating Mechanisms of the Mechanosensitive Piezo Channels.* Trends in Biochemical Sciences, 2021. **46**(6): p. 472-488.
47. Martinac, B., *Mechanosensitive ion channels: molecules of mechanotransduction.* Journal of Cell Science, 2004. **117**(12): p. 2449-2460.
48. Cox, C.D., et al., *Removal of the mechanoprotective influence of the cytoskeleton reveals PIEZO1 is gated by bilayer tension.* Nature Communications, 2016. **7**(1): p. 10366.
49. Chen, C.S., *Mechanotransduction – a field pulling together?* Journal of Cell Science, 2008. **121**(20): p. 3285-3292.
50. Discher, D.E., P. Janmey, and Y.-l. Wang, *Tissue Cells Feel and Respond to the Stiffness of Their Substrate.* Science, 2005. **310**(5751): p. 1139-1143.
51. Ellefsen, K.L., et al., *Myosin-II mediated traction forces evoke localized Piezo1-dependent Ca2+ flickers.* Communications Biology, 2019. **2**(1): p. 298.
52. Coste, B., et al., *Piezo1 and Piezo2 are essential components of distinct mechanically activated cation channels.* Science (New York, N.Y.), 2010. **330**(6000): p. 55-60.
53. Syeda, R., et al., *Chemical activation of the mechanotransduction channel Piezo1.* eLife, 2015. **4**: p. e07369.
54. Wang, Y., et al., *A lever-like transduction pathway for long-distance chemical- and mechano-gating of the mechanosensitive Piezo1 channel.* Nature Communications, 2018. **9**(1): p. 1300.
55. De Felice, D. and A. Alaimo, *Mechanosensitive Piezo Channels in Cancer: Focus on altered Calcium Signaling in Cancer Cells and in Tumor Progression.* Cancers, 2020. **12**(7): p. 1780.
56. Bae, C., F. Sachs, and P.A. Gottlieb, *The mechanosensitive ion channel Piezo1 is inhibited by the peptide GsMTx4.* Biochemistry, 2011. **50**(29): p. 6295-6300.
57. McHugh, B.J., et al., *Integrin activation by Fam38A uses a novel mechanism of R-Ras targeting to the endoplasmic reticulum.* Journal of cell science, 2010. **123**(Pt 1): p. 51-61.
58. Saotome, K., et al., *Structure of the mechanically activated ion channel Piezo1.* Nature, 2018. **554**(7693): p. 481-486.
59. Beech, D.J. and A.C. Kalli, *Force Sensing by Piezo Channels in Cardiovascular Health and Disease.* Arteriosclerosis, Thrombosis, and Vascular Biology, 2019. **39**(11): p. 2228-2239.
60. Martinac, B., *2021 Nobel Prize for mechanosensory transduction.* Biophysical reviews, 2022. **14**(1): p. 15-20.
61. Stewart, L. and N.A. Turner, *Channelling the Force to Reprogram the Matrix: Mechanosensitive Ion Channels in Cardiac Fibroblasts.* Cells, 2021. **10**(5).
62. Kefauver, J.M., A.B. Ward, and A. Patapoutian, *Discoveries in structure and physiology of mechanically activated ion channels.* Nature, 2020. **587**(7835): p. 567-576.
63. Haselwandter, C.A. and R. MacKinnon, *Piezo's membrane footprint and its contribution to mechanosensitivity.* eLife, 2018. **7**: p. e41968.
64. Wang, J., et al., *Tethering Piezo channels to the actin cytoskeleton for mechanogating via the cadherin-β-catenin mechanotransduction complex.* Cell Reports, 2022. **38**(6): p. 110342.
65. Chen, H., et al., *Mechanosensing by the α6-integrin confers an invasive fibroblast phenotype and mediates lung fibrosis.* Nature Communications, 2016. **7**(1): p. 12564.
66. Gao, Y., et al., *Mechanical strain promotes skin fibrosis through LRG-1 induction mediated by ELK1 and ERK signalling.* Communications Biology, 2019. **2**(1): p. 359.
67. Herum, K.M., et al., *Mechanical regulation of cardiac fibroblast profibrotic phenotypes.* Molecular biology of the cell, 2017. **28**(14): p. 1871-1882.

68. Braidotti, N., et al. *Piezo1 Channel as a Potential Target for Hindering Cardiac Fibrotic Remodeling*. International Journal of Molecular Sciences, 2022. **23**, DOI: 10.3390/ijms23158065.
69. Landry, N.M., S.G. Rattan, and I.M.C. Dixon, *An Improved Method of Maintaining Primary Murine Cardiac Fibroblasts in Two-Dimensional Cell Culture.* Scientific Reports, 2019. **9**(1): p. 12889.
70. Kudryashova, N., et al., *Virtual cardiac monolayers for electrical wave propagation.* Scientific Reports, 2017. **7**(1): p. 7887.
71. Johnson, B.Z., et al., *The Role of IL-6 in Skin Fibrosis and Cutaneous Wound Healing.* Biomedicines, 2020. **8**(5): p. 101.
72. Chambers, R., *Abnormal wound healing responses in pulmonary fibrosis: Focus on coagulation signalling.* European Respiratory Review, 2008. **17**.
73. Ceccato, T.L., et al., *Defining the Cardiac Fibroblast Secretome in a Fibrotic Microenvironment.* Journal of the American Heart Association, 2020. **9**(19): p. e017025.
74. Gibb, A.A., M.P. Lazaropoulos, and J.W. Elrod, *Myofibroblasts and Fibrosis.* Circulation Research, 2020. **127**(3): p. 427-447.
75. Tschumperlin, D.J., et al., *Mechanosensing and fibrosis.* The Journal of clinical investigation, 2018. **128**(1): p. 74-84.
76. Wiśniewska, J., et al., *Perspective on Stem Cell Therapy in Organ Fibrosis: Animal Models and Human Studies.* Life (Basel, Switzerland), 2021. **11**(10): p. 1068.
77. Fang, L., A.J. Murphy, and A.M. Dart, *A Clinical Perspective of Anti-Fibrotic Therapies for Cardiovascular Disease.* Frontiers in Pharmacology, 2017. **8**.
78. Park, S., et al., *Cardiac fibrosis: potential therapeutic targets.* Translational research : the journal of laboratory and clinical medicine, 2019. **209**: p. 121-137.
79. Vincent, J., *Biomimetics--a review.* Proceedings of the Institution of Mechanical Engineers. Part H, Journal of engineering in medicine, 2009. **223**: p. 919-39.
80. Suresh Kumar, N., et al., *A review on biological and biomimetic materials and their applications.* Applied Physics A, 2020. **126**(6): p. 445.
81. Sahan, A.Z., M. Baday, and C.B. Patel *Biomimetic Hydrogels in the Study of Cancer Mechanobiology: Overview, Biomedical Applications, and Future Perspectives*. Gels, 2022. **8**, DOI: 10.3390/gels8080496.
82. Cacopardo, L., N. Guazzelli, and A. Ahluwalia, *Characterizing and Engineering Biomimetic Materials for Viscoelastic Mechanotransduction Studies.* Tissue engineering. Part B, Reviews, 2022. **28**(4): p. 912-925.
83. Yi, B., Q. Xu, and W. Liu, *An overview of substrate stiffness guided cellular response and its applications in tissue regeneration.* Bioactive Materials, 2022. **15**: p. 82-102.
84. Luo, T., et al., *A Review on the Design of Hydrogels With Different Stiffness and Their Effects on Tissue Repair.* Frontiers in bioengineering and biotechnology, 2022. **10**: p. 817391-817391.
85. Li, X., et al., *Functional Hydrogels With Tunable Structures and Properties for Tissue Engineering Applications.* Frontiers in chemistry, 2018. **6**: p. 499-499.
86. Brandl, F., F. Sommer, and A. Goepferich, *Rational design of hydrogels for tissue engineering: Impact of physical factors on cell behavior.* Biomaterials, 2007. **28**(2): p. 134-146.
87. Hall, C., et al., *Chronic activation of human cardiac fibroblasts in vitro attenuates the reversibility of the myofibroblast phenotype.* Scientific Reports, 2023. **13**(1): p. 12137.
88. Gilles, G., et al., *Maintaining resting cardiac fibroblasts in vitro by disrupting mechanotransduction.* PloS one, 2020. **15**(10): p. e0241390-e0241390.
89. Asano, S., et al., *Matrix stiffness regulates migration of human lung fibroblasts.* Physiological reports, 2017. **5**(9): p. e13281.

90. Yang, T.-H., *Recent Applications of Polyacrylamide as Biomaterials.* Recent Patents on Materials Science, 2008. **100**.
91. Caliari, S.R. and J.A. Burdick, *A practical guide to hydrogels for cell culture.* Nature Methods, 2016. **13**(5): p. 405-414.
92. Subramani, R., et al., *The Influence of Swelling on Elastic Properties of Polyacrylamide Hydrogels.* Frontiers in Materials, 2020. **7**: p. 212.
93. Bercea, M. *Bioinspired Hydrogels as Platforms for Life-Science Applications: Challenges and Opportunities*. Polymers, 2022. **14**, DOI: 10.3390/polym14122365.
94. Sheth, S., et al., *UV Dose Governs UV-Polymerized Polyacrylamide Hydrogel Modulus.* International Journal of Polymer Science, 2017. **2017**: p. 5147482.
95. Nasrollahi, S., et al., *Past matrix stiffness primes epithelial cells and regulates their future collective migration through a mechanical memory.* Biomaterials, 2017. **146**: p. 146-155.
96. Fiore, A.P.Z.P., et al., *Extracellular matrix stiffness regulates degradation of MST2 via SCF βTrCP.* Biochimica et Biophysica Acta (BBA) - General Subjects, 2022. **1866**(12): p. 130238.
97. Hayashi, K., et al., *One-Step Synthesis of Gelatin-Conjugated Supramolecular Hydrogels for Dynamic Regulation of Adhesion Contact and Morphology of Myoblasts.* ACS Applied Polymer Materials, 2022. **4**(4): p. 2595-2603.
98. Sun, Y., et al., *Matrix stiffness regulates myocardial differentiation of human umbilical cord mesenchymal stem cells.* Aging, 2020. **13**(2): p. 2231-2250.
99. Xie, J., et al., *Energy expenditure during cell spreading influences the cellular response to matrix stiffness.* Biomaterials, 2021. **267**: p. 120494.
100. Hinz, B., et al., *Alpha-smooth muscle actin is crucial for focal adhesion maturation in myofibroblasts.* Molecular biology of the cell, 2003. **14**(6): p. 2508-2519.
101. Liu, F., et al., *Feedback amplification of fibrosis through matrix stiffening and COX-2 suppression.* The Journal of cell biology, 2010. **190**(4): p. 693-706.
102. Adamczyk, O., et al., *Substrate Stiffness Mediates Formation of Novel Cytoskeletal Structures in Fibroblasts during Cell-Microspheres Interaction.* International journal of molecular sciences, 2021. **22**(2): p. 960.
103. Sunyer, R., et al., *Fabrication of Hydrogels with Steep Stiffness Gradients for Studying Cell Mechanical Response.* PLOS ONE, 2012. **7**(10): p. e46107.
104. Charrier, E.E., et al., *Control of cell morphology and differentiation by substrates with independently tunable elasticity and viscous dissipation.* Nature Communications, 2018. **9**(1): p. 449.
105. Lembong, J., B. Sabass, and H.A. Stone, *Calcium oscillations in wounded fibroblast monolayers are spatially regulated through substrate mechanics.* Physical Biology, 2017. **14**(4): p. 045006.
106. Elliott, C.G., et al., *Periostin modulates myofibroblast differentiation during full-thickness cutaneous wound repair.* Journal of cell science, 2012. **125**(Pt 1): p. 121-132.
107. Gałdyszyńska, M., et al., *The stiffness-controlled release of interleukin-6 by cardiac fibroblasts is dependent on integrin α2β1.* Journal of cellular and molecular medicine, 2020. **24**(23): p. 13853-13862.
108. Gałdyszyńska, M., et al., *The Stiffness of Cardiac Fibroblast Substrates Exerts a Regulatory Influence on Collagen Metabolism via α2β1 Integrin, FAK and Src Kinases.* Cells, 2021. **10**(12): p. 3506.
109. Yong, K.W., et al., *Paracrine Effects of Adipose-Derived Stem Cells on Matrix Stiffness-Induced Cardiac Myofibroblast Differentiation via Angiotensin II Type 1 Receptor and Smad7.* Scientific Reports, 2016. **6**(1): p. 33067.
110. Daliri, K., K. Pfannkuche, and B. Garipcan, *Effects of physicochemical properties of polyacrylamide (PAA) and (polydimethylsiloxane) PDMS on cardiac cell behavior.* Soft Matter, 2021. **17**(5): p. 1156-1172.

111. Ribeiro, A.J.S., et al., *For whom the cells pull: Hydrogel and micropost devices for measuring traction forces.* Methods, 2016. **94**: p. 51-64.
112. Chuah, Y.J., et al., *Combinatorial effect of substratum properties on mesenchymal stem cell sheet engineering and subsequent multi-lineage differentiation.* Acta Biomaterialia, 2015. **23**: p. 52-62.
113. Menon, N.V., et al., *Microfluidic Assay To Study the Combinatorial Impact of Substrate Properties on Mesenchymal Stem Cell Migration.* ACS Applied Materials & Interfaces, 2015. **7**(31): p. 17095-17103.
114. Yeh, Y.-C., et al., *Mechanically dynamic PDMS substrates to investigate changing cell environments.* Biomaterials, 2017. **145**: p. 23-32.
115. Chuah, Y.J., et al., *Simple surface engineering of polydimethylsiloxane with polydopamine for stabilized mesenchymal stem cell adhesion and multipotency.* Scientific Reports, 2015. **5**(1): p. 18162.
116. Tanyeri, M. and S. Tay, *Chapter 1 - Viable cell culture in PDMS-based microfluidic devices*, in *Methods in Cell Biology*, D.A. Fletcher, J. Doh, and M. Piel, Editors. 2018, Academic Press. p. 3-33.
117. Seghir, R. and S. Arscott, *Extended PDMS stiffness range for flexible systems.* Sensors and Actuators A: Physical, 2015. **230**: p. 33-39.
118. Goffin, J.M., et al., *Focal adhesion size controls tension-dependent recruitment of alpha-smooth muscle actin to stress fibers.* The Journal of cell biology, 2006. **172**(2): p. 259-268.
119. Balestrini, J.L., et al., *The mechanical memory of lung myofibroblasts.* Integrative Biology, 2012. **4**(4): p. 410-421.
120. Shi, Y., et al., *Substrate stiffness influences TGF-β1-induced differentiation of bronchial fibroblasts into myofibroblasts in airway remodeling.* Mol Med Rep, 2013. **7**(2): p. 419-424.
121. Marquet, P. and C. Depeursinge, *Cellular Dynamics Revealed by Digital Holographic Microscopy*, in *Encyclopedia of Neuroscience*, L.R. Squire, Editor. 2009, Academic Press: Oxford. p. 675-683.
122. Kasprowicz, R., R. Suman, and P. O'Toole, *Characterising live cell behaviour: Traditional label-free and quantitative phase imaging approaches.* The International Journal of Biochemistry & Cell Biology, 2017. **84**: p. 89-95.
123. Shaked, N.T., Z. Zalevsky, and L.L. Satterwhite, *Biomedical Optical Phase Microscopy and Nanoscopy*. 2012: Elsevier Science.
124. Nguyen, T.L., et al., *Quantitative Phase Imaging: Recent Advances and Expanding Potential in Biomedicine.* ACS Nano, 2022. **16**(8): p. 11516-11544.
125. Myung, K.K., *Principles and techniques of digital holographic microscopy.* SPIE Reviews, 2010. **1**(1): p. 018005.
126. Picazo-Bueno, J.Á., et al., *Single-shot, dual-mode, water-immersion microscopy platform for biological applications.* Applied Optics, 2018. **57**(1): p. A242-A249.
127. Marquet, P., et al., *Digital holographic microscopy: a noninvasive contrast imaging technique allowing quantitative visualization of living cells with subwavelength axial accuracy.* Optics Letters, 2005. **30**(5): p. 468-470.
128. Braidotti, N., et al., *The Role of Cytoskeleton Revealed by Quartz Crystal Microbalance and Digital Holographic Microscopy.* International journal of molecular sciences, 2022. **23**(8): p. 4108.
129. Cao, R., et al., *Quantitative observations on cytoskeleton changes of osteocytes at different cell parts using digital holographic microscopy.* Biomedical Optics Express, 2018. **9**(1): p. 72-85.
130. do R. B. F. Lima, M.A. and D. Cojoc, *Monitoring Human Neutrophil Differentiation by Digital Holographic Microscopy.* Frontiers in Physics, 2021. **9**.
131. Renz, M., *Fluorescence microscopy—A historical and technical perspective.* Cytometry Part A, 2013. **83**(9): p. 767-779.

132. Sanderson, M.J., et al., *Fluorescence microscopy.* Cold Spring Harbor protocols, 2014. **2014**(10): p. pdb.top071795-pdb.top071795.
133. Huang, B., H. Babcock, and X. Zhuang, *Breaking the diffraction barrier: super-resolution imaging of cells.* Cell, 2010. **143**(7): p. 1047-1058.
134. Jonkman, J., et al., *Tutorial: guidance for quantitative confocal microscopy.* Nature Protocols, 2020. **15**(5): p. 1585-1611.
135. Elliott, A.D., *Confocal Microscopy: Principles and Modern Practices.* Current protocols in cytometry, 2020. **92**(1): p. e68-e68.
136. Longchao, C., W. Yuling, and S. Wei, *Super-Resolution Confocal Microscopy Through Pixel Reassignment*, in *Microscopy and Analysis*, G.S. Stefan, Editor. 2016, IntechOpen: Rijeka. p. Ch. 4.
137. Hell, S.W. and J. Wichmann, *Breaking the diffraction resolution limit by stimulated emission: stimulated-emission-depletion fluorescence microscopy.* Optics Letters, 1994. **19**(11): p. 780-782.
138. Chéreau, R., J. Tønnesen, and U.V. Nägerl, *STED microscopy for nanoscale imaging in living brain slices.* Methods, 2015. **88**: p. 57-66.
139. Hao, X., et al., *From microscopy to nanoscopy via visible light.* Light: Science & Applications, 2013. **2**(10): p. e108-e108.
140. Ranjit, S., et al., *Advances in fluorescence microscopy techniques to study kidney function.* Nature Reviews Nephrology, 2021. **17**(2): p. 128-144.
141. Betzig, E., et al., *Imaging Intracellular Fluorescent Proteins at Nanometer Resolution.* Science, 2006. **313**(5793): p. 1642-1645.
142. Rust, M.J., M. Bates, and X. Zhuang, *Sub-diffraction-limit imaging by stochastic optical reconstruction microscopy (STORM).* Nature Methods, 2006. **3**(10): p. 793-796.
143. Gustafsson, M.G.L., *Surpassing the lateral resolution limit by a factor of two using structured illumination microscopy.* Journal of Microscopy, 2000. **198**(2): p. 82-87.
144. Lazarides, E., *Immunofluorescence studies on the structure of actin filaments in tissue culture cells.* Journal of Histochemistry & Cytochemistry, 1975. **23**(7): p. 507-528.
145. Han, Y., et al., *A Labeling Strategy for Living Specimens in Long-Term/Super-Resolution Fluorescence Imaging.* Frontiers in chemistry, 2021. **8**: p. 601436-601436.
146. Sauerbrey, G., *Verwendung von Schwingquarzen zur Wägung dünner Schichten und zur Mikrowägung.* Zeitschrift für Physik, 1959. **155**(2): p. 206-222.
147. Kanazawa, K.K. and J.G. Gordon, *Frequency of a quartz microbalance in contact with liquid.* Analytical Chemistry, 1985. **57**(8): p. 1770-1771.
148. Voinova, M.V., M. Jonson, and B. Kasemo, *'Missing mass' effect in biosensor's QCM applications.* Biosensors and Bioelectronics, 2002. **17**(10): p. 835-841.
149. V., V.M., J. M., and K. B., *Dynamics of viscous amphiphilic films supported by elastic solid substrates.* Journal of Physics: Condensed Matter, 1997. **9**(37): p. 7799.
150. Marx, K.A., et al., *A comparative study of the cytoskeleton binding drugs nocodazole and taxol with a mammalian cell quartz crystal microbalance biosensor: Different dynamic responses and energy dissipation effects.* Analytical Biochemistry, 2007. **361**(1): p. 77-92.
151. Marx, K.A., et al., *Quartz crystal microbalance biosensor study of endothelial cells and their extracellular matrix following cell removal: Evidence for transient cellular stress and viscoelastic changes during detachment and the elastic behavior of the pure matrix.* Analytical Biochemistry, 2005. **343**(1): p. 23-34.
152. Marx, K.A., et al., *A quartz crystal microbalance cell biosensor: detection of microtubule alterations in living cells at nM nocodazole concentrations.* Biosensors and Bioelectronics, 2001. **16**(9): p. 773-782.
153. Galli Marxer, C., et al., *Cell spreading on quartz crystal microbalance elicits positive frequency shifts indicative of viscosity changes.* Analytical and Bioanalytical Chemistry, 2003. **377**(3): p. 578-586.

154. Rodahl, M. and B. Kasemo, *Frequency and dissipation-factor responses to localized liquid deposits on a QCM electrode.* Sensors and Actuators B: Chemical, 1996. **37**(1): p. 111-116.
155. Rodahl, M., et al., *Quartz crystal microbalance setup for frequency and Q-factor measurements in gaseous and liquid environments.* Review of Scientific Instruments, 1995. **66**(7): p. 3924-3930.
156. Wegener, J., A. Janshoff, and H.J. Galla, *Cell adhesion monitoring using a quartz crystal microbalance: comparative analysis of different mammalian cell lines.* European Biophysics Journal, 1998. **28**(1): p. 26-37.
157. Wegener, J., et al., *Analysis of the Composite Response of Shear Wave Resonators to the Attachment of Mammalian Cells.* Biophysical Journal, 2000. **78**(6): p. 2821-2833.
158. Chen, J.Y., L.S. Penn, and J. Xi, *Quartz crystal microbalance: Sensing cell-substrate adhesion and beyond.* Biosensors and Bioelectronics, 2018. **99**: p. 593-602.
159. Tymchenko, N., et al., *Reversible Changes in Cell Morphology due to Cytoskeletal Rearrangements Measured in Real-Time by QCM-D.* Biointerphases, 2012. **7**(1): p. 43.
160. González-Bermúdez, B., G.V. Guinea, and G.R. Plaza, *Advances in Micropipette Aspiration: Applications in Cell Biomechanics, Models, and Extended Studies.* Biophysical Journal, 2019. **116**(4): p. 587-594.
161. Wang, H., et al., *Micropipette-based biomechanical nanotools on living cells.* European biophysics journal : EBJ, 2022. **51**(2): p. 119-133.
162. Tan, S.C.W., et al., *Viscoelastic behaviour of human mesenchymal stem cells.* BMC cell biology, 2008. **9**: p. 40-40.
163. Lee, L.M. and A.P. Liu, *The Application of Micropipette Aspiration in Molecular Mechanics of Single Cells.* Journal of nanotechnology in engineering and medicine, 2014. **5**(4): p. 0408011-408016.
164. Guevorkian, K. and J.L. Maître, *Chapter 10 - Micropipette aspiration: A unique tool for exploring cell and tissue mechanics in vivo*, in *Methods in Cell Biology*, T. Lecuit, Editor. 2017, Academic Press. p. 187-201.
165. Jones, W.R., et al., *Alterations in the Young's modulus and volumetric properties of chondrocytes isolated from normal and osteoarthritic human cartilage.* Journal of Biomechanics, 1999. **32**(2): p. 119-127.
166. Zhou, E.H., S.T. Quek, and C.T. Lim, *Power-law rheology analysis of cells undergoing micropipette aspiration.* Biomechanics and Modeling in Mechanobiology, 2010. **9**(5): p. 563-572.
167. Artmann, G.M., et al., *Micropipette aspiration of human erythrocytes induces echinocytes via membrane phospholipid translocation.* Biophysical Journal, 1997. **72**(3): p. 1434-1441.
168. Engström, K.G. and H.J. Meiselman, *Effects of pressure on red blood cell geometry during micropipette aspiration.* Cytometry, 1996. **23**(1): p. 22-27.
169. Wang, H., et al., *Fluorescence-coupled micropipette aspiration assay to examine calcium mobilization caused by red blood cell mechanosensing.* European biophysics journal : EBJ, 2022. **51**(2): p. 135-146.
170. Binnig, G., C.F. Quate, and C. Gerber, *Atomic Force Microscope.* Physical Review Letters, 1986. **56**(9): p. 930-933.
171. Andolfi, L., et al., *Scanning Probe Microscopies: Imaging and Biomechanics in Reproductive Medicine Research.* International journal of molecular sciences, 2021. **22**(8): p. 3823.
172. Borin, D., et al., *Novel insights into cardiomyocytes provided by atomic force microscopy.* Seminars in Cell & Developmental Biology, 2018. **73**: p. 4-12.
173. Benitez, R. and J.L. Toca-herrera, *Looking at cell mechanics with atomic force microscopy: Experiment and theory.* Microscopy Research and Technique, 2014. **77**(11): p. 947-958.
174. Gavara, N., *A beginner's guide to atomic force microscopy probing for cell mechanics.* Microscopy research and technique, 2017. **80**(1): p. 75-84.

175. Kuznetsova, T.G., et al., *Atomic force microscopy probing of cell elasticity.* Micron, 2007. **38**(8): p. 824-833.
176. Jung, W., et al., *Nonlinear Elastic and Inelastic Properties of Cells.* Journal of biomechanical engineering, 2020. **142**(10): p. 100806.
177. Ashkin, A., *Optical Trapping and Manipulation of Neutral Particles Using Lasers*. 2006: World Scientific.
178. Ashkin, A., *Forces of a single-beam gradient laser trap on a dielectric sphere in the ray optics regime.* Biophysical journal, 1992. **61**(2): p. 569-582.
179. van Mameren, J., G.J.L. Wuite, and I. Heller, *Introduction to Optical Tweezers: Background, System Designs, and Commercial Solutions*, in *Single Molecule Analysis: Methods and Protocols*, E.J.G. Peterman, Editor. 2018, Springer New York: New York, NY. p. 3-23.
180. Avsievich, T., et al., *The advancement of blood cell research by optical tweezers.* Reviews in Physics, 2020. **5**: p. 100043.
181. Bustamante, C.J., et al., *Optical tweezers in single-molecule biophysics.* Nature Reviews Methods Primers, 2021. **1**(1): p. 25.
182. Harada, Y. and T. Asakura, *Radiation forces on a dielectric sphere in the Rayleigh scattering regime.* Optics Communications, 1996. **124**(5): p. 529-541.
183. Yousafzai, M.S., et al., *Substrate-dependent cell elasticity measured by optical tweezers indentation.* Optics and Lasers in Engineering, 2016. **76**: p. 27-33.
184. Sun, W., et al., *Biophysical Approaches for Applying and Measuring Biological Forces.* Advanced Science, 2022. **9**(5): p. 2105254.
185. Titushkin, I. and M. Cho, *Distinct Membrane Mechanical Properties of Human Mesenchymal Stem Cells Determined Using Laser Optical Tweezers.* Biophysical Journal, 2006. **90**(7): p. 2582-2591.
186. Pontes, B., P. Monzo, and N.C. Gauthier, *Membrane tension: A challenging but universal physical parameter in cell biology.* Seminars in Cell & Developmental Biology, 2017. **71**: p. 30-41.
187. Raucher, D. and M.P. Sheetz, *Characteristics of a Membrane Reservoir Buffering Membrane Tension.* Biophysical Journal, 1999. **77**(4): p. 1992-2002.
188. Kubitschke, H., et al., *Actin and microtubule networks contribute differently to cell response for small and large strains.* New Journal of Physics, 2017. **19**(9): p. 093003.
189. Wakatsuki, T., et al., *Effects of cytochalasin D and latrunculin B on mechanical properties of cells.* Journal of Cell Science, 2001. **114**(5): p. 1025-1036.
190. Ingber, D.E., N. Wang, and D. Stamenović, *Tensegrity, cellular biophysics, and the mechanics of living systems.* Reports on Progress in Physics, 2014. **77**(4): p. 046603.
191. Stamenović, D. and D.E. Ingber, *Models of cytoskeletal mechanics of adherent cells.* Biomechanics and Modeling in Mechanobiology, 2002. **1**(1): p. 95-108.
192. Rappaz, B., et al., *Spatial analysis of erythrocyte membrane fluctuations by digital holographic microscopy.* Blood Cells, Molecules, and Diseases, 2009. **42**(3): p. 228-232.
193. Marquet, P., C. Depeursinge, and P.J. Magistretti, *Review of quantitative phase-digital holographic microscopy: promising novel imaging technique to resolve neuronal network activity and identify cellular biomarkers of psychiatric disorders.* Neurophotonics, 2014. **1**(2): p. 020901-020901.
194. Yahara, I., et al., *Correlation between effects of 24 different cytochalasins on cellular structures and cellular events and those on actin in vitro.* Journal of Cell Biology, 1982. **92**(1): p. 69-78.
195. Middleton, C.A., et al., *The polarization of fibroblasts in early primary cultures is independent of microtubule integrity.* Journal of Cell Science, 1989. **94**(1): p. 25-32.
196. Kole, T.P., et al., *Intracellular mechanics of migrating fibroblasts.* Molecular biology of the cell, 2005. **16**(1): p. 328-338.

197. Gardner, Steven J., et al., *Measuring the Refractive Index of Bovine Corneal Stromal Cells Using Quantitative Phase Imaging.* Biophysical Journal, 2015. **109**(8): p. 1592-1599.
198. Kim, E., et al., *Semiautomated analysis of optical coherence tomography crystalline lens images under simulated accommodation.* Journal of biomedical optics, 2011. **16**(5): p. 056003-056003.
199. Li, F., J.H.C. Wang, and Q.-M. Wang, *Monitoring cell adhesion by using thickness shear mode acoustic wave sensors.* Biosensors and Bioelectronics, 2007. **23**(1): p. 42-50.
200. Gronewold, T.M.A., et al., *Effects of rhizopodin and latrunculin B on the morphology and on the actin cytoskeleton of mammalian cells.* Cell and Tissue Research, 1999. **295**(1): p. 121-129.
201. Ayala, Y.A., et al., *Effects of cytoskeletal drugs on actin cortex elasticity.* Experimental Cell Research, 2017. **351**(2): p. 173-181.
202. Trickey, W.R., T.P. Vail, and F. Guilak, *The role of the cytoskeleton in the viscoelastic properties of human articular chondrocytes.* Journal of Orthopaedic Research, 2004. **22**(1): p. 131-139.
203. Haase, K. and A.E. Pelling, *The role of the actin cortex in maintaining cell shape.* Communicative & integrative biology, 2013. **6**(6): p. e26714-e26714.
204. Brückner, B.R., H. Nöding, and A. Janshoff, *Viscoelastic Properties of Confluent MDCK II Cells Obtained from Force Cycle Experiments.* Biophysical Journal, 2017. **112**(4): p. 724-735.
205. Kim, A. and W. Matthew Petroll, *Microtubule regulation of corneal fibroblast morphology and mechanical activity in 3-D culture.* Experimental eye research, 2007. **85**(4): p. 546-556.
206. Smyth, J.T., et al., *Role of the microtubule cytoskeleton in the function of the store-operated Ca2+ channel activator STIM1.* Journal of Cell Science, 2007. **120**(21): p. 3762-3771.
207. Wu, H.W., T. Kuhn, and V.T. Moy, *Mechanical properties of L929 cells measured by atomic force microscopy: Effects of anticytoskeletal drugs and membrane crosslinking.* Scanning, 1998. **20**(5): p. 389-397.
208. Chang, Y.-C., et al., *GEF-H1 couples nocodazole-induced microtubule disassembly to cell contractility via RhoA.* Molecular biology of the cell, 2008. **19**(5): p. 2147-2153.
209. Meiri, D., et al., *Mechanistic Insight into the Microtubule and Actin Cytoskeleton Coupling through Dynein-Dependent RhoGEF Inhibition.* Molecular Cell, 2012. **45**(5): p. 642-655.
210. Borin, D., et al., *An engineering insight into the relationship of selective cytoskeletal impairment and biomechanics of HeLa cells.* Micron, 2017. **102**: p. 88-96.
211. Cai, P., et al., *Temporal Variation in Single-Cell Power-Law Rheology Spans the Ensemble Variation of Cell Population.* Biophysical Journal, 2017. **113**(3): p. 671-678.
212. Liu, X., et al., *Rheology characterization of sol–gel transition in aqueous alginate solutions induced by calcium cations through in situ release.* Polymer, 2003. **44**(2): p. 407-412.
213. Grady, M.E., R.J. Composto, and D.M. Eckmann, *Cell elasticity with altered cytoskeletal architectures across multiple cell types.* Journal of the Mechanical Behavior of Biomedical Materials, 2016. **61**: p. 197-207.
214. Rotsch, C. and M. Radmacher, *Drug-Induced Changes of Cytoskeletal Structure and Mechanics in Fibroblasts: An Atomic Force Microscopy Study.* Biophysical Journal, 2000. **78**(1): p. 520-535.
215. Omelchenko, T., et al., *Mechanisms of polarization of the shape of fibroblasts and epitheliocytes: Separation of the roles of microtubules and Rho-dependent actin–myosin contractility.* Proceedings of the National Academy of Sciences, 2002. **99**(16): p. 10452-10457.
216. Dai, J. and M.P. Sheetz, *Mechanical properties of neuronal growth cone membranes studied by tether formation with laser optical tweezers.* Biophysical journal, 1995. **68**(3): p. 988-996.
217. Khatibzadeh, N., et al., *Effects of cholesterol on nano-mechanical properties of the living cell plasma membrane.* Soft Matter, 2012. **8**(32): p. 8350-8360.

218. Godbout, C., et al., *The mechanical environment modulates intracellular calcium oscillation activities of myofibroblasts.* PloS one, 2013. **8**(5): p. e64560-e64560.
219. Thompson, S.A., et al., *Mechanical Coupling Between Myofibroblasts and Cardiomyocytes Slows Electric Conduction in Fibrotic Cell Monolayers.* Circulation, 2011. **123**(19): p. 2083-2093.
220. Zhao, M., et al., *Targeting fibrosis: mechanisms and clinical trials.* Signal Transduction and Targeted Therapy, 2022. **7**(1): p. 206.
221. Vukicevic, S., et al., *Bone morphogenetic protein 1.3 inhibition decreases scar formation and supports cardiomyocyte survival after myocardial infarction.* Nature Communications, 2022. **13**(1): p. 81.
222. Hillsley, A., J.E. Santos, and A.M. Rosales, *A deep learning approach to identify and segment alpha-smooth muscle actin stress fiber positive cells.* Scientific Reports, 2021. **11**(1): p. 21855.
223. López, B., et al., *Diffuse myocardial fibrosis: mechanisms, diagnosis and therapeutic approaches.* Nature Reviews Cardiology, 2021. **18**(7): p. 479-498.
224. Pesce, M., et al., *Cardiac fibroblasts and mechanosensation in heart development, health and disease.* Nature Reviews Cardiology, 2023. **20**(5): p. 309-324.
225. Nikolaev, Y.A., et al., *Mammalian TRP ion channels are insensitive to membrane stretch.* Journal of cell science, 2019. **132**(23): p. jcs238360.
226. Guo, Y., et al., *The Ca(2+)-activated cation channel TRPM4 is a positive regulator of pressure overload-induced cardiac hypertrophy.* eLife, 2021. **10**: p. e66582.
227. Swain, S.M. and R.A. Liddle, *Piezo1 acts upstream of TRPV4 to induce pathological changes in endothelial cells due to shear stress.* The Journal of biological chemistry, 2021. **296**: p. 100171-100171.
228. Swain, S.M., et al., *TRPV4 channel opening mediates pressure-induced pancreatitis initiated by Piezo1 activation.* The Journal of Clinical Investigation, 2020. **130**(5): p. 2527-2541.
229. Yu, Z.-Y., et al., *Piezo1 is the cardiac mechanosensor that initiates the cardiomyocyte hypertrophic response to pressure overload in adult mice.* Nature Cardiovascular Research, 2022. **1**(6): p. 577-591.
230. Ramires, F.J.A., Y. Sun, and K.T. Weber, *Myocardial Fibrosis Associated with Aldosterone or Angiotensin II Administration: Attenuation by Calcium Channel Blockade.* Journal of Molecular and Cellular Cardiology, 1998. **30**(3): p. 475-483.
231. Du, J., et al., *TRPM7-mediated Ca2+ signals confer fibrogenesis in human atrial fibrillation.* Circulation research, 2010. **106**(5): p. 992-1003.
232. Mohamed, T.M.A., et al., *The plasma membrane calcium ATPase 4 signalling in cardiac fibroblasts mediates cardiomyocyte hypertrophy.* Nature Communications, 2016. **7**(1): p. 11074.
233. Lombardi, A.A., et al., *Mitochondrial calcium exchange links metabolism with the epigenome to control cellular differentiation.* Nature Communications, 2019. **10**(1): p. 4509.
234. Niu, L., et al., *A positive mechanobiological feedback loop controls bistable switching of cardiac fibroblast phenotype.* Cell Discovery, 2022. **8**(1): p. 84.
235. Falleroni, F., et al., *Mechanotransduction in hippocampal neurons operates under localized low picoNewton forces.* iScience, 2022. **25**(2): p. 103807-103807.
236. te Riet, J., et al., *Interlaboratory round robin on cantilever calibration for AFM force spectroscopy.* Ultramicroscopy, 2011. **111**(12): p. 1659-1669.
237. Dulińska-Molak, I., et al., *Age-Related Changes in the Mechanical Properties of Human Fibroblasts and Its Prospective Reversal After Anti-Wrinkle Tripeptide Treatment.* International journal of peptide research and therapeutics, 2014. **20**(1): p. 77-85.
238. Yousafzai, M.S., et al., *Investigating the effect of cell substrate on cancer cell stiffness by optical tweezers.* Journal of Biomechanics, 2017. **60**: p. 266-269.

239. Chen, W.-H., et al., *Probing relevant molecules in modulating the neurite outgrowth of hippocampal neurons on substrates of different stiffness.* PloS one, 2013. **8**(12): p. e83394-e83394.
240. Balaban, N.Q., et al., *Force and focal adhesion assembly: a close relationship studied using elastic micropatterned substrates.* Nature Cell Biology, 2001. **3**(5): p. 466-472.
241. Lin, Y.-W., et al., *Understanding sensory nerve mechanotransduction through localized elastomeric matrix control.* PloS one, 2009. **4**(1): p. e4293-e4293.
242. Gaub, B.M. and D.J. Müller, *Mechanical Stimulation of Piezo1 Receptors Depends on Extracellular Matrix Proteins and Directionality of Force.* Nano Letters, 2017. **17**(3): p. 2064-2072.
243. Barros, V., *The heart cycle: review.* Women's Health, 2019. **8**: p. 66-69.
244. Ogilvie, L.M., et al., *A new approach to improve the hemodynamic assessment of cardiac function independent of respiratory influence.* Scientific Reports, 2021. **11**(1): p. 17223.
245. Zamponi, N., et al., *Mitochondrial network complexity emerges from fission/fusion dynamics.* Scientific Reports, 2018. **8**(1): p. 363.
246. Antony, P.M.A., et al., *Fibroblast mitochondria in idiopathic Parkinson's disease display morphological changes and enhanced resistance to depolarization.* Scientific Reports, 2020. **10**(1): p. 1569.
247. Montero, M., et al., *Chromaffin-cell stimulation triggers fast millimolar mitochondrial Ca2+ transients that modulate secretion.* Nature Cell Biology, 2000. **2**(2): p. 57-61.
248. Newburger, E., M. Correll, and N. Elmqvist, *Fitting Bell Curves to Data Distributions Using Visualization.* IEEE Transactions on Visualization and Computer Graphics, 2022: p. 1-12.
249. Jakob, D., et al., *Piezo1 and BKCa channels in human atrial fibroblasts: Interplay and remodelling in atrial fibrillation.* Journal of Molecular and Cellular Cardiology, 2021. **158**: p. 49-62.
250. Ashby, M.F., *Materials selection in mechanical design*. 2005, Butterworth-Heinemann: Amsterdam.
251. Solon, J., et al., *Fibroblast adaptation and stiffness matching to soft elastic substrates.* Biophysical journal, 2007. **93**(12): p. 4453-4461.
252. Morley, S.J., et al., *Acetylated tubulin is essential for touch sensation in mice.* eLife, 2016. **5**: p. e20813.
253. Qi, Y., et al., *Membrane stiffening by STOML3 facilitates mechanosensation in sensory neurons.* Nature Communications, 2015. **6**(1): p. 8512.
254. Aghajanian, H., et al., *Targeting cardiac fibrosis with engineered T cells.* Nature, 2019. **573**(7774): p. 430-433.
255. Ko, T., et al., *Cardiac fibroblasts regulate the development of heart failure via Htra3-TGF-β-IGFBP7 axis.* Nature Communications, 2022. **13**(1): p. 3275.
256. Ebrahimighaei, R., et al., *Combined role for YAP-TEAD and YAP-RUNX2 signalling in substrate-stiffness regulation of cardiac fibroblast proliferation.* Biochimica et Biophysica Acta (BBA) - Molecular Cell Research, 2022. **1869**(11): p. 119329.
257. Castella, L.F., et al., *A new lock-step mechanism of matrix remodelling based on subcellular contractile events.* Journal of Cell Science, 2010. **123**(10): p. 1751-1760.
258. Shao, X., et al., *Mechanical stimulation induces formin-dependent assembly of a perinuclear actin rim.* Proceedings of the National Academy of Sciences, 2015. **112**(20): p. E2595-E2601.
259. Ruder, W.C., et al., *Calcium signaling is gated by a mechanical threshold in three-dimensional environments.* Scientific Reports, 2012. **2**(1): p. 554.
260. Yao, M., et al., *Force- and cell state–dependent recruitment of Piezo1 drives focal adhesion dynamics and calcium entry.* Science Advances. **8**(45): p. eabo1461.
261. Pathak, M.M., et al., *Stretch-activated ion channel Piezo1 directs lineage choice in human neural stem cells.* Proceedings of the National Academy of Sciences of the United States of America, 2014. **111**(45): p. 16148-16153.

262. Schroer, A.K. and W.D. Merryman, *Mechanobiology of myofibroblast adhesion in fibrotic cardiac disease.* Journal of cell science, 2015. **128**(10): p. 1865-1875.
263. Vagnozzi, R.J., A.K.Z. Johansen, and J.D. Molkentin, *CARdiac Immunotherapy: T Cells Engineered to Treat the Fibrotic Heart.* Molecular therapy : the journal of the American Society of Gene Therapy, 2019. **27**(11): p. 1869-1871.
264. Bouvet, M., et al., *Anti-integrin α(v) therapy improves cardiac fibrosis after myocardial infarction by blunting cardiac PW1(+) stromal cells.* Scientific reports, 2020. **10**(1): p. 11404-11404.
265. Besedina, N.A., et al., *Persistent red blood cells retain their ability to move in microcapillaries under high levels of oxidative stress.* Communications Biology, 2022. **5**(1): p. 659.
266. Cahalan, S.M., et al., *Piezo1 links mechanical forces to red blood cell volume.* eLife, 2015. **4**: p. e07370.
267. Gokhin, D.S., et al., *Dynamic actin filaments control the mechanical behavior of the human red blood cell membrane.* Molecular biology of the cell, 2015. **26**(9): p. 1699-1710.
268. Vaisey, G., et al., *Piezo1 as a force-through-membrane sensor in red blood cells.* eLife, 2022. **11**: p. e82621.
269. Li, X., et al., *Probing red blood cell mechanics, rheology and dynamics with a two-component multi-scale model.* Philosophical transactions. Series A, Mathematical, physical, and engineering sciences, 2014. **372**(2021): p. 20130389.
270. Peng, Z., et al., *Lipid bilayer and cytoskeletal interactions in a red blood cell.* Proceedings of the National Academy of Sciences, 2013. **110**(33): p. 13356-13361.
271. Ebrahimi, S. and P. Bagchi, *A computational study of red blood cell deformability effect on hemodynamic alteration in capillary vessel networks.* Scientific Reports, 2022. **12**(1): p. 4304.
272. Evans, E.A., *Bending elastic modulus of red blood cell membrane derived from buckling instability in micropipet aspiration tests.* Biophysical journal, 1983. **43**(1): p. 27-30.
273. Wei, Q., et al., *Evolution of surface area and membrane shear modulus of matured human red blood cells during mechanical fatigue.* Scientific Reports, 2023. **13**(1): p. 8563.
274. Barns, S., et al., *Investigation of red blood cell mechanical properties using AFM indentation and coarse-grained particle method.* BioMedical Engineering OnLine, 2017. **16**(1): p. 140.
275. Renoux, C., et al., *Impact of surface-area-to-volume ratio, internal viscosity and membrane viscoelasticity on red blood cell deformability measured in isotonic condition.* Scientific Reports, 2019. **9**(1): p. 6771.
276. Guck, J., et al., *The Optical Stretcher: A Novel Laser Tool to Micromanipulate Cells.* Biophysical Journal, 2001. **81**(2): p. 767-784.
277. Lim, H.G. and K.K. Shung, *Quantification of Inter-Erythrocyte Forces with Ultra-High Frequency (410 MHz) Single Beam Acoustic Tweezer.* Annals of Biomedical Engineering, 2017. **45**(9): p. 2174-2183.
278. Bernecker, C., et al. *Biomechanics of Ex Vivo-Generated Red Blood Cells Investigated by Optical Tweezers and Digital Holographic Microscopy*. Cells, 2021. **10**, DOI: 10.3390/cells10030552.
279. Keyvan, J. and M. Inkyu, *Quantitative investigation of red blood cell three-dimensional geometric and chemical changes in the storage lesion using digital holographic microscopy.* Journal of Biomedical Optics, 2015. **20**(11): p. 111218.
280. Gallagher, P.G., *Disorders of erythrocyte hydration.* Blood, 2017. **130**(25): p. 2699-2708.
281. Ataullakhanov, F., et al., *How Erythrocyte Volume Is Regulated, or What Mathematical Models Can and Cannot Do for Biology.* Biochemistry (Moscow) Supplement Series A Membrane and Cell Biology, 2009. **3**: p. 101-115.
282. Jankovsky, N., et al., *Recent advances in the pathophysiology of PIEZO1-related hereditary xerocytosis.* American Journal of Hematology, 2021. **96**(8): p. 1017-1026.

283. Liang, X. and J. Howard, *Structural Biology: Piezo Senses Tension through Curvature.* Current Biology, 2018. **28**(8): p. R357-R359.
284. Svetina, S., T. Švelc Kebe, and B. Božič, *A Model of Piezo1-Based Regulation of Red Blood Cell Volume.* Biophysical journal, 2019. **116**(1): p. 151-164.
285. Belkacemi, A., et al., *The TRPV2 channel mediates Ca2+ influx and the Δ9-THC-dependent decrease in osmotic fragility in red blood cells.* Haematologica, 2021. **106**(8): p. 2246-2250.
286. Egée, S. and L. Kaestner, *The Transient Receptor Potential Vanilloid Type 2 (TRPV2) Channel-A New Druggable Ca(2+) Pathway in Red Cells, Implications for Red Cell Ion Homeostasis.* Frontiers in physiology, 2021. **12**: p. 677573-677573.
287. Dyrda, A., et al., *Local membrane deformations activate Ca2+-dependent K+ and anionic currents in intact human red blood cells.* PloS one, 2010. **5**(2): p. e9447-e9447.
288. Falleroni, F., V. Torre, and D. Cojoc, *Cell Mechanotransduction With Piconewton Forces Applied by Optical Tweezers.* Frontiers in cellular neuroscience, 2018. **12**: p. 130-130.
289. Ju, L., et al., *Microscale geometrical modulation of PIEZO1 mediated cell mechanosensing via cytoskeletal redistribution buckle.* Research Square, 2023. **PREPRINT (Version 1)**.
290. Hochmuth, R.M., *Micropipette aspiration of living cells.* Journal of Biomechanics, 2000. **33**(1): p. 15-22.
291. Howard, J., *Mechanics of Motor Proteins and the Cytoskeleton*. 2001: Sinauer Associates, Publishers.
292. Kim, H.-Y., *Statistical notes for clinical researchers: Nonparametric statistical methods: 1. Nonparametric methods for comparing two groups.* Restorative dentistry & endodontics, 2014. **39**(3): p. 235-239.
293. Burns, J.M., et al., *Deterioration of red blood cell mechanical properties is reduced in anaerobic storage.* Blood transfusion = Trasfusione del sangue, 2016. **14**(1): p. 80-88.
294. Xu, Z., et al., *Stiffness increase of red blood cells during storage.* Microsystems & Nanoengineering, 2018. **4**(1): p. 17103.
295. Ma, S., et al., *Multiscale computational framework for predicting viscoelasticity of red blood cells in aging and mechanical fatigue.* Computer Methods in Applied Mechanics and Engineering, 2022. **391**: p. 114535.
296. Qiang, Y., et al., *Mechanical fatigue of human red blood cells.* Proceedings of the National Academy of Sciences, 2019. **116**(40): p. 19828-19834.
297. Lecklin, T., S. Egginton, and G.B. Nash, *Effect of temperature on the resistance of individual red blood cells to flow through capillary-sized apertures.* Pflügers Archiv, 1996. **432**(5): p. 753-759.
298. Smith, A.S., et al., *Myosin IIA interacts with the spectrin-actin membrane skeleton to control red blood cell membrane curvature and deformability.* Proceedings of the National Academy of Sciences, 2018. **115**(19): p. E4377-E4385.
299. Garcia-Herreros, A., et al., *Cyclic Mechanical Stresses Alter Erythrocyte Membrane Composition and Microstructure and Trigger Macrophage Phagocytosis.* Advanced Science, 2022. **9**(20): p. 2201481.
300. Biswas, A., et al., *Cholesterol Depletion by MβCD Enhances Cell Membrane Tension and Its Variations-Reducing Integrity.* Biophysical journal, 2019. **116**(8): p. 1456-1468.
301. Ridone, P., et al., *Disruption of membrane cholesterol organization impairs the activity of PIEZO1 channel clusters.* The Journal of general physiology, 2020. **152**(8): p. e201912515.
302. Gehringer, C., et al., *Accuracy of urine flow cytometry and urine test strip in predicting relevant bacteriuria in different patient populations.* BMC Infectious Diseases, 2021. **21**(1): p. 209.
303. Cao, Y., F. Gao, and W. Chen, *Comparison of different urine culture methods in urinary tract infection.* Translational andrology and urology, 2022. **11**(2): p. 260-267.
304. Xie, R., et al., *Diagnostic value of different urine tests for urinary tract infection: a systematic review and meta-analysis.* Translational andrology and urology, 2022. **11**(3): p. 325-335.

305. Boonen, K.J.M., et al., *Urine flow cytometry as a primary screening method to exclude urinary tract infections.* World Journal of Urology, 2013. **31**(3): p. 547-551.
306. Mejuto, P., M. Luengo, and J. Díaz-Gigante, *Automated Flow Cytometry: An Alternative to Urine Culture in a Routine Clinical Microbiology Laboratory?* International Journal of Microbiology, 2017. **2017**: p. 8532736.
307. Robinson, J.P., *Flow cytometry: past and future.* BioTechniques, 2022. **72**(4): p. 159-169.
308. Jolkkonen, S., et al., *Screening of Urine Samples by Flow Cytometry Reduces the Need for Culture.* Journal of Clinical Microbiology, 2010. **48**(9): p. 3117-3121.
309. van der Zwet, W.C., et al., *Evaluation of the Sysmex UF-1000i® urine flow cytometer in the diagnostic work-up of suspected urinary tract infection in a Dutch general hospital.* Clinical Chemistry and Laboratory Medicine, 2010. **48**(12): p. 1765-1771.
310. Okada, H., et al., *The basic performance of bacteria counting for diagnosis of urinary tract infection using the fully automated urine particle analyzer UF-1000i.* Sysmex Journal International, 2007. **17**(2): p. 95-101.
311. De Rosa, R., et al., *Evaluation of the new Sysmex UF-5000 fluorescence flow cytometry analyser for ruling out bacterial urinary tract infection and for prediction of Gram negative bacteria in urine cultures.* Clinica Chimica Acta, 2018. **484**: p. 171-178.
312. Ugele, M., et al., *Label-Free High-Throughput Leukemia Detection by Holographic Microscopy.* Advanced Science, 2018. **5**(12): p. 1800761.
313. Rappaz, B., et al., *Comparative study of human erythrocytes by digital holographic microscopy, confocal microscopy, and impedance volume analyzer.* Cytometry Part A, 2008. **73A**.
314. McNeal, A.S., et al., *BRAFV600E induces reversible mitotic arrest in human melanocytes via microRNA-mediated suppression of AURKB.* eLife, 2021. **10**: p. e70385.
315. Roitshtain, D., et al., *Quantitative phase microscopy spatial signatures of cancer cells.* Cytometry Part A, 2017. **91**(5): p. 482-493.
316. Pham, H.V., L. Pantanowitz, and Y. Liu, *Quantitative phase imaging to improve the diagnostic accuracy of urine cytology.* Cancer cytopathology, 2016. **124**(9): p. 641-650.
317. Rasband, W.S. *ImageJ*. 1997-2018.; Available from: https://imagej.nih.gov/ij/.
318. Dai-jun Xiang and Yulong Cong and Chengbin Wang and, J.Y.a.X.M.a.Y.-j.L.a.P.L.a.J.-l.M., *Development of microscopic review criteria by comparison urine flow cytometer, strip and manual microscopic examination.* Clinical laboratory, 2012. **58 9-10**: p. 979-85.
319. Christelle, F., D. Jacques, and R. Jean-Philippe, *Évaluation des performances de l'automate d'analyse urinaire UF-1000i ®.* Annales de Biologie Clinique, 2011. **69**(4): p. 431-439.
320. Kadkhoda, K., et al., *UF-1000i™ flow cytometry is an effective screening method for urine specimens.* Diagnostic Microbiology and Infectious Disease, 2011. **69**(2): p. 130-136.
321. Jiang, T., et al., *Urine particles analysis: Performance evaluation of Sysmex UF-1000i and comparison among urine flow cytometer, dipstick, and visual microscopic examination.* Scandinavian Journal of Clinical and Laboratory Investigation, 2011. **71**(1): p. 30-37.
322. Manoni, F., et al., *Urine particle evaluation: a comparison between the UF-1000i and quantitative microscopy.* 2010. **48**(8): p. 1107-1111.
323. Mosby, C.V., *Mosby's Medical Dictionary*. 8 ed. 2009: Elsevier.
324. Cornaglia, G., et al., *European Manual of Clinical Microbiology*. 2012: European Society for Clinical Microbiology and Infections Diseases.
325. Sharp, S.E., *Cumitech 2c: Laboratory Diagnosis of Urinary Tract Infections*. 2009: ASM Press.
326. Trevethan, R., *Sensitivity, Specificity, and Predictive Values: Foundations, Pliabilities, and Pitfalls in Research and Practice.* Frontiers in public health, 2017. **5**: p. 307-307.
327. Liu, P.Y., et al., *Real-time Measurement of Single Bacterium's Refractive Index Using Optofluidic Immersion Refractometry.* Procedia Engineering, 2014. **87**: p. 356-359.

328. Godin, M., et al., *Measuring the mass, density, and size of particles and cells using a suspended microchannel resonator.* Applied Physics Letters, 2007. **91**(12): p. 123121.
329. Carl, D., et al., *Parameter-optimized digital holographic microscope for high-resolution living-cell analysis.* Applied Optics, 2004. **43**(36): p. 6536-6544.
330. Gil-Redondo, J.C., et al., *Substrate stiffness modulates the viscoelastic properties of MCF-7 cells.* Journal of the Mechanical Behavior of Biomedical Materials, 2022. **125**: p. 104979.
331. Santoro, R., et al., *Activation of human aortic valve interstitial cells by local stiffness involves YAP-dependent transcriptional signaling.* Biomaterials, 2018. **181**: p. 268-279.
332. Symons, H.E., et al., *Automated analysis of soft material microindentation.* Soft Matter, 2022. **18**(43): p. 8302-8314.